Design, Fabrication, and Characterization of a Micro Fuel Processor

by

Brandon S. Blackwell

B.S. Chemical Engineering, University of Notre Dame, 2002
M.S. Chemical Engineering Practice, Massachusetts Institute of Technology, 2004

Submitted to the Department of Chemical Engineering in partial fulfillment of the requirements
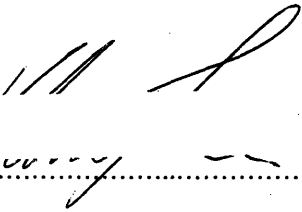for the degree of

Doctor of Philosophy

at the

MASSACHUSETTS INSTITUTE OF TECHNOLOGY

February 2008

Signature of Author...
Department of Chemical Engineering
September 5, 2007

Certified by..
Klavs F. Jensen
Warren K. Lewis Professor of Chemical Engineering
Professor of Materials Science and Engineering
Thesis Supervisor

Accepted by..
William M. Deen
Carbon P. Dubbs Professor of Chemical Engineering
Chairman, Committee for Graduate Students
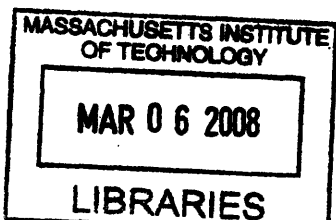
Design, Fabrication, and Characterization of a Micro Fuel Processor
by
Brandon S. Blackwell

Submitted to the Department of Chemical Engineering on September 5, 2007
in partial fulfillment of the requirements for the degree of
Doctor of Philosophy in Chemical Engineering

Abstract

The development of portable-power systems employing hydrogen-driven solid oxide fuel cells continues to garner significant interest among applied science researchers. The technology can be applied in fields ranging from the automobile to personal electronics industries. In order for fuel cell systems to outperform batteries, a method of chemically converting high-energy-density combustible fuels to hydrogen while maintaining high thermal efficiency must be developed. This thesis focuses on developing microreaction technology that minimizes thermal losses during the conversion of fuels – such as light end hydrocarbons, their alcohols, and ammonia – to hydrogen. Critical issues in realizing high-efficiency devices capable of operating at high temperatures have been addressed: specifically, thermal management, the integration of materials with different thermophysical properties, and the development of improved packaging and fabrication techniques.

A new fabrication scheme for a thermally insulated, high temperature, suspended-tube microreactor has been developed. The new design improves upon a monolithic design proposed by Leonel Arana. In the new modular design, a high-temperature reaction zone is connected to a low-temperature package via the brazing of pre-fabricated, thin-walled glass tubes. The design also replaces traditional deep reactive ion etching (DRIE) with wet potassium hydroxide (KOH) etching, an economical and time-saving alternative. A glass brazing method that effectively accommodates the difference in thermal expansion between the silicon reactor and the glass tubes has been developed. The material used in this procedure is stable at temperatures up to 710 °C.

Autothermal combustion of hydrogen, propane, and butane in excess oxygen has been demonstrated in ambient atmosphere and under vacuum. Hot spot temperatures of up to 900 °C have been measured during autothermal combustion of propane in ambient and vacuum conditions. Experimental temperature measurements have been compared to steady-state temperature estimates, and show good agreement. Finally, a computational fluid dynamics (CFD) model has been developed to study the heat transfer properties of the microreactor. Using simplified reaction schemes from the literature, the model has successfully reproduced the results observed in the laboratory.

Thesis Supervisor: Klavs F. Jensen
Title: Warren K. Lewis Professor of Chemical Engineering

Acknowledgments

Many people have made my time at MIT an enjoyable and educational experience. I would like to thank my advisor, Klavs Jensen, for his consistent support and direction. His passion for collaboration with outside parties has allowed me to develop relationships that never would have been possible otherwise. In addition, I would like to thank the members of my thesis committee, Professors Martin Schmidt, William Green, and Jeff Tester. Each provided unique insight and helpful recommendations as the project progressed. I would also like to thank Multidisciplinary University Research Initiative (MURI) and the Lincoln Labs Advanced Technology Concepts program for funding.

I have also had the opportunity to work alongside many talented students and post-doctoral associates during my time here. I would like to thank Smitha Matthews and Ben Wilhite for guiding me during my first few months in the fabrication facility. I would also like to thank Sravanti Kusuma and Gian Caviezel for their assistance in assembling the testing apparatus used for experimentation. Maurizio Rondanini played a critical role in developing and refining the solution grid employed by the CFD-ACE model described in Chapter 7. I also thank Kishori Deshpande for taking the time to discuss issues with my project, helping with the maintenance of common lab equipment, and her impromptu lab clean ups.

I also owe thanks to the entire KFJ research group. I could not have asked for a more welcoming environment in which to work. Specific thanks go to Jake Albrecht, Jane Rempel, and Jamil El-Ali for the water cooler breaks in 66-501. I would also like to thank Joan Chisholm and Alina Haverty for their patience in dealing with my complicated supply requests and for being great resources in general.

Most importantly, I would like to thank my family, to whom this thesis is dedicated. I thank my parents, Steve and Cheryl, for their love and support; my brother, Sean, for his weekend visits that forced me to get out of the lab; and I think my sister, Emily. Finally, I thank my wife, Kenzie. For over three years she tolerated the roller coaster ride – my frustrations and complaints, successes and celebrations – and provided unwavering support.

Table of Contents

List of Figures

– 11 –

List of Tables

Chapter 1   Introduction

Portable electronic devices – from cellular telephones to laptop computers to iPods – continue to require greater amounts of energy for longer periods of time. While energy demands have increased, portable power technology has failed to maintain pace. The battery has served as the primary vehicle for powering portable electronics, and improvement in battery technology remains an active area of research. Alternative research efforts have focused on developing portable electric generators such as fuel cell systems, microengines, and thermophotovoltaic systems. Electric generators have the potential to reach higher levels of performance due to the fact that the combustible fuels used to power them have energy densities an order of magnitude greater than those of their battery counterparts.

Of the types of electrical generators mentioned above, fuel cell systems are advantageous due to their high energy density, ease of miniaturization, quiet operation, and lack of moving parts. Of the many available types of fuel cells systems, only a few are suitable for portable power applications due to size restrictions and the desire to avoid the use of hazardous chemicals. Polymer electrolyte membrane (PEM) fuel cells, direct methanol fuel cells (DMFCs), and solid oxide fuel cells (SOFCs) have garnered the most attention for portable power applications.

Hydrogen is the best-performing option among combustible fuels, but its use requires an effective storage scheme. A number of strategies have been investigated including cryogenic storage, compression in high pressure vessels, adsorption to carbon nanostructures, and chemical binding in reversible and non-reversible metal hydrides. Of these technologies, only borohydride-based systems have been proven to outperform batteries [1]. As an alternative to hydrogen storage, direct processing of liquid fuels has been investigated. The direct methanol

fuel cell, for example, generates power by directly converting easily stored liquid methanol. While direct methanol systems have been developed for practical use, their efficiencies lag behind those theoretically achievable in high-temperature solid oxide fuel cells. This thesis investigates a third option: on-board reforming of combustible fuels to hydrogen-rich streams via a portable fuel processor.

1.1   Motivation

1.1.1 Consumer Electronics

Since the inception of the integrated circuit – and especially over the last two decades – the number and diversity of consumer electronics devices on the market has swelled at a fast rate. The sales of laptops and wireless telephones have significantly increased annually since their introduction to the marketplace. Annual worldwide laptop computer sales doubled from 2002 to 2006, growing from 36 million to 72.5 million units sold [2, 3] . Wireless phone sales have also increased substantially, from 600 million units sold in 2002 to more than 1 billion units in 2006 [2, 4]. Portable power systems have the potential to be used in myriad other devices including music players, portable gaming devices, digital cameras, and camcorders, among others.

Growth has been observed not only in the market for portable devices, but in the energy demand of these devices as well. For example, laptop computers with brighter screens require more power to operate. The addition of audio file playback and internet browsing features in wireless phones has taxed current power delivery devices. Along with delivering more power, it is also desirable to deliver the power for longer lengths of time. A laptop computer that can operate continually for a few days is preferable to one that can operate for only a few hours. The

devices manufactured to satisfy these needs will not only have to deliver the necessary power, but be small and unobtrusive as well.

Finally, it is promising that new developments in power supply technology have historically been quickly accepted in the marketplace. A prime example of this is the adoption of lithium-ion battery technology. Lithium-ion batteries were introduced 1990, but by 2002 Li-ion batteries already powered an estimated 75-80% of all laptop computers and about 35% of all wireless telephones [2]. This point is further supported upon investigating Figure 1-1, which illustrates the growth in lithium-ion battery sales over the first years of the technology's existence.
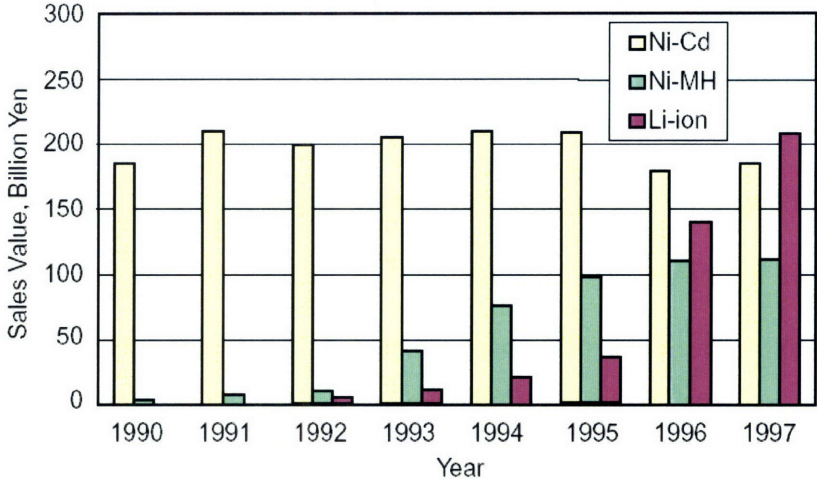
Figure 1-1. Sales growth of various rechargeable cell technologies. [5]

1.1.2 Military Applications

When properly outfitted with electronics systems, mechanized military forces are much more effective in outfighting larger but electronically blind adversaries [6]. For this reason, the United States military is pushing for a transition to a digitized battlefield. The electronics systems currently being developed – including communication, navigation, and guidance systems – all require portable, reliable power sources. In addition, the energy source must be

lightweight, so as not to impede the soldier on the battlefield. Due to their potentially large energy densities, the use of fuel cell systems may be a viable option for satisfying this need.

The performance requirements for military-grade energy devices are much more demanding than those for consumer-grade batteries. For example, batteries currently used by the military must be able to operate in a much larger temperature range, from –40°C to 60°C rather than the 0°C to 50°C range required by consumer applications [7]. Furthermore, military applications place a much larger premium on size and weight than do consumer applications.

It is expected that lithium-ion battery technology will continue to provide the military with acceptable levels of portable power in the short term [7]. However, significant improvements will be necessary in order to fulfill the military's power needs into the 21st Century. Already, battery/fuel cell hybrid systems have been predicted to play a large role in supplying power to the dismounted soldier in the near future [4, 7].

1.2 Batteries

1.2.1 Battery Basics

A battery is defined as any device that converts chemical energy stored within the battery into electrical energy via an electrochemical oxidation-reduction reaction between an anode and a cathode [8]. While a fuel cell is defined similarly, it is important to note that the reactants in a fuel cell originate from an external location, whereas in a battery, the fuel is an integral part of the device.
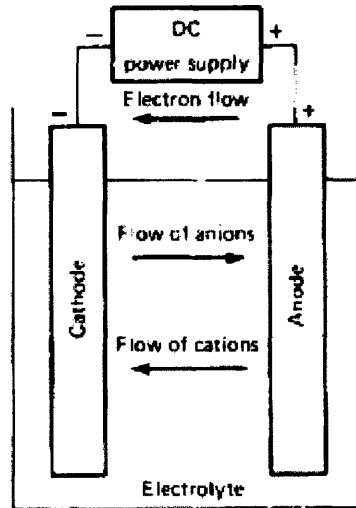
Figure 1-2. Battery schematic.

As depicted in Figure 1-2, a battery is comprised of two electrolytes – the anode (negative) and cathode (positive) – separated by an insulating layer, termed the electrolyte. During discharge, the anode is oxidized and electrons are released. Meanwhile, the cathode is reduced, accepting the electrons from the anode. These electrons can be used to power a load external to the system. To complete the circuit, mobile ions pass through the electrolyte. Depending on the type of system employed, positive ions pass from anode to cathode or negative ions pass from cathode to anode.

1.2.2 State of Battery Technologies

Depending on whether or not the system can be recharged, batteries are labeled either primary (non-rechargeable) or secondary (rechargeable). In order to recharge a secondary cell, current must be passed through the system in the direction opposite that of the discharge current. Primary batteries – ubiquitous on the consumer market – are optimal for portable electronics devices as they are inexpensive, lightweight, and possess a long shelf life. Secondary batteries, while more expensive, are ideal for larger applications as they can provide more power than primary batteries. Batteries are further characterized according to the materials that comprise the

– 20 –

anode and cathode. For example, a Zn/MnO_2 primary cell is a non-rechargeable battery with a Zn anode and MnO_2 cathode.

In characterizing battery performance, two very important measures include specific energy and energy density. Specific energy ($W\,h\,kg^{-1}$) describes the net energy per unit weight, while energy density ($W\,h\,m^{-3}$) indicates the net energy per unit volume. Obviously, it is desirable to achieve high specific energy and energy density, thus maximizing the amount of energy that can be derived from a small, lightweight cell. Figure 1-3 illustrates typical values of specific energy and energy density for current battery technologies.
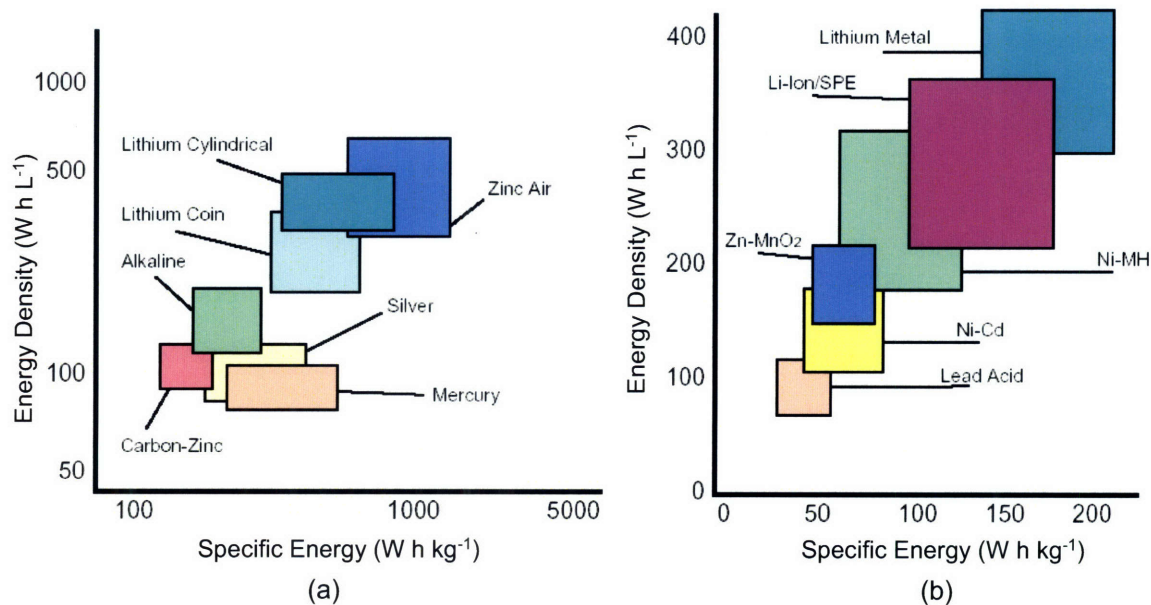
Figure 1-3. Modified Ragone plot of energy density vs. specific energy for current technologies in (a) primary batteries and (b) secondary batteries. [5, 9]

From Figure 1-3a, it can be seen that alkaline batteries – those most popular on the consumer market – represent the median in energy density and specific energy. Lithium batteries have yet to enter the consumer market for a variety of reasons including manufacturing expense and safety. In the case of Zinc Air batteries, a suitable package has yet to be discovered that would allow for its entrance into the consumer market. It should be noted, however, that

zinc air batteries might be more accurately described as fuel cells, since the air used to power the cell originates from outside the device package. In the secondary battery field (Figure 1-3b), lithium batteries again achieve the highest performance. As discussed previously, sales of lithium-ion batteries – the second best performer in the secondary battery field – have steadily increased over the past decade.

1.3   Electric Generators

Rather than deriving electricity from an internally stored fuel, electric generators are used to convert the stored chemical energy of an external fuel into electricity. For example, a heat engine utilizes combustion to extract electrical energy from an externally stored hydrocarbon fuel. Similarly, fuel cells produce energy via reaction (e.g. oxidation) of an external fuel such as hydrogen gas.

Two characteristics suggest that electric generators have the potential to overtake batteries as the leading portable power technology: specific energy and energy density. Typical hydrocarbon fuels used in electric generators can provide energy densities as high as 50 MJ/kg. This is roughly 100 times greater than that of a typical Li-ion battery (~0.5 MJ/kg). Therefore, even at an operating efficiency of only 10% – a typical value for a thermoelectric generator – the generator will provide 10 times more power to the portable device than the battery. Obviously, the advantages offered by the increase in power density are enormous.

Table 1-1. Energy Properties of Common Fuels [10]

Fuel	Specific Energy (W·h/kg)	Energy Density (W·h/L)
Hydrogen (gas)	33,300	3
Methanol	5,530	4,370
Ethanol	7,460	5,885
Propane	12,870	6,320
n-Butane	12,700	7,280
Isooctane	12,320	8,504
Ammonia	5,167	3,110

Note: Based on lower heating value

It is important to note that when considering electric generators, one cannot neglect the size or weight of the energy conversion system, as was done in the analysis above. The energy conversion system itself will always contribute to the weight and volume of the total system, thus decreasing the overall specific energy and energy density as illustrated in Figure 1-4.
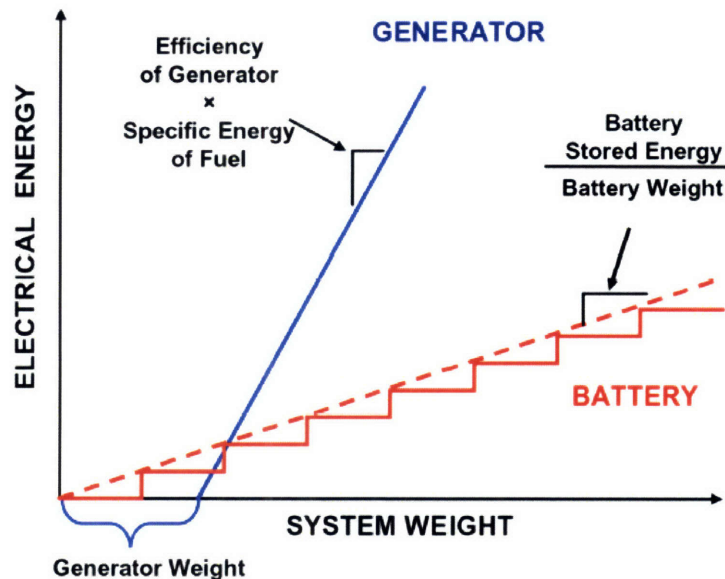
Figure 1-4. Plot of electrical energy versus system weight for generators and batteries. Note that the steps in the battery curve represent the incremental increase in system performance with an increase in number of discrete cells. [11]

From Figure 1-4, it can be seen that in order to minimize the effect of the generator mass on energy density and specific energy, it will be necessary to make the generator as small as possible. Examining the generator curve (blue), one notices that the smaller the generator weight is, the less efficient the generator needs to be in order to meet the same specifications as the battery system, that meeting point represented by the intersection of the red and blue curves. The need to miniaturize the system as much as possible provides further support for the choice to manufacture the system using microfabrication technology. While this choice restricts the possible design geometries, it is justified since it allows for the manufacture of a device on the order of a square centimeter in size.

1.3.1 Fuel Cells

Fuel cell systems have several advantages over other electric generators. Perhaps most importantly, fuel cells have the potential to operate at very high efficiencies (as high as 60%) over a wide range of temperatures. Electrochemical devices such as fuel cells can achieve such high efficiencies because they are not limited by the Carnot efficiency.

Due to the absence of moving parts, there are no frictional losses in a fuel cell system, and the unit operates quietly. Additionally, flame quenching is not an issue in these systems, and heat loss effects are thus reduced. Solid oxide fuel cells can operate on hydrocarbon fuels and do not require hydrogen as the fuel. Not only are hydrocarbons safer to handle, but their use eliminates the need to devise an efficient hydrogen storage scheme. Yet another advantage of fuel cell use is the benign nature of the by-products formed. In many cases, only H_2O and CO_2 are formed as by-products.

1.3.2 Microengines

Mechanical engines – such as internal combustion engines and steam turbines – convert combustible fuels into mechanical or electrical energy via a power cycle. The combustion engine and the gas turbine are two examples of this technology. Mechanical engines are capable of achieving efficiencies of up to 40%, an attractive number for small-scale applications.

There are currently several ongoing research efforts seeking to miniaturize engine technology for portable power generation. Epstein et al at MIT have developed a silicon microfabricated gas tubine engine the size of a quarter [12, 13]. Running on hydrocarbon fuels, these engines on a chip could potentially provide power 10 times as long as today's best batteries. A research team at the University of California Berkeley is developing a stainless steel micromachined rotary engine, with the hopes of producing a device capable of delivering 30 W [14, 15]. Research teams at the Georgia Institute of Technology and MIT have collaborated to produce a microengine/magnetic induction generator coupling that has produced 1.1 W of energy [16].

While the preliminary results in the field of microengines are promising, their development poses a difficult technical challenge. The designs are very complex and have yet to achieve significant yields of successful devices. In the case of the MIT microengine, each of the individual components work, but they have yet to function simultaneously in a single device [17]. In addition, microengine designs call for the operation of moving parts at high speeds and temperatures. Maintaining quiet operation and thermal stability of the devices is challenging.

1.3.3 Thermoelectric and Thermophotovoltaic Generators

Thermoelectric (TE) and thermophotovoltaic (TPV) generators passively generate electricity from the combustion of fuel. In the case of TE generators, a fuel is combusted to locally heat a zone of the reactor. A thermopile bridges the hot and cold zones of the reactor, and electricity is generated via the Peltier–Seebeck effect. In TPV generation, gases are again combusted in a reactor. The resultant radiation is filtered and passed to a low-bandgap TPV cell where it is converted to electricity.

TE generators have been developed by several research teams. Schaevitz et al. at MIT have investigated the use of membrane reactors for TE power generation [18]. The microfabricated device is capable of achieving a thermopile output voltage of up to 7 V, with a thermal efficiency of 0.02%. Sitzki et al. from the University of Southern California have developed a "Swiss roll" burner design capable of generating an electric power output of 0.1 W in a volume of 0.04 cm^3 [19].

Thermophotovoltaic generators have been researched since low-bandgap photocell materials became available in the late 1980s. Nielsen et al. at MIT have studied the performance of a TPV generator powered by a suspended-tube combustor [20]. The system is capable of generating up to 1.0 mW of electricity at 0.01% efficiency. The National University of Singapore has developed a micro-TPV system comprised of a silicon carbide emitter, a nine-layer dielectric filter, and a GaSb PV cell array [21]. This device is capable of producing 0.92 W of power in a volume of 0.113 cm^3.

TE and TPV generators allow for the quiet generation of electricity without the involvement of moving parts. While the components can be expensive, the designs are relatively simple. In both cases, however, efficiencies are limited. TE generators are limited by the low

efficiency of thermal to electric energy conversion, which has yet to exceed efficiencies above 12% at temperatures of 1100°C [18]. Large-scale TPV systems have achieved efficiencies as high as 12.3% [22].

1.4   Fuel Cell Systems

1.4.1 Fuel Cell Basics

A fuel cell is an electrochemical device that continuously converts a fuel into electric energy via reaction with an oxidant. While many types of fuel cells have been developed, this section will focus the three that were identified as options for portable power generation: the polymer electrolyte membrane (PEM) fuel cell, the direct methanol fuel cell (DMFC), and the solid oxide fuel cell (SOFC). Figure 1-5 provides a basic schematic of a hydrogen-powered fuel cell.
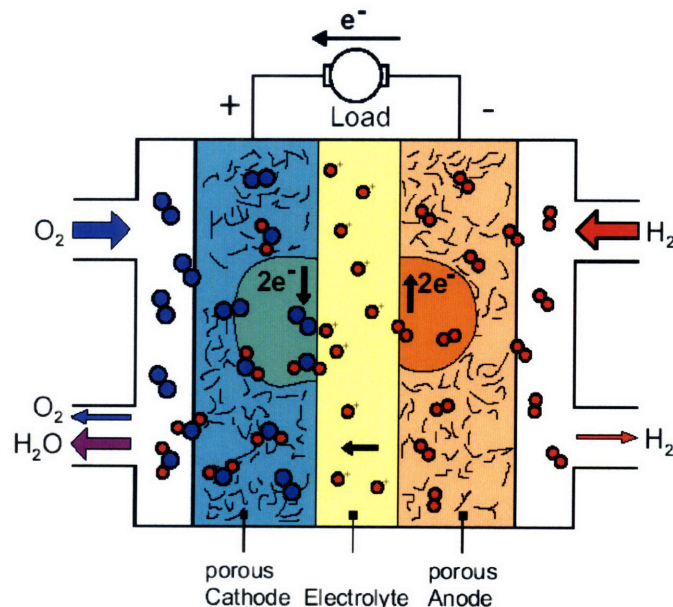
Figure 1-5. Schematic of hydrogen-powered fuel cell operation. From [23].

While the materials of construction vary, the basic design is consistent among fuel cell types: an electrolyte is sandwiched between a porous anode and porous cathode. The fuel – H_2

in the case of Figure 1-5 – passes through the porous anode and reacts catalytically at the anode-electrolyte interface. The electrolyte allows ions to pass through – positive or negative depending on the type of fuel cell – and prevents the passage of electrons which are forced out of the cell to power a load. Meanwhile, the oxidizer – usually O_2 from air – travels through the porous cathode and reacts catalytically at the cathode-electrolyte interface. In the case of Figure 1-5, the oxidizer accepts the ions from the electrolyte and the free electrons from the external load, which completes the circuit. The by-product of the process – water and, in the case of direct hydrocarbon processing in solid oxide fuel cells, CO_2 – is passed out of the system.

1.4.2 Hydrogen-Fueled Polymer Electrolyte Fuel Cells

The hydrogen-fueled polymer electrolyte membrane (PEM) fuel cell – sometimes called the proton exchange membrane fuel cell – is familiar to most as the fuel cell used to power automobiles [24-27]. The operation of the hydrogen PEM fuel cell is illustrated in Figure 1-5. Hydrogen PEM fuel cells use oxygen from the air as the oxidant. The hydrogen reacts at the anode to form two protons and two electrons. The protons pass through the electrolyte and recombine with oxygen at the cathode to form water.

Anode: $\quad\quad H_2 \rightarrow 2H^+ + 2e^-$ $\quad\quad\quad\quad\quad\quad\quad\quad\quad\quad\quad\quad$ (1-1)

Cathode: $\quad\quad 4H^+ + O_2 + 4e^- \rightarrow 2H_2O$ $\quad\quad\quad\quad\quad\quad\quad\quad\quad$ (1-2)

Hydrogen PEM fuel cells have a number of advantages. They operate using platinum/carbon electrocatalysts in temperatures ranging from 60–120°C. The low-temperature operation of hydrogen PEM fuel cells allows for quick start-up times and reduces the risk of injury due to burns. Another advantage of hydrogen PEM fuel cells is that they produce only water as a by-product of their operation. There are also several drawbacks associated with the

use of hydrogen PEM fuel cells. The polymer membrane – usually Nafion® – must be kept wet in order to facilitate the efficient transport of protons. Additionally, at temperatures of 100°C, platinum is easily poisoned when exposed to ppm levels of CO [28]. For this reason, hydrogen PEM fuel cells are almost always powered by on board ultra-pure hydrogen. The storage of hydrogen poses many difficult challenges as will be outlined later. One alternative is to reform hydrocarbons on board, which would require the purification of the hydrogen production stream.

Hydrogen PEM fuel cells can achieve efficiencies as high as 40-60% [29]. Although hydrogen PEM fuel cells have been mainly developed for mid-scale applications such as automobiles, there has been an acceleration of research focused on the miniaturization of the technology. Lee et al. at Stanford University have developed an integrated series connection of PEM fuel cells using a "flip-flop" connection [30]. The peak power of the system has been reported to exceed $40 \, \text{mW/cm}^2$. Madou et al. at the University of California, Irvine has developed a micro PEM fuel cell that makes use of pyrolyzed carbon fluidic plates [31]. On the commercial side, development of PEM fuel cells has also accelerated in recent years. The Nippon Telegraph and Telephone Corporation has developed a PEM fuel cell small enough to mount directly in a cell phone [32].

1.4.3 Direct Methanol Fuel Cells

Direct methanol fuel cells (DMFCs) are currently the leading fuel cell technology for portable power generation. As the name suggests, DMFCs are powered by a methanol solution. Methanol and water react at the anode to produce CO_2, six protons, and six electrons. As in PEM fuel cells, protons are conducted through the electrolyte layer of the DMFC. These protons react with oxygen at the cathode to produce water.

Anode: $\qquad CH_3OH + H_2O \rightarrow CO_2 + 6H^+ + 6e^-$ $\hfill$ (1-3)

Cathode: $\qquad 12H^+ + 3O_2 + 12e^- \rightarrow 3H_2O$ $\hfill$ (1-4)
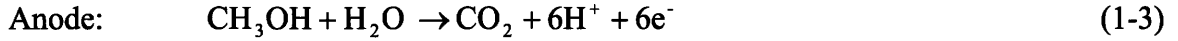
One advantage of DMFCs is that they are powered by easily stored methanol. Additionally, they require no on-board reforming, thus reducing the complexity of the overall system. Like PEM fuel cells, DMFCs are also operated at low temperatures of 60–120°C. There are also several limitations associated with DMFCs. DMFCs require water for proper operation, both for the catalytic reaction at the anode and to ensure proper transport of protons through the electrolyte. Water decreases the energy density of the fuel feed. Additionally, the use of water in the electrolyte can lead to "methanol crossover"; as water is transported through the electrolyte, the methanol dissolved in solution accompanies it. Once the methanol reaches the cathode, it can directly oxidize, drastically reducing the cell voltage. In order to prevent methanol crossover, one can either recirculate the water produced at the anode or dilute the methanol fuel to low concentration. Both of these methods reduce the overall efficiency of the cell. In addition to the problems with water, the reaction of methanol at the anode is relatively slow compared to those seen in PEM fuel cells and solid oxide fuel cells.

Despite the challenges outlined above, many large companies including Fujitsu, Hitachi, LG, NEC, Samsung, Sanyo and Toshiba have developed portable electronic devices powered by DMFCs. Smaller companies have also been involved in the development of DMFCs for portable power. MTI Micro (Albany, NY) has developed Mobion® technology that allows DMFCs to run on a 100% methanol feed [33]. Ultracell Power (Livermore, CA) has developed a 40-ounce DMFC capable of delivering 25 W of continuous power [34]. Myriad other companies

are currently developing DMFC systems, although an in-depth description is beyond the scope of this thesis.

1.4.4 Solid Oxide Fuel Cells

Solid oxide fuel cells (SOFCs) operate at high temperatures, around 500 to 1000°C. High temperatures introduce several challenges in the selection of materials. Specifically, it is important to manage the thermal stresses that arise during high temperature operation. The SOFC can be operated using a variety of fuels. Air is supplied to the cathode delivering O_2 as the oxidant. O_2- acts as the charge carrier in the electrolyte.

The SOFC is an attractive choice for power generation for several reasons. First, the solid oxide electrolyte renders the SOFC more mechanically robust than fuel cells employing liquid electrolytes. Preventing leakage of liquid electrolytes would be particularly difficult in a microdevice. Along the same lines, the SOFC operates using gaseous reactants, which are much easier to handle than the liquids used in direct methanol fuel cells. Most importantly, SOFCs can directly process fuels other than hydrogen – such as hydrocarbons, alcohols, and ammonia – due to high operation temperatures. As will be discussed, the fuel processing step always produces carbon monoxide. Carbon monoxide can be fed directly to an SOFC without poisoning the catalyst, as it does in other fuel cell types, specifically the hydrogen PEM fuel cell. This feature allows for the elimination of a fuel purification step between the fuel processor and the SOFC. Finally, the high temperature operation reduces the sensitivity of the fuel cell system to perturbations from the external environment.

The use of SOFCs also poses design challenges, mostly associated with the high temperature operation. Since the device must operate at temperatures of at least 500°C, effective

thermal management is critical. Any thermal losses to the environment will directly affect the efficiency of the unit. Furthermore, the high temperature operation raises the issue of materials compatibility and stability.

1.5   Fuel Processing for Hydrogen Generation

1.5.1 Problems with Hydrogen Storage

Ideally, one would prefer to feed hydrogen fuel to the SOFC directly rather than reform a pre-fuel gas to produce hydrogen. Unfortunately, storing hydrogen on-board can be difficult, dangerous, and inefficient. Current research is exploring novel ways in which on-board hydrogen storage can be accomplished. Pressure cylinders have been utilized for large-scale operations, but hardly seem reasonable for fueling portable power sources. Compressing hydrogen into a cryogenic liquid has also been proposed, but the low density of liquid hydrogen (0.07 g cm^{-3}) likely eliminates this option from consideration as well. Research involving active carbon nanotubes had been promising, but recent developments in this field have been scarce. Synthesis of hydrogen from reversible and non-reversible metal hydrides has shown promise recently. Varma et al. at Purdue University have developed a method of producing hydrogen from combustion-assisted hydrolysis of sodium borohydride [35]. This method has been shown to stably generate hydrogen in batch with a yield of 7wt%.

Given the low hydrogen density of existing technologies, storing hydrogen on-board as a fuel source for the SOFC is not an attractive option. This thesis focuses on the development of a method for producing hydrogen on-board from an alternative fuel source. There are many chemicals that can be used as reactants to form hydrogen including hydrocarbons, simple

alcohols, and ammonia among others. Regardless of the chemicals employed, the process of reacting these fuels to form hydrogen is referred to as fuel processing.

1.5.2 Steam Reforming of Hydrocarbons and Alcohols

The most popular method of hydrogen production currently used in industry is steam reforming of hydrocarbons and alcohols. For hydrocarbons, this reaction proceeds as:

$$C_xH_{2x+2} + H_2O \rightarrow x\,CO + (x+2)H_2 \tag{1-5}$$
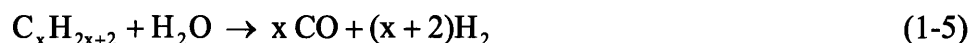
Reaction 1-5 is highly endothermic and therefore must be carried out at high temperatures. For example, steam reforming of butane is commonly carried out at temperatures of 700 to 1000°C. To achieve these high temperatures, it is necessary to burn a small portion of the inlet hydrocarbon:

$$C_xH_{2x+2} + \tfrac{1}{2}(3x+1)O_2 \rightarrow x\,CO_2 + (x+1)H_2O \tag{1-6}$$
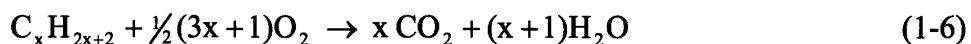
When run in concert, Reactions 1-5 and 1-6 can produce hydrogen autothermally (i.e. without the aid of an external heat source). To maximize hydrogen output, the products of Reaction 1-5 are often further reacted via the water-gas shift:

$$CO + H_2O \leftrightarrow CO_2 + H_2 \quad \Delta H° = -41 \text{ kJ/mol} \tag{1-7}$$
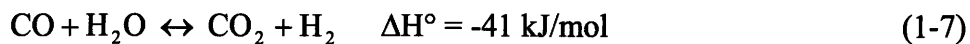
At the microscale, the use of the water-gas shift is problematic. Normally, it is desired to run this reaction at lower temperatures, thus driving the equilibrium to the right. Operation at low temperature lowers the kinetic rate of the reaction, thus requiring large residence time in the reactor to achieve equilibrium. This large residence time can only be achieved through use of a large reactor, which makes operation at the microscale difficult.

Similarly, alcohols can be used as fuel for the steam reforming reaction. One advantage to using alcohols is that the reactions are less endothermic than those involving hydrocarbons. Steam reforming of methanol can be carried out at temperatures as low as 200°C using zinc-oxide supported catalysts. The general reaction for the steam reforming of alcohols is:

$$C_xH_{2x+1}OH + H_2O \rightarrow x\,CO_2 + (x+2)H_2 \qquad (1\text{-}8)$$
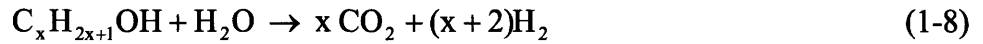
1.5.3 Partial Oxidation of Hydrocarbons and Alcohols

Rather than reacting hydrocarbons and alcohols with steam, an alternative is to partially oxidize the reactants in oxygen gas, as shown in Reactions 1-9a and b:

$$C_xH_{2x+2} + \tfrac{x}{2}O_2 \rightarrow x\,CO + (x+1)H_2 \qquad \Delta H° < 0 \qquad (1\text{-}9a)$$

$$C_xH_{2x+1}OH + \tfrac{x}{2}O_2 \rightarrow x\,CO_2 + (x+1)H_2 \qquad \Delta H° < 0 \qquad (1\text{-}9b)$$
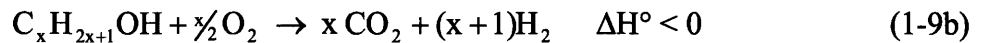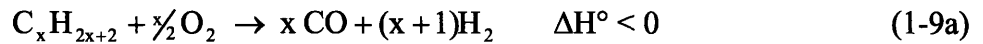
It is important that Reactions 1-9a and 1-9b be carried out using less than a stoichiometric amount of oxygen to avoid forming CO_2 in the process. The CO produced in Reaction 1-9a can either be used as a reactant in the water gas shift to produce more hydrogen, or it can be directly consumed by the SOFC. If another type of fuel cell is used, it is necessary to purify the outlet since the CO will poison the catalyst. One major advantage of the partial oxidation method is that the reaction is exothermic. Therefore, there is no need to generate heat via an additional oxidation reaction in order to drive the reaction. This allows for a much simpler fuel processor design.

1.5.4 Thermal Decomposition

Thermal decomposition (i.e. cracking) can be carried out using a variety of fuels including hydrocarbons, alcohols (usually methanol), and ammonia. Examples of these three reactions are shown in Reactions 1-10a through 1-10c below:

$$C_xH_{2x+2} \rightarrow x\,C_{(s)} + (x+1)H_2 \qquad\qquad (1\text{-}10a)$$

$$CH_3OH \rightarrow CO + 2H_2 \qquad\qquad (1\text{-}10b)$$

$$NH_3 \rightarrow \tfrac{1}{2}N_2 + \tfrac{3}{2}H_2 \qquad\qquad (1\text{-}10c)$$
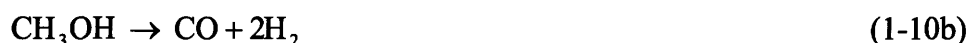
Hydrocarbon cracking (Reaction 1-10a) is an endothermic process, requiring the combustion of 10% of the fuel source to drive the cracking of the other 90%. Without the aid of a catalyst, hydrocarbon cracking requires temperatures in excess of 1000°C, although the use of catalysts can reduce this requirement to as low as 850°C [36]. These temperatures are well in excess of those required to power the SOFC, so thermal management would become a very difficult task if this reaction were chosen for the fuel processor. Another disadvantage of hydrocarbon cracking is that the reaction produces solid carbon as a product. This carbon will deposit (coke) onto the catalyst, necessitating a catalyst regeneration step between reaction cycles.

Similar to steam reforming and hydrocarbon cracking, methanol cracking (Reaction 1-10b) is also an endothermic process. However, methanol cracking offers several advantages over hydrocarbon cracking. First, methanol cracking does not result in the formation of solid carbon, so frequent catalyst regeneration is not necessary. Furthermore, methanol cracking can be run at temperatures of around 400°C with the aid of catalysts [37]. Unfortunately, methanol cracking does not offer any advantages over steam reforming of methanol. This is because 3

moles of H_2 are produced per mole of methanol via steam reforming while only 2 are produced via cracking. While the water-gas shift reaction could be used with the CO effluent to make up for this effect, the addition is not optimal for work in the microscale.

Finally, ammonia cracking (Reaction 1-10c) is yet another endothermic reaction capable of producing hydrogen gas. This reaction can be run catalytically at temperatures as low as 500°C. Similar to the other endothermic processes, it would be necessary to include an exothermic combustion step in order to drive ammonia cracking. This could be accomplished either by combusting part of the ammonia feed or by combusting the unused hydrogen effluent from the fuel cell system (i.e. anode off-gas). Again, this method does not produce solid carbon, and therefore does not lead to problems associated with catalyst coking. However, one would need to deal with the toxicity of NH_3. Additionally, ammonia is energetically expensive to produce.

1.5.5 Current Portable Fuel Processing Technologies

As mentioned previously, the difficulties associated with hydrogen storage have led many research groups to investigate continuous on-board reforming of energy dense fuels to hydrogen. Due to the requirement of at least one high-temperature step in the fuel reforming process, a primary focus of fuel reforming research has been thermal management (which will be address in Chapter 2).

In recent years, several examples of autothermal portable hydrogen generation have been developed. Leonel Arana fabricated a suspended-tube microreactor which served as a starting point for the research described in this thesis [11]. This device – described in more detail later – is capable of generating up to 9 sccm of hydrogen via 97% conversion of 6 sccm of ammonia

[38]. Palo et al have used a stainless steel microreactor to achieve simultaneous methanol combustion and steam reforming of methanol to produce hydrogen [39]. Holliday et al. also used a stainless steel reactor to produce hydrogen from autothermal methanol reforming at efficiencies between 6 and 9% [40]. Horny et al have developed a compact string reactor with catalytic brass wires to autothermally reform methanol [41].

Ganley et al. at the University of Illinois have developed a microreactor employing a ruthenium-impregnated anodic aluminum catalyst to reform 95% of anhydrous ammonia at 650°C to yield 15 sccm of hydrogen [42].

1.6   Thesis Objectives and Approach

The overarching goal of this thesis was to fabricate a microreactor capable of efficiently performing high-temperature fuel-reforming reactions for use in a portable power generator. In order to produce a highly-efficient reactor, one must develop a thorough understanding of the heat loss pathways in the system and the tools that are available to mitigate those losses. Chapter 2 includes a detailed discussion of thermal management strategies in microdevices for portable power generation. The three pathways for heat loss from the system – conduction, convection, and radiation – are described in detail. The effect of designing at small length scales is investigated. Based on this information, general design strategies to minimize heat losses are outlined. Finally, the methods and tools available for fabricating reactors at the microscale are discussed, including the advantages and disadvantages of each.

Using the insight gained from the analysis in Chapter 2, a detailed design of the micro fuel processor was developed. The design consists of a high-temperature reactor suspended from a low-temperature frame by thin-walled glass tubes. The reactor was designed as a single-unit

capable of being stacked for operation in various configurations. High-temperature operation restricts the materials and mechanical layout of the design. Furthermore, MEMS processing – the chosen method of fabrication – limits the available geometries. These and other design limitations are discussed in detail in Chapter 3.

The fabrication of the reactor is described in Chapter 4. The microchannels were fabricated using a wet potassium hydroxide (KOH) etch which is inexpensive and compatible with batch processing. KOH etching results in undercutting of convex corners. The strategies used to address this issue are outlined in Section 4.2.1. To join the glass tubes to the silicon reactor, a glass tube brazing procedure was developed. The glass sealant used in this process was stable to temperatures up to 710 °C. The details of the process are discussed in Section 4.2.3. Finally, the fabrication results and post-fabrication packaging techniques are outlined.

Once the reactor was fabricated, a detailed heat transfer analysis was performed on the system. Theoretical steady-state heat losses were estimated for isothermal reactor operation. The results of these calculations are included in Chapter 5.

Once the reactors had been fabricated, combustion tests were performed using several fuels. The results of the reaction testing are described in Chapter 6. Autothermal combustion of hydrogen, propane, and butane were achieved at atmospheric pressure and under vacuum. The temperature profiles of the reactor were measured for each experiment and compared to the heat transfer results from Chapter 5. A variety of reactor failure mechanisms were observed during testing, and they are outlined in Section 6.5.

Finally, a computational fluid dynamics (CFD) model was developed (Chapter 7). The results of the model were compared to experimental data in order to extract kinetic parameters.

Once it was established that the model was accurate over a variety of flow rates, the results were used to predict the effect of various design alterations. The model yielded insights into the operation of the reactor that could not be obtained directly via testing such as the temperature distribution through the thickness of the reactor.

Chapter 2   Thermal Management in Devices for Portable Power Generation

In order for portable power devices to compare favorably to batteries, they must be small, lightweight, and efficient. As mentioned previously, maximum theoretical efficiency is achieved by employing a high-temperature (600–1000 °C) solid oxide fuel cell as the power generator. In order for the system to operate efficiently, the reforming/fuel cell zone must be maintained at high temperatures while isolated from the environment. Given the enhanced heat transfer in microsystems, thermal isolation poses significant challenges.

2.1   Micro Fuel Processor Overview

The purpose of the fuel processor is to convert easily storable fuel to hydrogen. All of the fuels and reforming reactions mentioned in Chapter 1 require at least one high-temperature step. Additionally, endothermic reforming reactions require heat input from an external source, usually from the combustion of a fraction of the feed fuel. Finally, the use of a solid oxide fuel cell requires high temperature operation in order to facilitate the transport of O_2. through the electrolyte.

In order to compete with batteries, the size and weight of the fuel processor must be small. Miniturization poses two challenges. First, reduction in reactor size limits the residence time of the reactor. Lower residence times generally lead to a reduction in conversion. To compensate, the reactor must be run at higher temperatures when powering endothermic reactions. Additionally, miniaturization leads to enhanced heat transfer. Enhanced heat transfer increases the difficulty of isolating the reactor from the environment since the effectiveness of traditional

insulating methods is limited at small scales. One advantage of enhanced heat transfer is that it helps maintain temperature uniformity among reactor components.

In order for the reactor to operate at its maximum efficiency, the amount of heat lost to the environment must be minimized. Therefore, when designing the fuel processor, careful consideration must be given to the methods by which the reaction zone is isolated. Figure 2-1 outlines the various mechanisms by which heat can be lost from the system.
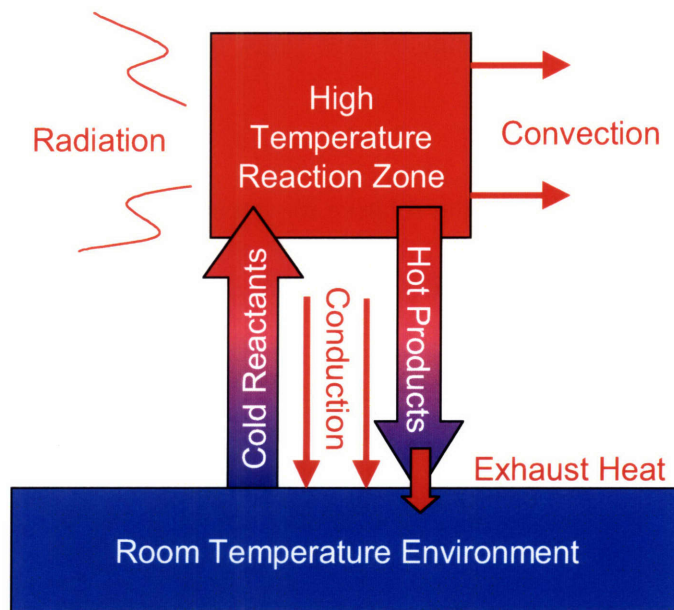
Figure 2-1. Schematic of heat-loss pathways associated with a high-temperature fuel processor. Process heat is lost via conduction, natural and forced convection from the exterior of the reaction zone, radiation from the reaction zone, and process heat lost due to forced convection of the process gasses through the reactor.

Figure 2-1 outlines four pathways by which heat can be lost from the high-temperature reaction zone to the ambient environment. Heat will be conducted through the air and through any solid in direct contact with the reactor (e.g. inlet and outlet fluidic connections). The reactor will also lose heat from its exterior faces via natural convection and forced convection (e.g. airflow due to movement of the device). In addition, the external faces of the reactor will emit radiation. Finally, forced convection of heated reactants and products through the channels of

the reactor will result in enthalpic losses from the reactor exhaust. The design of the fuel processor must incorporate features that minimize the effects of each of these heat loss pathways while preserving the heat exchange between the combustion and reforming units.

2.2 Characteristics of the Microscale

Microscale systems are defined as those with characteristic lengths on the order of 1 to 1000 microns. Microsystems exhibit several unique mechanical and thermal characteristics including: laminar flow over a large range of flow rates, high rates of heat transfer, low thermal inertia, and low mechanical inertia.

The Reynolds number defines the relative importance of intertial and viscous forces in a fluidic system and is written mathematically as follows:

$$\text{Re} = \frac{\text{Inertial Forces}}{\text{Viscous Forces}} = \frac{v\rho}{\mu/L} = \frac{v\rho L}{\mu} \tag{2-1}$$

In Equation 2-1, v represents the mean fluid velocity, ρ is the density of the fluid, L is the characteristic length of the system, and μ is the fluid viscosity. Re scales proportionally with the characteristic length of the system. Therefore, the very small length scales of microfluidic systems ensure that laminar flow (Re < 2300) is observed over a broad range of flow rates. One consequence of operation in the laminar flow regime is that turbulent mixing is not observed. While this ensures predictability of the fluid dynamics of the system, it also means that mixing of the inlet (e.g. reactants in the case of a microfluidic reactor) must be achieved via diffusion. For gas reactors, where typical diffusion coefficients range from 10^{-5} to 10^{-4} m^2 s^{-1}, the characteristic diffusion time across a 500 micron channel is between 25 and 2.5 milliseconds, respectively.

Microsystems also exhibit high rates of heat transfer. Radiation and convection, which are dependent on the external surface area of the object, are enhanced by the large surface to volume ratios seen in the microscale. Conductive heat transfer, which is inversely proportional to the length of which conduction occurs, is enhanced by the short characteristic length scales in Microsystems. Heat transfer will be addressed in detail in Section 2.3.

Due to small mass, microsystems generally have very low thermal inertia (i.e. the heating and cooling times are very quick). This property is particularly advantageous for on-demand, high-temperature energy generation as it allows for quick start up and shut down times.

In addition to thermal inertia, mechanical inertia is also very small in microsystems. Due to the small mass of microsystems, the mechanical loads placed on individual components are very small. Hence, the incorporation of features that might mechanically fail in the meso- and macroscales (e.g. cantilevers and thin beams) becomes feasible in the small scale. In addition, brittle materials such as silicon and glass become practical materials of construction for microsystems. The low mechanical inertia seen at the microscale allows for the use of these fragile materials.

2.3   Thermal Management

As mentioned in Section 2.1, in order for the fuel processor to operate efficiently, the heat loss from the high temperature reaction zone must be minimized. The section will describe in further detail the mechanisms for heat loss outlined in Figure 2-1. In addition, general design strategies that can be used to minimize heat loss from the reactor will be described.

2.3.1 Conduction

Heat loss via conduction is described by Fourier's Law:

$$q = -kA\nabla T \tag{2-2a}$$

In Equation 2-2, q is the energy flow, k is the thermal conductivity, A is the cross-sectional area normal to the direction of the gradient, and T is the temperature. It is useful to modify Fourier's Law to a linearized, one-dimensional form as:

$$q = -kA\frac{\Delta T}{\Delta L} \tag{2-2b}$$

To minimize the amount of heat conducted from the reactor, only the inlet and outlet tubes should be in direct contact with the reaction zone. Using the linearized version of Fourier's Law, one can develop a general strategy for the design of these tubes. Heat loss is directly proportional to the thermal conductivity of the material. Therefore, low-thermal conductivity materials should be used for the inlet and outlet. Additionally, heat loss scales proportionally with the cross-sectional area of the tubes. Therefore, thin-walled tubing should be used as conduit. Finally, conductive heat losses are inversely proportional to the length through which the heat must be passed. Long tube lengths are therefore desirable. Finally, the reaction zone should make direct contact only with the inlet and outlet conduits.

Equation 2-2b can be used to estimate the amount of heat lost via conduction through a tube for a given temperature gradient. Figure 2-2 outlines heat loss rates through commonly used conduit materials.
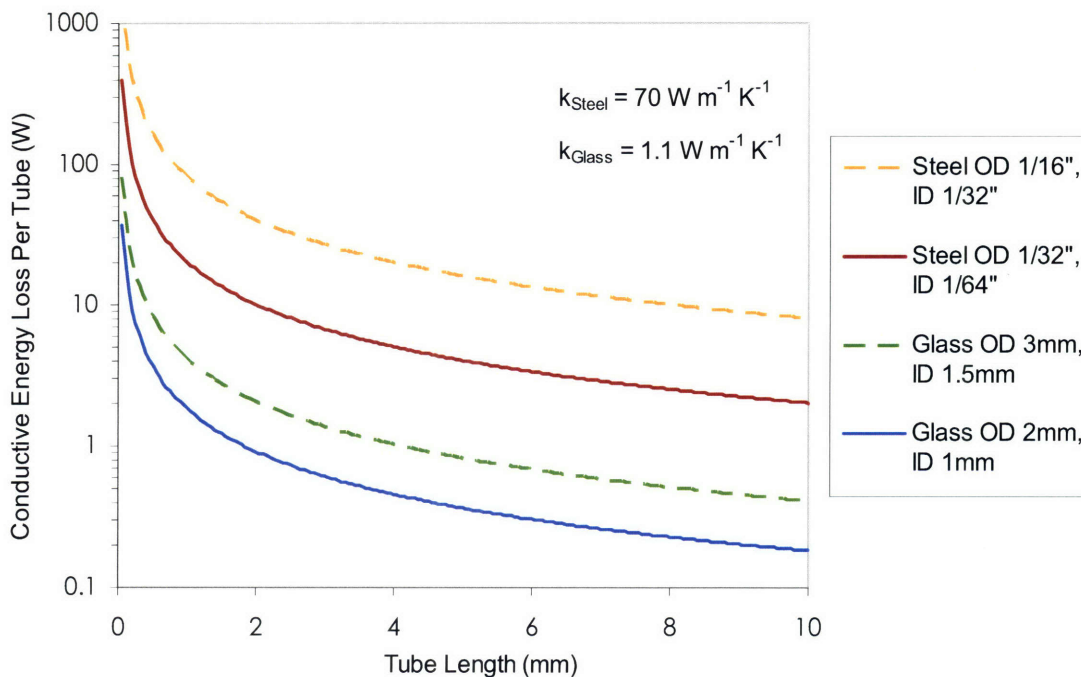
Figure 2-2. Theoretical conductive heat loss from an 800°C fuel processor to a 25°C heat sink along one tube for various materials. Commonly available tube materials and sizings were chosen. Thermal conductivities are assumed to be constant over the temperature range.

Figure 2-2 shows the per tube conductive heat losses from an 800°C reactor to the ambient atmosphere at 25°C. The tubes used in the example are commonly available thin-walled stainless steel and glass tubes. The conductive losses for each stainless steel tube are greater than 2 W in all cases. For use in a 1 W fuel processor, these losses would be unmanageable. While the glass tubing performs better than the stainless steel tubing, each glass tube would still lose at least 0.2 W of energy. Given that a reactor will use at least 2 tubes, 0.2 W per tube is still unacceptable.

There are two alternatives to using commonly available pre-fabricated tubing. One is to incorporate pre-fabricated, ultra-thin-walled capillary tubing made of materials compatible with those found in a microfabrication facility. Another option is to microfabricate ultra-thin-walled tubing as part of the reactor itself. Figure 2-3 shows the amount of heat lost via conduction from

an 800°C reactor to the ambient atmosphere for capillary tubes constructed of materials compatible with silicon microfabrication.
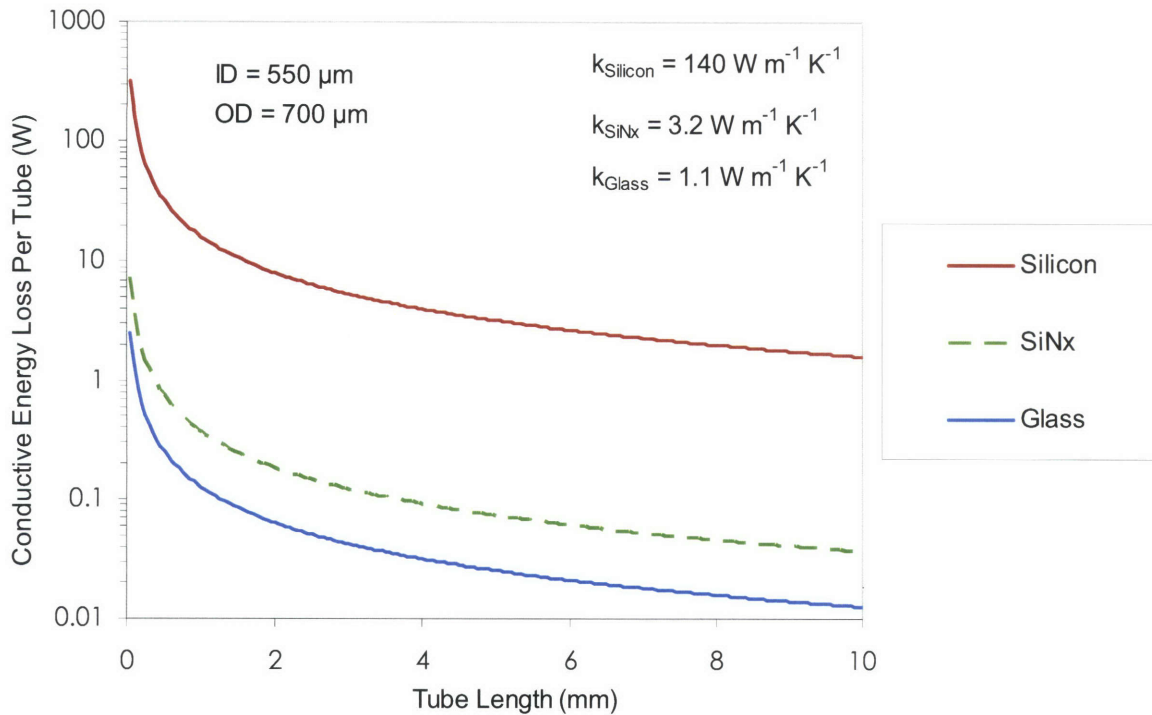
Figure 2-3. Theoretical conductive heat loss from an 800°C fuel processor to a 25°C heat sink along one ultra-thin-walled capillary tube. Tube materials were chosen from those compatible with silicon microfabrication. Thermal conductivities are assumed to be constant over the temperature range.

While silicon is not an attractive material for capillary fabrication – with conductive heat losses of at least 1.5 W per tube – silicon nitride or glass capillaries are a reasonable choice. Glass is a particularly strong candidate, with conductive heat losses of less than 0.02 W per 10-mm-long tube.

2.3.2 Convection

Heat loss due to convection (natural and forced) from a high-temperature region to a low-temperature ambient can be described by Newton's Law of Cooling:

$$q = h\,A\,dT \tag{2-3}$$

– 46 –

where q is the energy flow, h is the convective heat transfer coefficient, A is the external surface area, and T is the temperature. Equation 2-3 can be used to develop a strategy for minimizing the convective heat losses from the high-temperature reaction zone of the fuel processor system. Convective heat losses are reducing by minimizing the exposed surface area of the system. As discussed, however, microsystems are characterized by high external surface area to volume ratios. Therefore, it is critical that the design incorporate a shape with a low surface to volume ratio. The shape with the lowest intrinsic surface to volume ratio is the sphere, but they are difficult to fabricate at the microscale. Therefore, a cubic structure has been adopted for the fuel processor.

A second method of reducing convective losses from the system is by reducing the external temperature of the object. In large-scale systems, this can be achieved via the addition of thermal insulation. This technique does not work as well for microsystems, however. Due to the low surface to volume ratio, the external surface area of the object can increase rapidly as layers of insulation are added. For systems smaller than a critical dimension – termed the critical length of insulation – the amount of heat lost from the system actually increases as insulation is added. The critical radius of insulation for a sphere and a cylinder, respectively, can be calculated as [43]:

$$\text{Cylinder:} \qquad r_{crit} = \frac{k}{h} \qquad\qquad\qquad (2\text{-}4a)$$

$$\text{Sphere:} \qquad r_{crit} = \frac{2k}{h} \qquad\qquad\qquad (2\text{-}4b)$$

For typical values of k and h, the critical radius is on the order of 1 mm. In order to avoid adding several millimeters of insulation to the system, a very low-k insulating material would have to be selected.

Convective losses can also be minimized by lowering the convective heat transfer coefficient (h) of the system. This is most easily achieved by packaging the reaction zone in a vacuum.

2.3.3 Radiation

The amount of heat lost from an object due to radiation is characterized by the emissivity of the object. The emissivity is defined as the ratio of the heat transfer from a hot emitting body to that of a theoretical "black body" at the same temperature. Heat loss due to radiation from a gray body emitter at temperature T_H to a black body emitter at temperature T_C can be calculated as:

$$q = \varepsilon_H \sigma A_H (T_H^4 - T_C^4) \qquad (2\text{-}5)$$

In Equation 2-5, q is the rate of radiative heat loss, ε_H is the emissivity of the gray body emitter, σ is the Stefan-Boltzmann constant (5.7×10^{-12} W·cm^{-2}·K^{-4}), and A_H is the external surface area of the gray body emitter. ε_H is an intrinsic property of the material and varies with temperature.

Radiative losses scale as the fourth power of temperature, and therefore become more important – compared to convective and conductive losses – as the temperature of the system increases. When a reactor is coupled with a photovoltaic generator, radiative losses can be converted to electrical power. In this case, it is desirable to fabricate the reactor using high emissivity materials. When fuel reforming is the goal, however, the radiative losses must be minimized to increase system efficiency. Two methods of reducing radiative losses include incorporating a reflective shields and fabricating the reactor from low-emissivity materials.

When analyzing the transfer of radiation between two bodies, the net exchange can be approximated as that between two gray bodies. The reactor serves as the hot zone and either the mirror or the TPV cell serves as the cold surface. Two critical factors must be considered when making this approximation: the view factor and the apparent emissivity.

The view factor, F, is a geometric construct that describes the fraction of radiation emitted by the hot surface that is incident on the cold surface. Values of F range from 0 to 1, with 1 representing complete exchange of radiation between the two surfaces. Figure 2-4 illustrates the exchange of radiation between two surfaces with differing view factors.
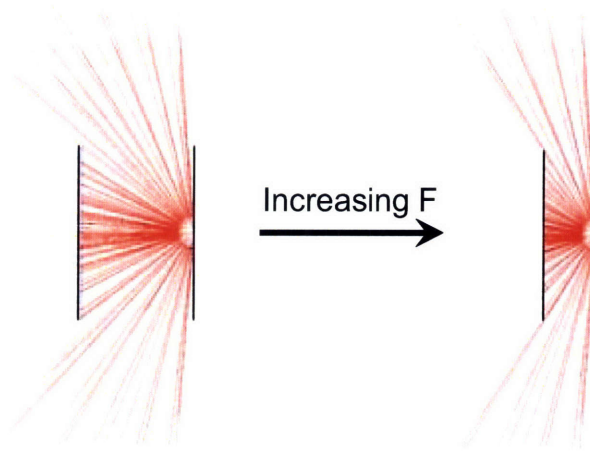
Figure 2-4. Exchange of radiation between two surfaces with differing view factors. As the hot and cold surfaces approach each other, F approaches 1.

From Figure 2-4 it can be seen that as the hot and cold surfaces approach each other, a larger fraction of radiation emitted by the hot surface is incident on the cold surface. In the case where $F = 1$, all of the radiation emitted from the hot surface arrives at the cold surface. Theoretically, a view factor of 1 is realized in two configurations: infinite parallel plates and complete enclosure of the hot body by the cold body. In practice, the best approximation is achieved when the reflective shields or TPV cells are as close as possible to the radiating surface of the reactor.

In addition to the view factor, the exchange of radiation between two gray bodies is dependent upon the apparent emissivity, ε_A. The apparent emissivity is defined as:

$$\frac{\varepsilon_A}{\varepsilon_H} = \frac{q_{\text{without cold body}}}{q_{\text{net, with cold body}}} \tag{2-6}$$

where ε_H, is the emissivity of the hot surface.

In the case where $F = 1$, the apparent emissivity can be calculated as [44]:

$$\varepsilon_A = \frac{1}{1/\varepsilon_H + 1/\varepsilon_C - 1} \tag{2-7}$$

where ε_C, is the emissivity of the cold surface.
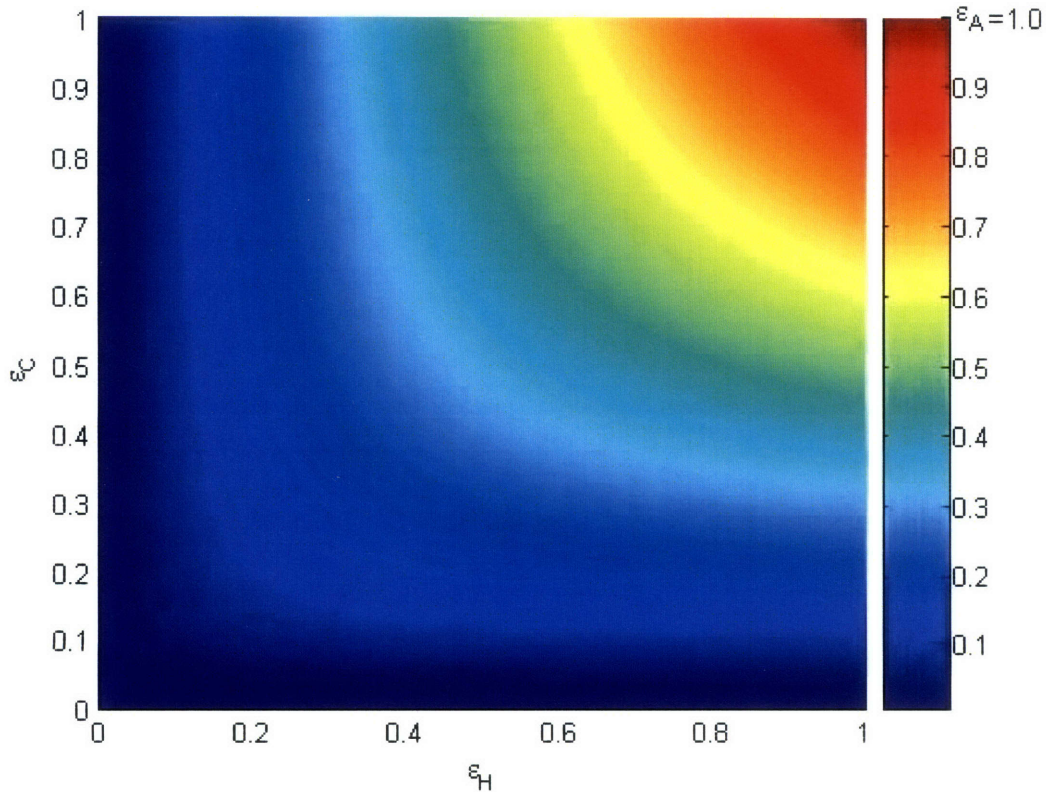
Figure 2-5. Apparent emissivity, ε_A, of a hot surface in close proximity to a cold surface (view factor = 1).

Equation 2-7 shows that the apparent emissivity of the hot surface is equally dependent upon the actual emissivities of both the hot and cold surfaces. Figure 2-5 shows that the apparent emissivity can never be larger than the emissivity of the cold surface. Therefore, when employing reflective mirrors to minimize the apparent emissivity, it is important to select mirror materials with as low an emissivity as possible. Many materials suitable for use as reflective mirrors have apparent emissivities of 0.1 or less. Hence, it is possible to reduce the amount of radiative heat lost from the system by over 90% if the mirrors can be placed very close to the reactor surface.

2.4 Fabrication Technologies Compatible with High-Temperature Systems

Several options are available for fabricating high-temperature microscale chemical systems including conventional micromachining, successive laminating of multiple layers of metal or ceramic, and silicon-based MEMS microfabrication. The advantages and disadvantages of each technique are outlined in this section.

2.4.1 Conventional Micromachining

Conventional micromachining techniques include turning, milling, and drilling. Micromachining is compatible with a large variety of materials including metals, plastics, and to a limited extent, ceramics. Precision tools have been used to make parts with features on the order of 50 μm [45]. For feature sizes on the order of a micron, non-conventional tools such as lasers are required [46].

The adoption of conventional micromachining as a fabrication method provides several advantages. First, expensive and maintenance-intense cleanrooms are not required. Also, the

tools are relatively inexpensive. Complex 3-D structures can be made relatively easily. Finally, conventional micromachining is quick when making a small number of prototypes.

On the other hand, conventional micromachining is not conducive to scale-up as parts are made one at a time. In addition, integration of a variety of materials can be difficult. Also, the minimum feature size of 50 μm is relatively large compared to other fabrication methods.

2.4.2 Thin-Layer Lamination

Thin-layer lamination involves the assembly of a 3-dimensional structure via the successive bonding of patterned layers. This technique can be employed with metals, ceramics, and plastics.

Thin-layer lamination can be used with a wide range of materials. Additionally, highly complex 3-dimensional structures can be fabricated with laminates. However, layer by layer bonding can be a time consuming process, especially for mass produced microdevices. Also, thin-layer lamination requires expensive specialized equipment.

Researchers at Pacific Northwest National Laboratories (PNNL) have developed a high-temperature stainless-steel microcombustor capable of operating at temperatures of up to 900 °C [47]. The fabrication of these devices involved the photochemical etching of 250-μm thick stainless steel shims. The etched shims were then bonded via high temperature, high pressure (900 °C, 4000 psi) diffusion bonding to form the final geometry. Similar fabrication methods, using different materials and bonding conditions, have been used at PNNL to fabricate microfluidic components, heat exchangers, chemical sensors, separators, and other components [48-51].

2.4.3 Silicon-Based MEMS Microfabrication

Silicon-based MEMS microfabrication is based on processing technology developed by the integrated circuits (IC) industry. Feature sizes range from submicron to millimeter length scales. In addition to silicon, thin films of silicon dioxide, silicon nitride, and various metals can be incorporated into designs. These materials can be precisely deposited using a series of steps including photolithography, chemical vapor deposition (CVD), wet and dry etching, and wafer bonding. Additionally, bulk etching of silicon allows for the construction of channels and pits of varying aspect ratios.

Silicon-based microfabrication processes are highly scalable, with the potential to produce a large number of dice at once on a single silicon wafer. Photolithography allows for the fabrication of very small features (down to sub-micron scale) with high precision. Additionally, device electronics can be fabricated directly on the device, allowing for the incorporation of a variety of sensors and actuators. Silicon microfabrication can also be easily automated.

Silicon microfabrication also has its limitations. Silicon processing requires an expensive and maintenance-intense cleanroom facility. Many microfabrication techniques require expensive specialized equipment. In addition, the types of geometries achievable with silicon microfabrication are limited.

Chapter 3 Micro Fuel Processor Design

The design of the micro fuel processor began with a review of a design previously developed by Arana (SµRE I) [11, 38]. This chapter describes the design of a new suspended tube reactor for use in small-scale fuel processing. Several features have been incorporated to address the thermal management issues outlined in Chapter 2. Additionally, this design seeks to minimize the amount of time, complexity, and expense required to fabricate a viable portable fuel processing device.

3.1 A Starting Point: SµRE I

SµRE I was used as a starting point for the design of the micro fuel processor. Arana's fabrication process – described in detail in Appendix A – was carried out using MEMS fabrication techniques on a 100-mm wafer diameter based process line. A schematic of the design is provided in Figure 3-1.
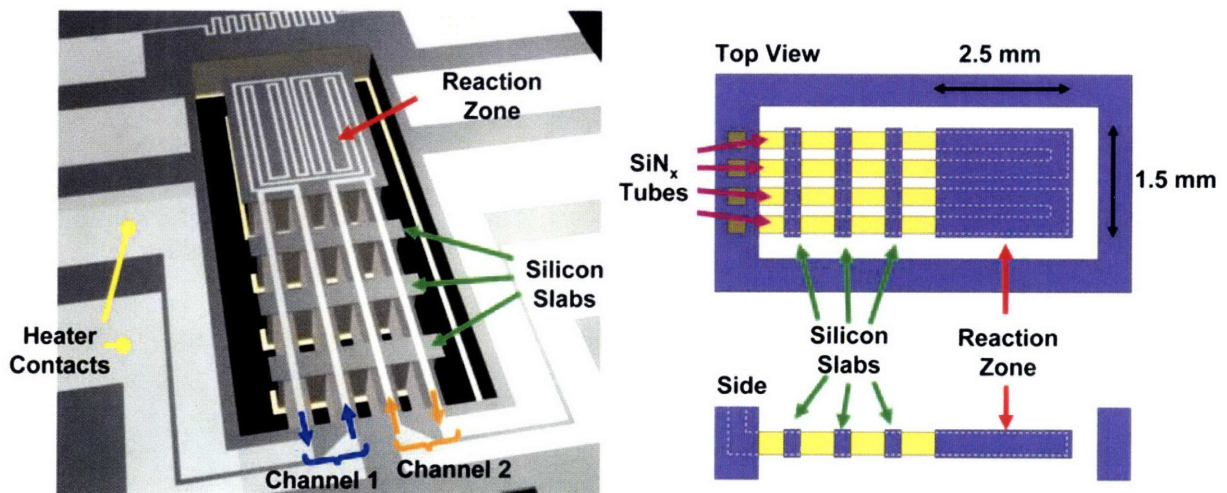
Figure 3-1. Schematic of Arana's suspended tube reactor (SµRE I). The four suspended tubes are each 200µm wide by 480µm high. The overall die dimensions are 8 x 10 mm. [38].

High temperature catalytic reactions are carried out in the single crystal silicon reaction zone measuring 1.5 by 2.5 mm. The reaction zone is suspended from the surrounding frame via four, thin-walled (2-μm thickness) silicon nitride tubes, each 3 mm in length. These tubes act as inlet and outlet conduits, supplying the reaction zone with fuel and providing a path for the exhaust. Heat exchange is achieved between the inlet and outlet streams via silicon slabs that span the width of the tubes. The silicon frame includes etched fluidic channels and ports, allowing for the attachment of macroscopic fluidic connections.

The air surrounding the reaction zone and SiN_x tubes can be evacuated, allowing for the near-elimination of convective heat transfer losses. Heat exchange between the inlet and outlet streams reduces the amount of heat lost due to forced convection in the exhaust streams. The thin walls and low thermal conductivity of the SiN_x tubes lead to very small heat losses via conduction. Various packaging schemes – including mirrored internal package surfaces – can be incorporated to mitigate radiative losses from the reaction zone. The tubes are connected to fluidic channels etched into the silicon reaction zone via deep reactive ion etching (DRIE).

3.2   Proposed Design Improvements

While SμRE I achieved simultaneous autothermal combustion and hydrogen generation, the original design included several limitations including:

- Small reactor volume
- Time-consuming, complex fabrication process with non-standard starting materials
- Heavy use of deep reactive ion etching (DRIE)
- Fragile inlet and outlet tubes that are difficult to fabricate
- Complex catalyst loading scheme

The reaction portion of SµRE I measured 1.5 by 2.5 mm with an internal reactor volume of ~1 µL. The goal of the new design was to increase the reactor dimensions to 10 by 10 mm, the size of the high-temperature SOFC being developed by group collaborators. Based on these dimensions, the new design would have an exposed surface area roughly 20 times greater than SµRE I. In order to compensate for the twenty-fold increase in available heat transfer area, the design called for twenty-fold increases in available reaction surface area and channel volume.

The microfabrication process for SµRE I – described in [11] – required roughly 135 hours of fabrication time in MIT's Microsystems Technology Laboratories (MTL), although this number would likely be lower in an industrial setting. The process required complex bonding steps, handling of fragile ultra-thin silicon wafers, and a molecular fluorine release etch. Expensive non-standard wafers were used to begin the process, including ultra-thin silicon wafers and SOI wafers. In addition, the process was not repeatable using the existing equipment in MTL once the fabrication facility upgraded from 100-mm to 150-mm wafer based machines. The goal of the new design was to reduce the fabrication time such that new designs could be fabricated within days rather than weeks. It was also necessary to eliminate the need for expensive, non-standard starting materials.

The channel molds, ports, and release pits in SµRE I were etched using an STS DRIE plasma etcher. While DRIE is useful for etching high aspect ratio structures, its high expense and incompatibility with batch fabrication have limited its adoption at the industrial scale. DRIE non-uniformity was also the primary reason that the original SµRE I process was not scalable to 150-mm silicon wafers. One goal of the new design was to adopt an inexpensive and scalable channel etching scheme to replace DRIE.

The inlet and outlet tubes fabricated for SµRE I required a complex fabrication scheme in which channel molds were etched and partially enclosed, and low-stress silicon nitride was grown on the exposed surfaces. The growth of 2 µm of nitride required a full day in the deposition tube. In addition, the resulting tubes were square in cross-section. The corners of the tubes acted as stress concentration points, and as a result, the maximum tolerable pressure gradient across the tubes was 2 atm. The new design called for the use of easily-fabricated, durable tubing to eliminate these problems.

Finally, SµRE I required the patterning of specialized fluidic stop valves in order avoid loading catalyst into the entrance tube, causing pre-mature reactant combustion. Given the desire to eliminate DRIE, inclusion of fluidic stop valves – which generally require high aspect ratio etching – would be much more difficult in the new design.

3.3   SµRE II and SµRE III

SµRE II and SµRE III were monolithic suspended-tube reactors developed by Ole Nielsen. SµRE II was designed as a larger version of SµRE I, with the primary goal of increasing power output. However, fabrication limitations led to the abandonment of the design.

SµRE III – shown in Figure 3-2 – was fabricated as a three-wafer stack. The silicon nitride channels were redesigned in a serpentine pattern rather than the straight channel mold in SµRE I. The details of the SµRE III design and fabrication can be found in Nielsen [52].
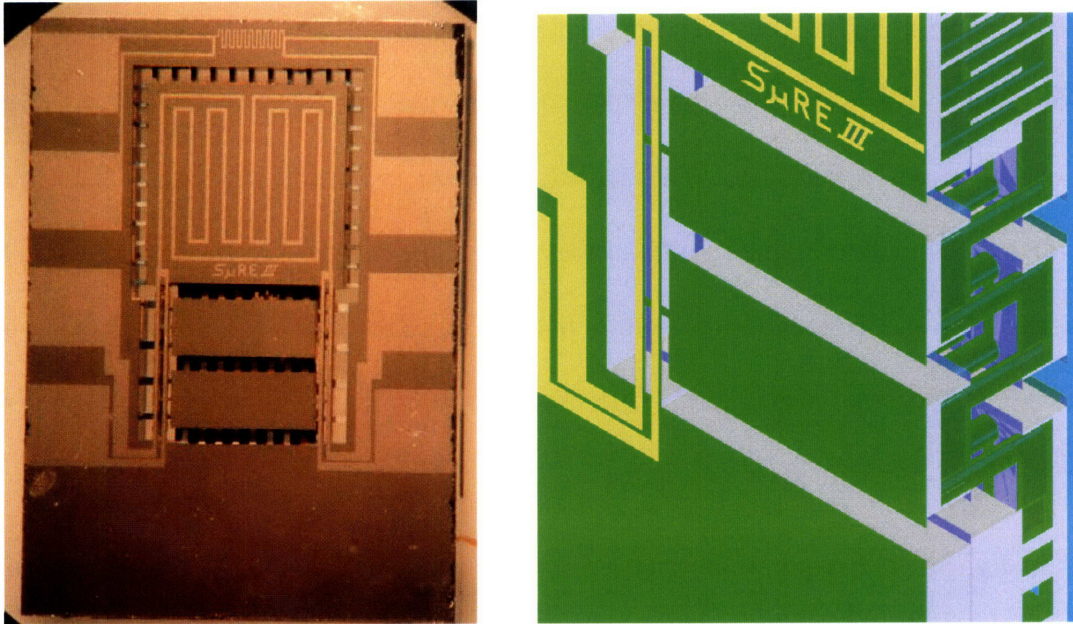
Figure 3-2. Photo and cross-section schematic of SµRE III, as designed by Nielsen [52].

3.4 SµRE IV: General Description

The design of the new suspended tube reactor – SµRE IV – takes advantage of the efficient parallel processing and precision offered by MEMS fabrication technology. Additionally, design features were chosen that would allow for quick processing and design modification. A schematic of the new suspended tube fuel processor design is shown in Figure 3-3.
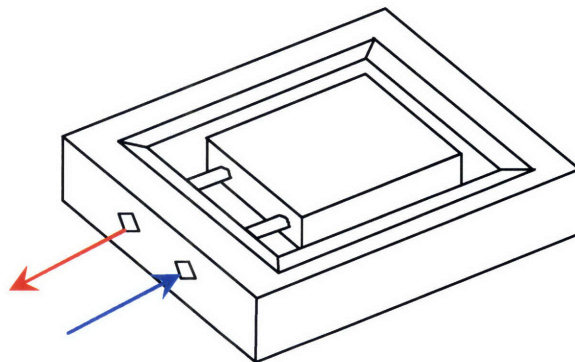
Figure 3-3. Schematic of the new suspended tube micro fuel processor (SµRE IV).

The design calls for each of the three components – the reaction zone, the tubes, and the frame – to be fabricated separately and assembled outside the clean room. By adopting this scheme, catalyst can be loaded into the reaction zone prior to the attachment of the tubing, hence avoiding deposition of catalyst in the inlet and eliminating the need for fluidic stop valves. Silicon has been retained as the material of construction for the reaction zone due to its high thermal conductivity, which promotes even distribution of heat within the reactor. In addition, silicon is the cheapest available material that is compatible with MEMS processing techniques and sufficiently stable to house a combustion reaction at 800°C.

The high-temperature reaction zone is suspended from a surrounding low-temperature frame via two, thin-walled ($\sim$100-μm thickness) tubes. The length of the tubes is limited only by the size of the surrounding frame. As in SμRE I, the U-configuration minimizes the effect of stress that arises from reactor expansion at high temperatures.

The frame of the reactor can be fabricated from any material capable of holding high vacuum. Original versions of SμRE IV included silicon fabricated frames. The frame includes fluidic ports, through which the thin-walled tubes can be threaded. Macroscopic fluidic connections can be attached to the exterior of the frame with epoxy.

As in SμRE I, the air surrounding the reaction zone and tubes can be evacuated, allowing for the elimination of convective heat transfer losses. The thin walls and low thermal conductivity of the tubes lead to very small heat losses via conduction. As will be described in Section 3.5, various packaging schemes can be incorporated to make the most effective use of the radiative energy emitted from the reaction zone.

3.5   Applications

3.5.1 Parallel Operation

One advantage SμRE IV has in comparison to its predecessors is that individual units can be easily bonded and operated in parallel. By operating multiple SμRE IV reactors in a stacked configuration, the overall efficiency of the system is increased due to the disproportionate addition of reactor volume versus external reactor surface area. When two reactors are bonded for operation in parallel, the amount of reactor volume and available catalyst surface area are increased by 100%. On the other hand, the external surface area of the combined unit is only 25% greater than a single unit. Each additional unit adds a full share of the original reactor volume, but only a fraction of the external surface area (see Figure 3-4). The stackable nature of the reactor design also allows for flexibility in the types of reaction schemes for which the design is useful.
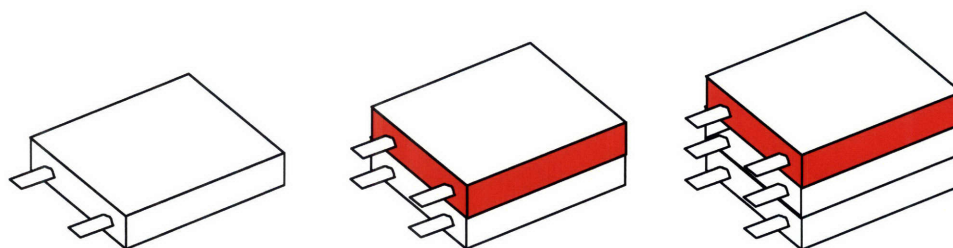
Figure 3-4. Schematic of multiple reactors operating in parallel. As each reactor is added, the amount of channel volume and exposed catalyst increases by whole multiples of a single unit. The amount of external surface area (highlighted in red) is increased by a fraction of a single unit.

3.5.2 Fuel Processing for Portable Fuel Cells

SμRE IV was designed primarily to function as a microscale hydrogen generation unit. Exothermic reforming can be accomplished with a single unit. Endothermic reforming (e.g. ammonia cracking, water gas shift, etc.) requires that two units be bonded and operated in

parallel: one to combust a portion of the feed fuel and another to house the reforming reaction. A suitable endothermic reforming configuration is illustrated in Figure 3-5.
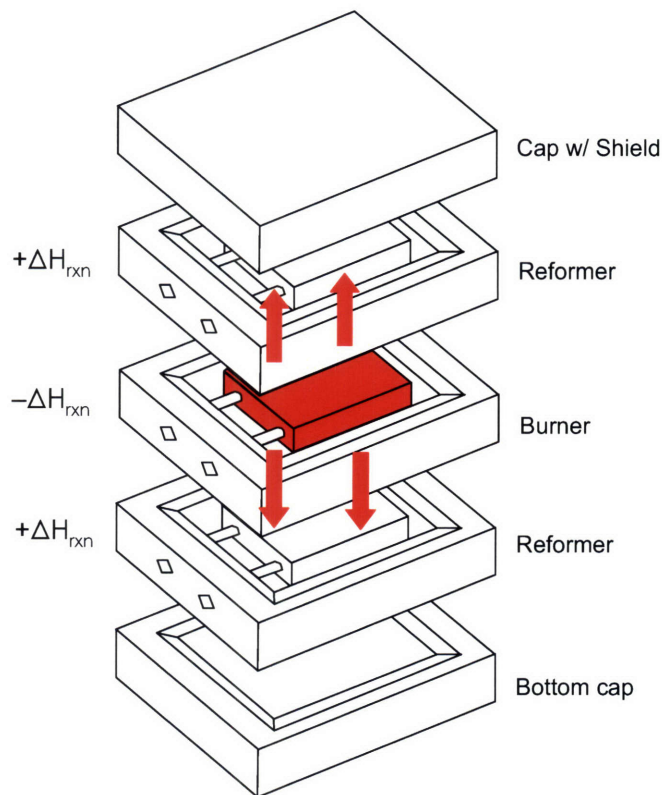
Figure 3-5. Schematic of parallel opereation of three SμRE IV reactors to achieve autothermal endothermic reforming.

The high thermal conductivity of silicon – 140 W m^{-1} K^{-1} at 25 °C and 29 W m^{-1} K^{-1} at 800 °C [53] – allows for efficient heat transfer from the burner unit to the adjacent reforming units when a high-quality bond is employed. Furthermore, the presence of extra tubes provides additional structural support.

3.5.3 Thermophotovoltaic Power Generation

In addition to reforming fuel to produce hydrogen, SμRE IV is also suitable for TPV power generation. This configuration is illustrated in Figure 3-6.
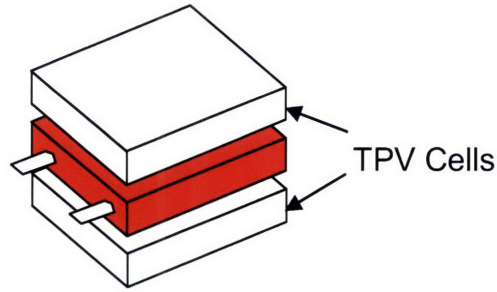
Figure 3-6. Schematic of SμRE IV reactor used for TPV power generation.

Recall from Equation 2-5, the amount of radiation transferred between a hot body at T_H to a cold body at T_C is:

$$q = \varepsilon_H \sigma A_H (T_H^4 - T_C^4) \tag{2-5}$$

In the case of TPV power generation, it is desirable to maximize the amount of radiative energy transferred to the TPV cell (the cold body). In order to do this, it is necessary to keep the TPV cells cool to maximize the temperature difference between the emitter and the cells. Maintaining the thermal gradient is a difficult task since optimal operation requires that the TPV cells be very close to the emitter in order to keep the view factor as close to 1 as possible. TPV cell cooling can be accomplished via active cooling (e.g. water flow cooling, powered fan) or passive cooling (e.g. attachment of a fanned heat sink to each TPV cell).

The apparent emissivity of an emitter in a TPV system should also be maximized. Recall that the apparent emissivity is calculated as:

$$\varepsilon_A = \frac{1}{1/\varepsilon_H + 1/\varepsilon_C - 1} \tag{2-7}$$

In order to maximize ε_A, the emissivities of the emitter and TPV cells should be as large as possible (see Figure 2-5). While silicon is an inefficient emitter ($\varepsilon = 0.63 - 0.70$), it can be coated with high emissivity materials such as zirconium diboride.

Finally, the performance of the TPV system can be improved by adding specialized IR filters between the emitter and the TPV cell. Of the radiation that is emitted from the combustion reactor, only the wavelengths short enough to create an electron-hole pair in the cell material are useful in creating electricity; the balance of the radiation that reaches the TPV cell simply creates heat. This escape of low-energy radiation not only inhibits system performance by heating the TPV cell, it also reduces the efficiency of the emitter. IR filters reflect radiation that is too low in energy to create an electron-hole pair back to the emitter. At the same time, high-energy IR is transmitted.

3.6   SμRE IV Design Details

Several of the design constraints imposed on SμRE IV were briefly introduced in Section 3.2. In this section, the methodology behind the selection of processor components will be described in more detail.

3.6.1 Cost and Processing Time Constraints

The desire to minimize the time and expense required to fabricate the reactors limited the possible machine choices to a subset of what was available for use in the cleanroom. As discussed, DRIE systems were not practical for use in the new design due to their high expense and incompatibility with batch processing. In order to minimize the cost and processing time constraints, the design was required to be compatible with multiple-wafer wet etching techniques. Of the other techniques available in the fabrication facility, wet potassium hydroxide (KOH) etching yields the fastest silicon etch rates.

Thin film deposition and growth are suitable techniques for such purposes as depositing etch masks and passivating surfaces. However, it is expensive and time consuming to grow

films in the clean room that are thick enough to act at structural features in devices. In the new design, thin film growth is limited to applications in which it is relatively quick and affordable. Additionally, the tubes employed in the design are pre-fabricated capillaries, eliminating the need for the day-long nitride tube deposition step in the SμRE I process.

3.6.2 Materials Selection

When choosing the materials used in the microfabrication process, four characteristics were considered: cost, compatibility with standard silicon MEMS processing techniques, thermal performance, and mechanical performance.

The first two properties of the fabrication materials – cost and MEMS processing compatibility – were analyzed hand in hand. Standard MEMS fabrication materials include silicon, quartz, Pyrex®, thin-film silicon dioxide, silicon nitride (low-stress and stoichiometric), a variety of polymers, and a variety of metals. Of these materials, only silicon, quartz, and Pyrex® are used to fabricate 150-mm wafers. Of those three materials, only silicon can be quickly etched using standard MEMS processes. Specialty wafers, such as SOI and ultra-thin wafers, are very expensive, while standard 150-mm wafers are mass produced and readily available in the clean room. Therefore, the process to fabricate the high-temperature reaction zone was designed to use only standard, 150-mm silicon wafers.

The first step in analyzing the thermal performance of the materials was to identify which materials would survive high-temperature (800ºC) operation. Silicon, silicon nitride, silicon dioxide, and fused quartz all soften well above 800ºC. Borosilicate and Pyrex® begin to soften at temperatures as low as 550ºC, but can be used for structures sufficiently isolated from the reactor. With the high-temperature materials identified, an effective conductor (for the reaction zone) and

an effective insulator (for the inlet and outlet tubes) must be chosen. Fortunately, silicon is an effective thermal conductor (k = 140 W m^{-1} K^{-1} at 25 °C and 29 W m^{-1} K^{-1} at 800 °C). The most commonly available ultra-thin-walled capillary tubes are fabricated from borosilicate and fused quartz. Both materials are also very effective thermal insulators. With thermal conductivities of 1.1 W m^{-1} K, borosilicate and fused quartz conduct three times less energy than the low-stress silicon nitride used for SµRE I.

In addition to the thermal conductivities, the thermal expansion coefficients of the materials were also important to consider. The reaction zone is designed to be heated to 800°C while the frame is to be held under 100°C. The large thermal gradient can yield large stresses in the system. While the channel geometry can be designed to optimize the stress distribution, it is also necessary to select materials for the reaction zone and the tubing with closely matched thermal expansion coefficients. Silicon, with $\alpha = 2.8 \times 10^{-6}$, is very closely matched with borosilicate (3.3×10^{-6}) and could conceivably be matched with fused quartz (0.5×10^{-6}). Both materials were considered for final use in SµRE IV.

In addition to thermal expansion mismatch, mechanical instability can arise from thin-film residual stresses and poor geometric design. To minimize residual stresses during the fabrication process, low-stress silicon nitride was used as an etchant mask throughout the process. To eliminate the fragility in the inlet and outlet tubes present in SµRE I, cylindrical capillary tubes were incorporated into the design of SµRE IV.

3.6.3 Size and Shape of the Reactor

While MEMS processing enables high-throughput assembly of devices with micron-scale feature sizes, the equipment and materials used in the clean room limit the geometry and feature

sizes of the fabricated devices. For example, layer-by-layer nature of MEMS processing makes it difficult to fabricate cylinders, spheres, and complex three-dimensional structures. Therefore, many common large-scale fuel processor geometries – including parallel-plate and concentric-cylinder configurations – are impractical. Since KOH etching was chosen to replace DRIE in this process, no curves could be incorporated into the design. For this reason, the reactor was designed to be square in shape in order to minimize the circumference to area ratio (and hence, the eventual surface to volume ratio).

Regarding the size of the reactor, it is desirable to maximize the internal channel volume in order to maximize the residence time for a given flow rate. By maximizing residence time, conversion of a single-step reaction will be maximized, all other things being equal. The reactor was designed to be 10 mm on each side to accommodate a high-temperature SOFC designed by group collaborators.

The use of silicon-based microfabrication also limits the depth of the device. Channel depths cannot exceed the thickness of the substrate wafer unless multiple wafer to wafer bonding steps are employed. Standard 150-mm-diameter wafers are 650 μm thick. Allowing for a structurally sound thickness to act as the channel bottom, the deepest channel allowable in the design would be ~500 μm per bonded wafer unless non-standard wafers are used.

3.6.4 Tube Design

Since the tubes are not fabricated in the clean room, we are free to choose a variety of sizes and dimensions. The tubes should be as thin as possible to minimize heat conduction along their length, yet they must be thick enough to provide structural support for the reactor.

Additionally, the tubes should be mechanically robust enough that they can be handled during the attachment step.

Minimization of conductive losses was discussed in Section 2.3.1. Low conduction requires long, thin-walled tubes made of low thermal conductivity material. From Figure 2.3, one can see that the use of 10 mm-long glass capillaries eliminates most of the conductive heat loss from the system. To further eliminate losses, the tubes would either have to be much longer. Increasing tube length, however, reduces the structural integrity of the reactor suspension. A 75-μm wall thickness was chosen because it allows for easy handling of the capillaries and is sufficiently thick to support a suspended reactor. Additionally, capillary tubes with smaller wall thicknesses are much more expensive.

Cylindrical tubes have been chosen in an effort to maximize the tolerable level of overpressure in the inlet and outlet tubes. If the reactor is to be vacuum packaged, the burst pressure of the tubes must be at least 1 atmosphere. Any pressure drop or plug in the reactor during operation will result in an additional pressure imbalance. To check the burst strength of the tubes, one can calculate the hoop stress imposed on the tube walls at a given pressure and compare it to the fracture strength of the tube materials. The hoop stress is calculated as:

$$\sigma = \frac{PR}{d} \tag{3-1}$$

The hoop stress, σ, corresponds to the stress produced upon radial expansion of the cylindrical tube. In Equation 3-1, P is the pressure difference across the tube wall, R is the radius of the tube, and d is the wall thickness of the tube. When the hoop stress is equal to or larger than the tensile strength of the tube material, fracture will occur. The fracture strength of fused quartz and borosilicate is highly dependent upon the number of defects in the material, and

is therefore highly variable. Littleton found that the tensile strength of borosilicate glass ranged from 117 to 147 MPa [54]. Using a conservative estimate of 117 MPa, one can calculate the maximum tolerable pressure for a variety of tube diameters and thicknesses using Equation 3-1. These are plotted in Figure 3-7.
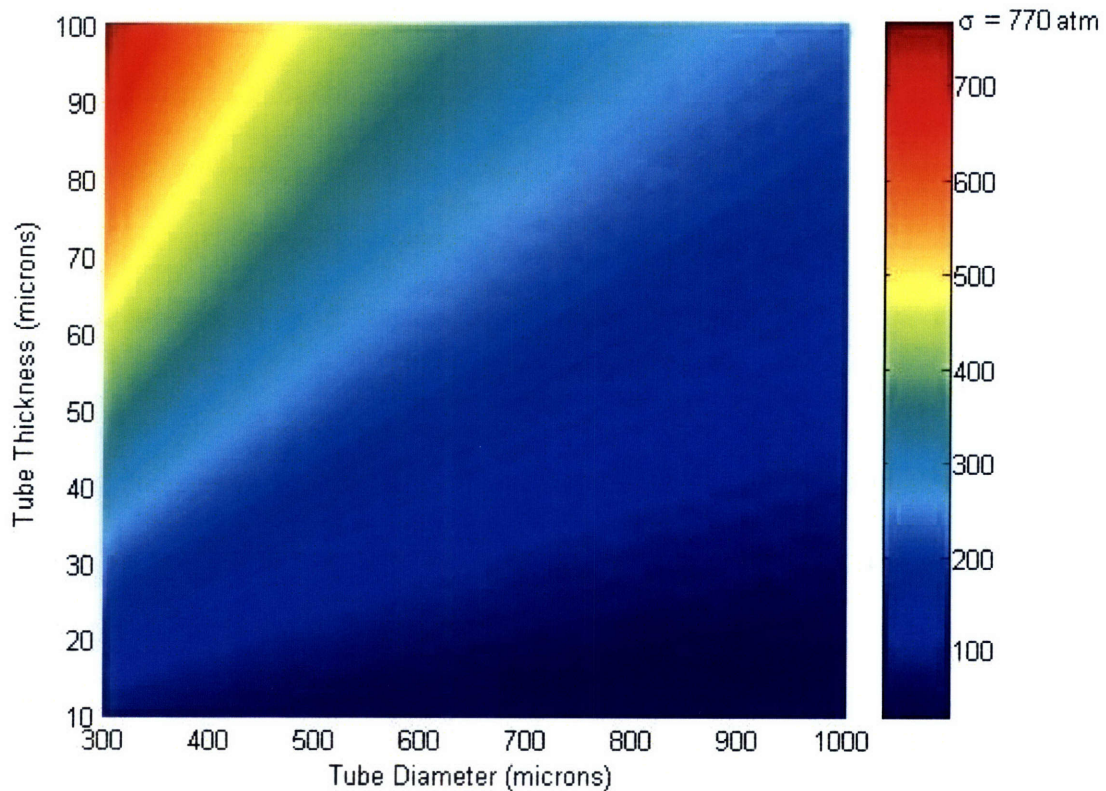
Figure 3-7. Maximum tolerable pressure gradient across tube walls for various tube radii and thicknesses. Calculations based on glass fracture strength of 117 MPa.

The smallest value of the hoop stress (23 atm) corresponds to large diameter tubes (1 mm) with very thin walls (10 μm). 23 atm is much larger than any pressure differential that might arise in SμRE IV, so it is reasonable to assume that the burst strength of the tubing will not be a factor in the performance of the reactor, assuming low defect densities.

3.6.5 Channel Geometry

The desire to use only wet etching limits the available channel geometries. All wet etches yield channels with aspect ratios close to 1:1. Furthermore, etching corners is difficult due to the isotropic nature of wet etchants. Geometries will be chosen such that wall surface area is maximized for a given volume. This will allow sufficient residence time to maximize the conversion of slower reactions. Hence, a serpentine channel configuration will be most effective. The use of a wet etch imposes two restrictions on the fabrication of the channels. First, the amount of turns incorporated into the reactor will be limited due to the undercutting of convex corners (discussed in detail in Section 4.2.1). Additionally, the fabrication of catalyst support posts and other features that would maximize internal surface area will not be possible.

Chapter 4   Fabrication and Packaging of the Micro Fuel Processor

The micro fuel processor is fabricated using standard MEMS silicon microfabrication techniques. The reaction zone and frame are fabricated separately and connected via glass brazing of thin-walled borosilicate tubes. Potassium hydroxide (KOH) wet etching is used to define the channels. The process requires the use of many other common microfabrication processes including photolithography, chemical vapor deposition (CVD), and wafer bonding.

4.1   Fabrication Process

The fabrication processes for both the reaction zone and the frame begin with two 150-mm (100) double-side-polished (DSP) silicon wafers, each of standard thickness (~650 μm, Wafer Net, Inc.). A single-side-polished (SSP) wafer of standard thickness may be substituted for one of the wafers if needed. A list of processing steps and detailed photomasks are included in Appendix B and Appendix C, respectively.

The fabrication process of the reaction zone is outlined schematically in Figure 4-1. First, a 2500Å-thick layer of low-stress LPCVD silicon nitride (ASML/SVG VTR Series 6000 furnace) is deposited on both sides of the wafers. Next, the nitride layer is patterned, exposing the channel pattern on one side of the wafer and the dicing lines and alignment marks on the other side of the wafer. The patterned nitride layer serves as an etch mask for the wet KOH etch that follows. The wafers are submerged in 25% KOH solution at 80°C for 5 hours, then checked every 10 minutes to ensure that the channels are not over etched. The average total etching time for the KOH etch was 5.5 hours. After the KOH etch, the wafers undergo a cleaning process to eliminate any residual silicon fragments. The wafers are first rinsed thoroughly in DI water.

Next, the wafers undergo two piranha cleaning steps (3:1 mixture of sulfuric acid to hydrogen peroxide). The wafers are then inspected, and subsequent piranha cleaning steps are performed if necessary. After the wafers are cleaned, the low-stress nitride mask is stripped using a hot phosphoric acid etch.
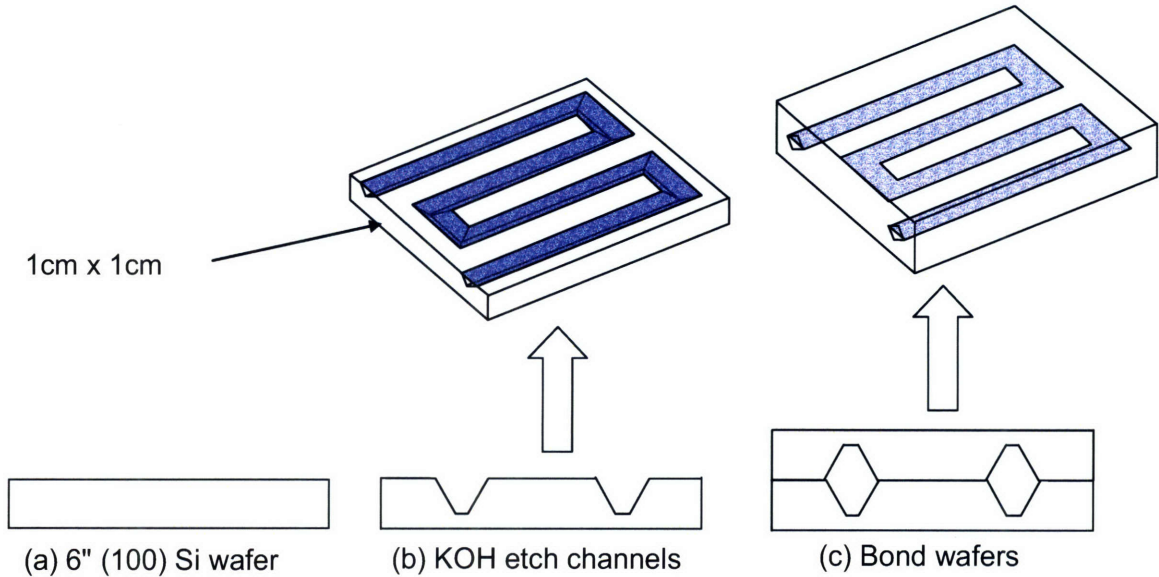
Figure 4-1. Schematic of the fabrication process for the high-temperature reaction zone.
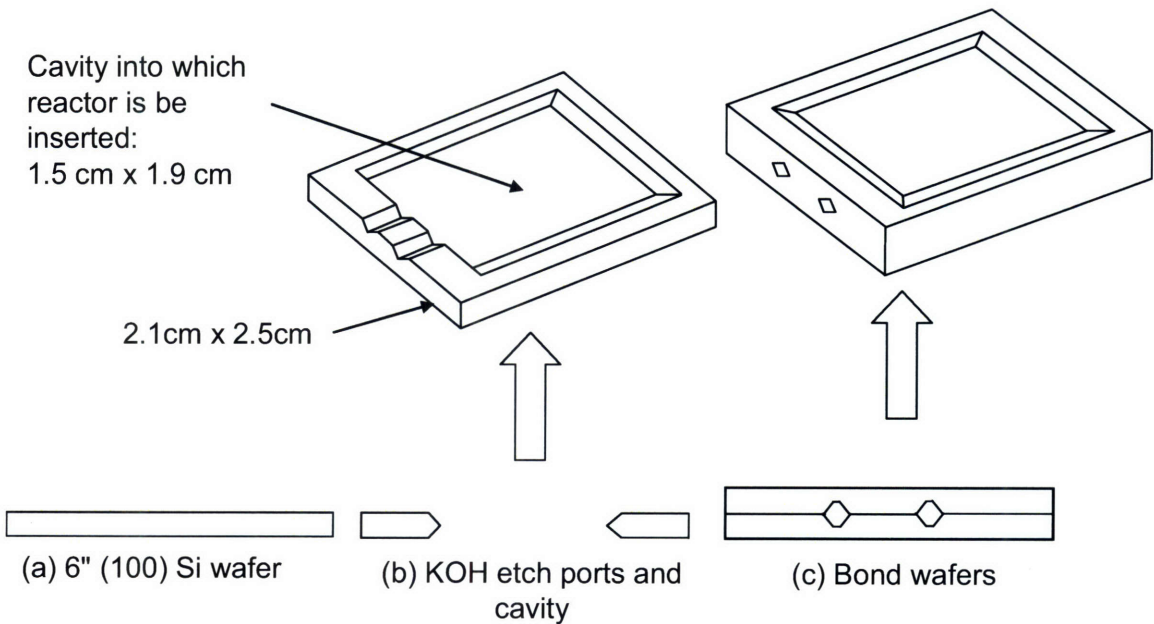
Figure 4-2. Schematic of the fabrication process for the reactor frame.

After stripping the nitride mask, the wafers are ready to be bonded. To begin the bonding process, the wafers are dipped in concentrated HF (49% solution) for 5 minutes and rinsed. Immediately following this step, the wafers are RCA cleaned, leaving out the intermediate HF dip. The wafers are then aligned and fusion bonded using an Electronic Visions aligner/bonder. Once bonded, the wafer stacks are annealed for 2 hours at 1100°C in a nitrogen atmosphere and cut into dice. The fabrication process for the silicon frame – illustrated in Figure 4-2 – is identical to that of the reaction zone, with the exception of the masks used in the process.

Once the devices are out of the clean room, the reaction zone is loaded with catalyst (described in Section 4.2.2). Next, thin-walled glass tubes are used to connect the reaction zone to the frame. The tubes are joined to the silicon reaction zone using a glass brazing technique in which a glass paste is heated to its melting point and cooled to room temperature to form a hermetic seal. Finally, the tubes are joined to the frame using 5-minute epoxy, and external fluidic connections can be made.

4.2　Fabrication Details

Several of the fabrication techniques described in the previous section were particularly challenging and required special care to produce the desired result. These processes – including KOH etching, catalyst loading, and glass brazing – are described in more detail below.

4.2.1 Potassium Hydroxide (KOH) Etching

The decision to use a wet KOH etch rather than the DRIE allows for more effective parallel processing and lower cost. However, when KOH is used as a wet etch with single crystal silicon, convex corner features in etch masks are severely undercut. This undercut is due

to the fact that the <411> crystal place etches approximately 1.5 times faster than the <100> crystal plane. An example convex corner undercut is shown in Figure 4-3.
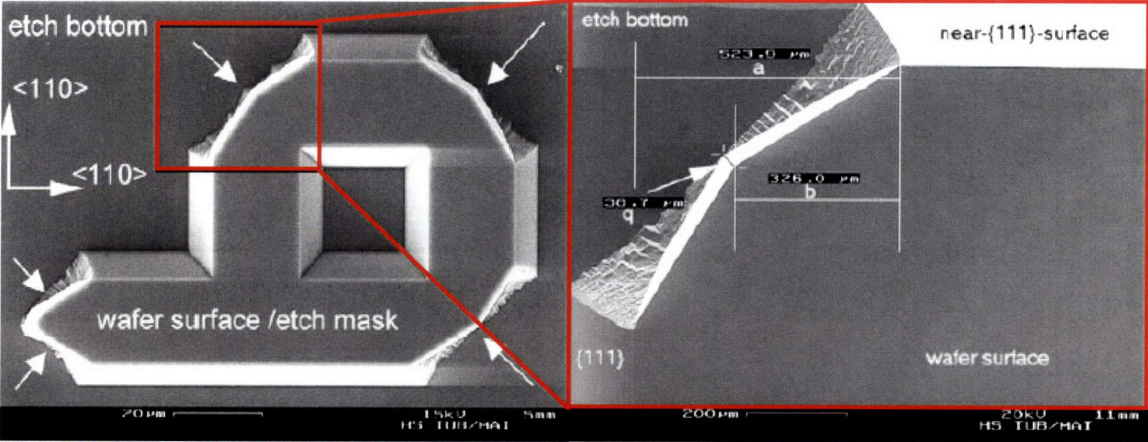
Figure 4-3. SEM micrograph of an etched structure showing convex corner undercutting [55].

In order to fabricate channels with convex corners, various features can be incorporated into the photolithography mask. These features appear as tabs extending from the convex corners of the mask. The purpose of the tab is to extend the convex corner of the mask feature into the channel. When the KOH etch is performed, the tab is undercut rather than the convex corner of the mask. With proper sizing and spacing of the tabs, consistent corners can be etched into the silicon.
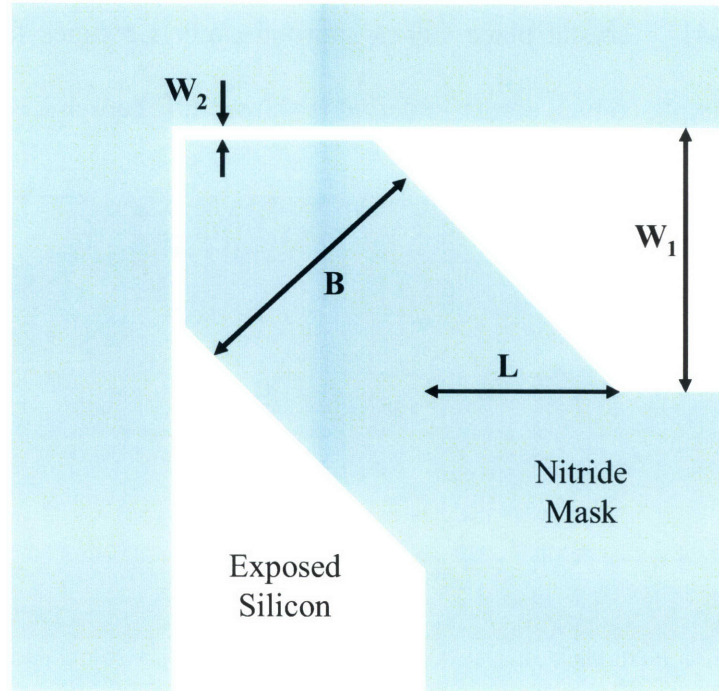
Figure 4-4. Example corner compensation structure [56].

The corner compensation features used in the masks for the first two iterations of SµRE IV are based upon those proposed by Zhang et al [56]. As shown in Figure 4-4, these features take the shape of an arrow extending at a 45° angle from the corner of the channel. The optimal dimensions of the feature are calculated as follows:

$$\frac{V_{411}}{V_{100}} D = 0.857 \left(0.424B + 0.4W_1 - 0.4W_2 \right) \tag{4-1}$$

In Equation 4-1, V_{411}/V_{100} is the ratio of the etch rate in the 411 and 100 directions and is KOH concentration dependent [57]. D is the channel depth, B is the width of the compensation structure, W_1 is the channel width, and W_2 is the resolution limit of the lithography step. Equation 4-1 can be used to find the maximum depth that can be etched for a given channel while protecting the convex corner:

$$D \leq \frac{W_1 - W_2}{0.398 + 0.730 \frac{V_{411}}{V_{100}}} \qquad (4\text{-}2)$$

The design of the corner compensation features limits the maximum packing density of the channels in the micro fuel processor. The corner compensation features cannot be allowed to overlap. Were this to happen, the width of the channel in which the overlap occurs would narrow accordingly. To avoid channel narrowing, the minimum distance between parallel channels is 2L, where L is the compensation structure "overlap length" shown in Figure 4-4.

In order to pack the channels more densely, a new corner compensation feature was included in the newest version of SµRE IV. The new feature, developed by Fan et al – is shown in Figure 4-5.
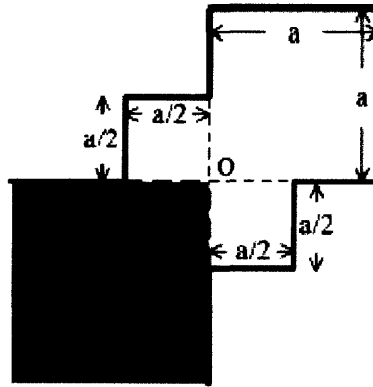
Figure 4-5. Updated corner compensation structure [58].

From Figure 4-5, one can see that the new corner compensation structure consists of one large square with side length a, and two small squares each with side length a/2. Assuming that the anisotropic etch rate ratio of the (100) and (111) planes is around 400:1, the side length, a, can be calculated directly from the etching depth as:

$$D = \left(\frac{11}{4\sqrt{32}U_c} + \frac{5\sqrt{2}}{32} \right) a \qquad\qquad (4\text{-}3)$$

where: $\qquad\qquad U_c < \dfrac{36}{5\sqrt{17}}$ $\qquad\qquad\qquad\qquad$ (4-4)

By using the corner compensation feature shown in Figure 4-5, the overlap distance (shown as L in Figure 4-4) is decreased from $1.414D$ to $0.909D$. This allowed for the design of an extra turn in the channel layout.

4.2.2 Catalyst Loading

The modular fabrication of the micro fuel processor allows for the loading of catalyst into the reaction zone prior to making fluidic connections. By loading catalyst before the brazing step, catalyst deposition in the inlet tube is avoided. This is important because if catalyst is deposited at the inlet, the reactant gases will ignite prematurely and burst the tubing.

Catalyst was deposited in the reaction zone by injecting slurries of powdered catalyst. La-doped γ-Al_2O_3 (208 m^2/g) was used as the support due to its superior thermal stability. To begin the catalyst preparation process, the γ-Al_2O_3 was weighed and impregnated to incipient wetness with an 18wt% solution of chloroplatinic acid hydrate. The slurry was then calcined in air and reduced at 400°C in flowing hydrogen gas. Assuming full evacuation of water from the sample, the percentage of platinum metal in the final slurry was 5.1wt%.

The powdered catalyst was added to water in a 20:1 weight ratio of water to catalyst. The suspension was ground using a mortar and pestle until the catalyst was fine enough to remain in suspension for at least 5 minutes after shaking. This usually required 1 hour of grinding. Once dispersed, the catalyst was loaded directly into the reaction zone chip via syringe, and dried on

one side at 80°C for 1 hour. Once dry, the reactor is loaded again, and the chip is dried on the other side. This procedure results in even deposition of catalyst on the channel walls, as shown in Figure 4-6a. Note that the channel corners in Figure 4-6a contain no catalyst as the coating was removed during the reactor cleaving. Figure 4-6b shows an image of a second reactor in which the channel turns remained coated after cleaving.

(a)   (b)
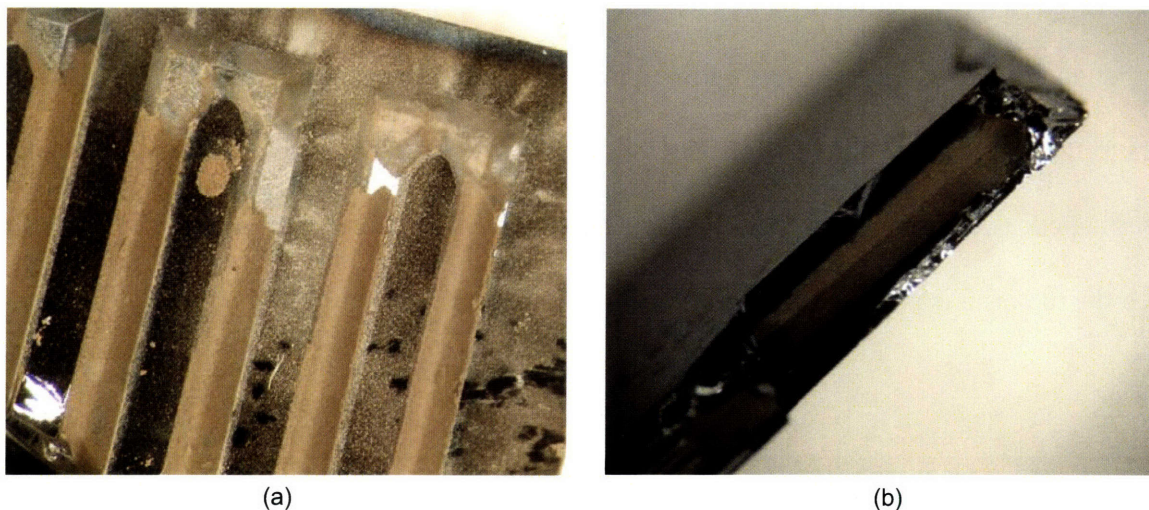
Figure 4-6. Photos of reactor microchannels after catalyst loading and subsequent cleaving.

4.2.3 Glass Brazing

The thin-walled inlet and outlet tubes are connected to the reaction chip using a glass brazing technique. Glass brazing involves applying a sealant glass at the interface between the two objects to be joined. The device is then heated above the melting point of the sealant, thus melting the glass and forming a hermetic seal between the two objects.

While silicon was fixed as the material for the reaction zone chip, a variety of materials were available for the inlet and outlet tubes and the glass sealant. The choices of materials for the tubes and sealant were closely coupled and constrained by the following considerations. Most importantly, the glass sealant and tubes must be stable at the desired operating temperature of the device, at least 600°C in the case of the micro fuel processor. Additionally, the tubes must

melt – and preferably soften – at a higher temperature than the melting point of the sealant glass to ensure the stability of the device during the brazing step. To maintain mechanical stability during temperature swings, the thermal expansion coefficients of the sealing glass and tubes must be closely matched to that of silicon ($\alpha = 2.8 \times 10^{-6}$/K at 20°C). Finally, the sealing glass must be safe and convenient for use in the available laboratory facilities.

After considering the factors outlined above, several materials were chosen as candidates for inlet and outlet connections, as outlined in Table 4-1. Note that in Table 4-1 the strain point refers to the temperature above which stresses that develop within the material upon heating will be permanent (i.e. present upon cooling). The softening point refers to the temperature above which the material is susceptible to permanent deformation (such as sagging).

Table 4-1. Properties of Materials Considered for Tubing [59, 60]

	α (10^{-6} °C^{-1})	k (W m^{-1} K^{-1})	Strain Point (°C)	Softening Point (°C)
Silicon (Reactor)	2.8	140	> 1000	--
Silicon Nitride	2.3	3.2	> 1000	--
Fused Quartz	0.55	1.4	1120	1683
Borosilicate (Pyrex®)	3.25	1.1	510	821

While silicon nitride strains at a very high temperature, insulates well, and has a thermal expansion coefficient close to silicon, it is not commonly used as a material for capillary tubing. Several attempts were made to incorporate fused quartz tubing, but the resulting reactors broke due to thermal expansion stresses. The best brazing results were obtained using VitroCom borosilicate capillary tubing. Tubes were cut to the desired length (~1 cm) by scoring the side using a diamond tipped wand and fracturing by hand.

A wide variety of brazing materials were tested for use in the reactor. An exhaustive list of brazing attempts is listed in Appendix D. After extensive testing, SEMCOM SCC-7 glass frit powder was chosen as the brazing material.

Two chucks were used to perform the glass brazing. Using the first setup, shown in Figure 4-7a, the tubes are threaded through the ports in the silicon frame. The tubes are then aligned with the channels in the reaction zone chip, and the sealant is applied. In the second setup, shown in Figure 4-7b, the tubes are instead threaded through a support plate above the brazing chuck. This setup was used for the fabrication of standalone reactors, allowing for the conservation of microfabricated silicon frames. Once the sealant glass has been applied, the brazing chuck is placed in the oven and heated to the appropriate temperature. In the case of SCC-7, the reactors were heated to 350 °C at a rate of 5°C/min and held for two hours. This allowed the binder in the SCC-7 adequate time to burn off. The reactors were then heated to 690 °C at a rate of 5°C/min and left for two hours while the sealant glass re-flowed. Finally, the reactors were cooled to room temperature at a rate of 1°C/min. The entire brazing process was performed in an ambient atmosphere.

(a)   (b)
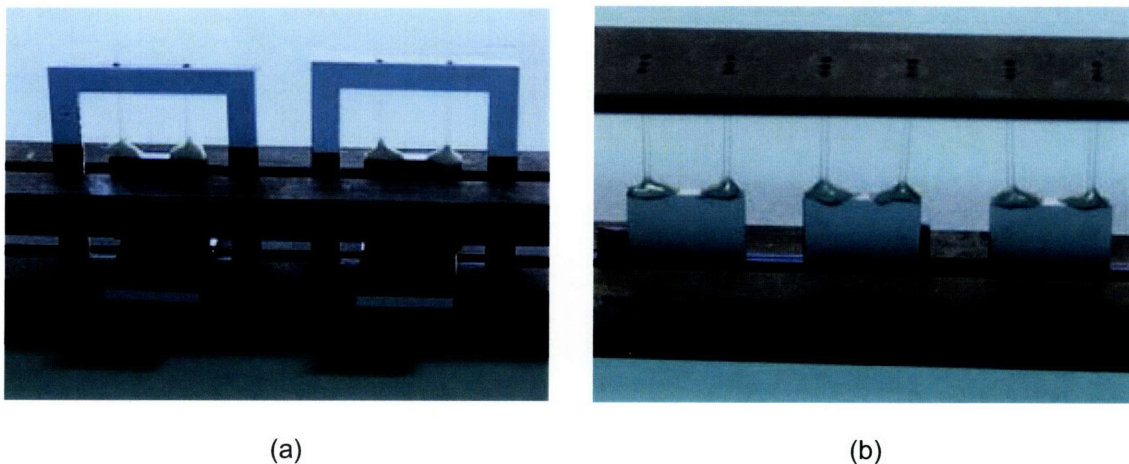
Figure 4-7. Reactor setup for glass tube brazing procedure.

4.3   Fabrication Results

4.3.1 Internal Channel Geometries

The photolithography masks used for the KOH etch are included in Appendix C. The first fabrication masks for the reaction zone chip included a channel width of 1 millimeter. The fabrication results are shown in Figure 4-8. The KOH etch produced the desired channel geometry, with nearly perfect convex corners. However, the original reactor design included several flaws. The large width of the channel led to a relatively short channel length, thus limiting the residence time of the reactants. Additionally, the 1-mm channel width made it necessary to time the KOH etching step; if the wafer is left in the bath for too long, the KOH will etch completely through the thickness of a standard wafer. Due to etch rate inconsistencies across the length of the wafer, the timed etch resulted in inconsistent channel depth, especially at the fringes. Finally, the brazing interface on the chips was completely flat. This geometry made it difficult to align the tubes for brazing and led to a finished seal that was structurally unsound.
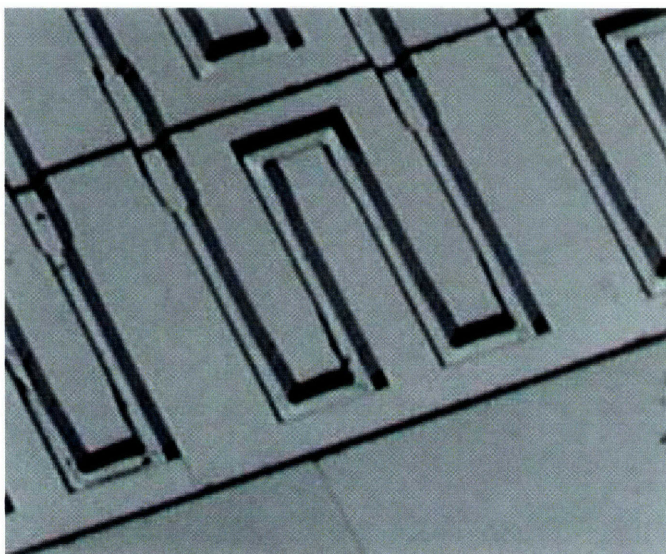
Figure 4-8. KOH etching results for original channel layout.

The weaknesses mentioned above were addressed in the second design of the micro fuel processor, the results of which are shown in Figure 4-9. The channel width was reduced to 600μm, resulting in a KOH etch that self-terminated at a depth of approximately 420μm. Also, the channel passes were spaced closer together, increasing the total channel length from 42 mm to 58 mm. In order to accommodate this feature, the corner compensation structures were modified slightly, leading to imperfect convex corners in the etched wafers. In addition to the modified channel layout, thin lines were incorporated perpendicular to the inlets and outlets of the channels. Once etched, these lines led to corner blowouts in which reactor tubes could be housed during the brazing step. This feature yielded reactors that were easier to braze and more structurally stable than those generated during the first fabrication run.
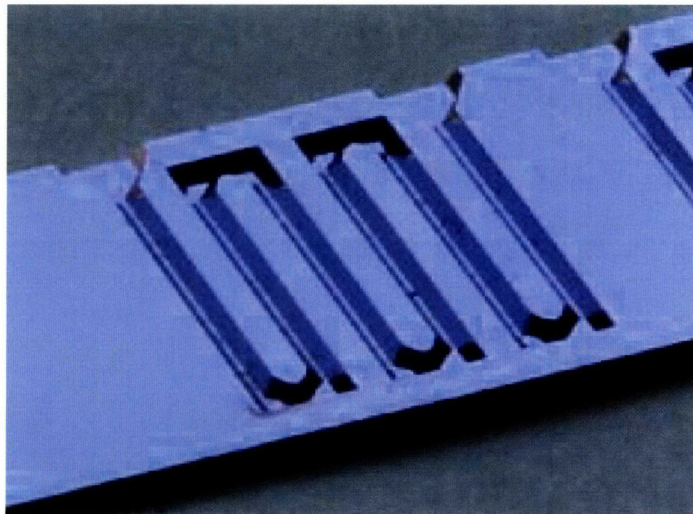
Figure 4-9. KOH etching results for modified channel layout.

A final fabrication run was performed using corner compensation features similar to those shown in Figure 4-5. The resulting reactor channel pattern is shown in Figure 4-10. The use of the new features allowed for a fourth turn in the channel layout. The channel width was reduced to 500μm, resulting in a KOH etch that self-terminated at a depth of approximately 350μm.
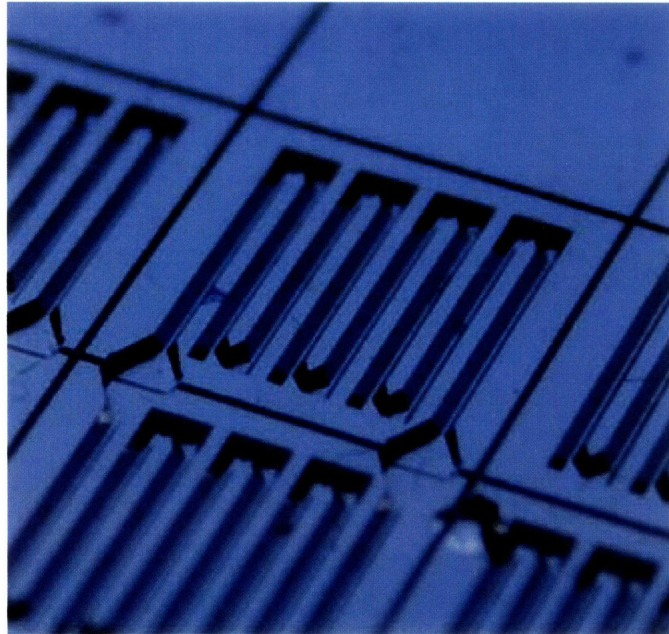
Figure 4-10. KOH etching results for reactors employing newest corner compensation features.

4.3.2 Brazed Reactors

Originally, sealant was applied to both the tube-reactor interface and the tube-frame interface (Figure 4-11a). However, the stresses induced by thermal expansion of the reaction zone chip led to cracking of the tubes and sealant after several thermal cycles. To mitigate this problem, the sealant at the tube-frame interface was replaced with epoxy, as shown in Figure 4-11b.
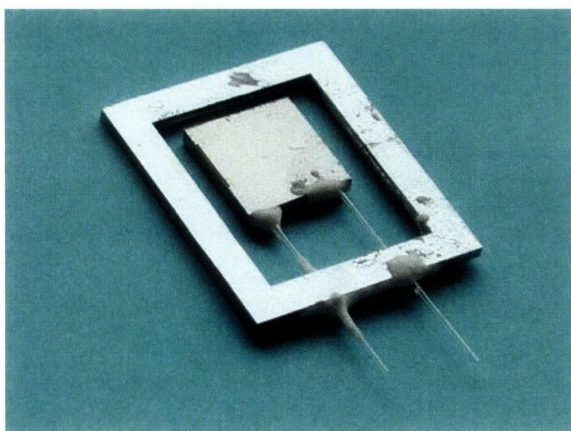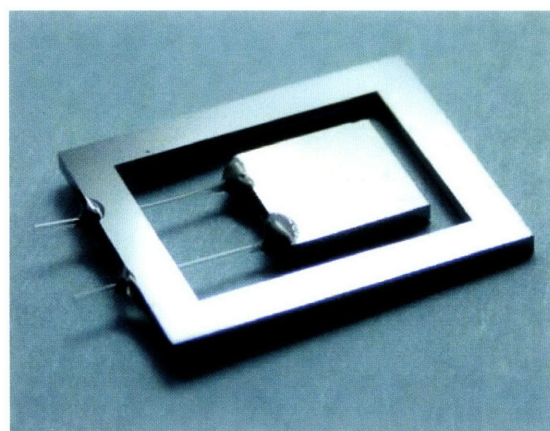
(a)   (b)

Figure 4-11. Photos of completed SμRE IV with silicon frame. Note that in (b) the sealant at the frame has been replaced with epoxy.

As mentioned previously, a scheme was developed to braze the reactors without using the silicon frame. Figure 4-12 shows examples of reactors brazed using this setup.
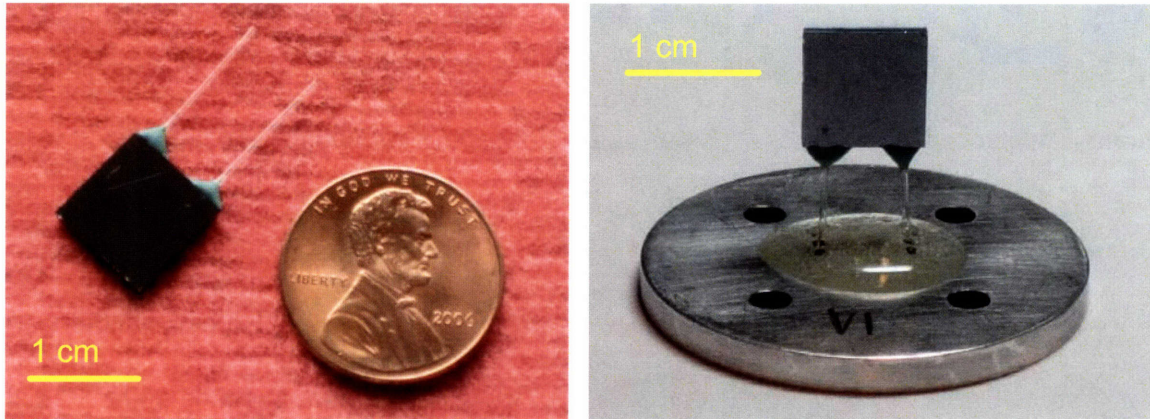
Figure 4-12. Photos of completed SμRE IV without silicon frame.

4.3.3 Multiple Reactor Bonding

In order to operate SμRE IV in the configuration outlined in Figure 3-5, multiple reactors must be bonded. Multiple SμRE IV reactors were bonded by placing a 100 μm thick copper foil between the two surfaces to be bonded. The reactors were then placed in an oven and heated to 950 °C for 2 hours. A steel block was placed on top of the reactor stack to provide pressure. The resulting wafer stack is pictured in Figure 4-13. This method produced bonded reactors capable of surviving multiple cycles to 850 °C. Bond failure was never observed during chemical testing.
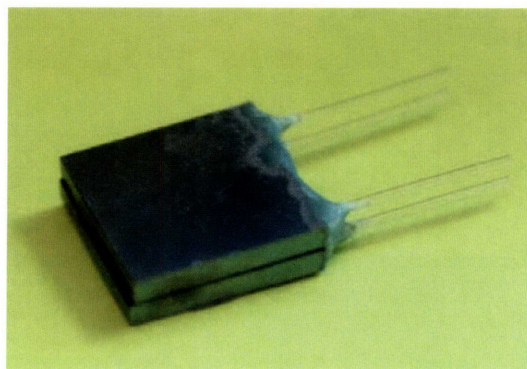
Figure 4-13. Two SμRE IV reactors bonded to form a stack.

4.4   Reactor Packaging

In order to test the fabricated microreactors, connections must be made to macroscopic testing tools such as mass flow controllers, gas chromatorgraphs, and mass spectrometers. Heat transfer and reaction analysis of the reactor requires testing in both ambient atmosphere and vacuum. The packaging schemes used during reactor testing are described below.

4.4.1 Vacuum Chamber

As previously mentioned, a scheme was devised to test SµRE IV without the use of a silicon frame (Figure 4-12). The reactor was epoxied to an aluminum frame. The frame was attached to a fluidic routing chuck via four screws. The attachment was kept air tight by placing a gasket between the routing chuck and the aluminum reactor frame. The routing chuck was placed into an aluminum vacuum chamber and sealed with an o-ring. The vacuum chamber includes a ¼" Swagelok fitting to which a vacuum line can be attached. Four holes in the bottom of the vacuum chamber house ceramic posts that insulate wiring and allow for electronic connections to the reactor under vacuum. The assembly is shown in Figure 4-14 and Figure 4-15. Once sealed, this setup allowed for both ambient testing and vacuum testing down to 16 mTorr.
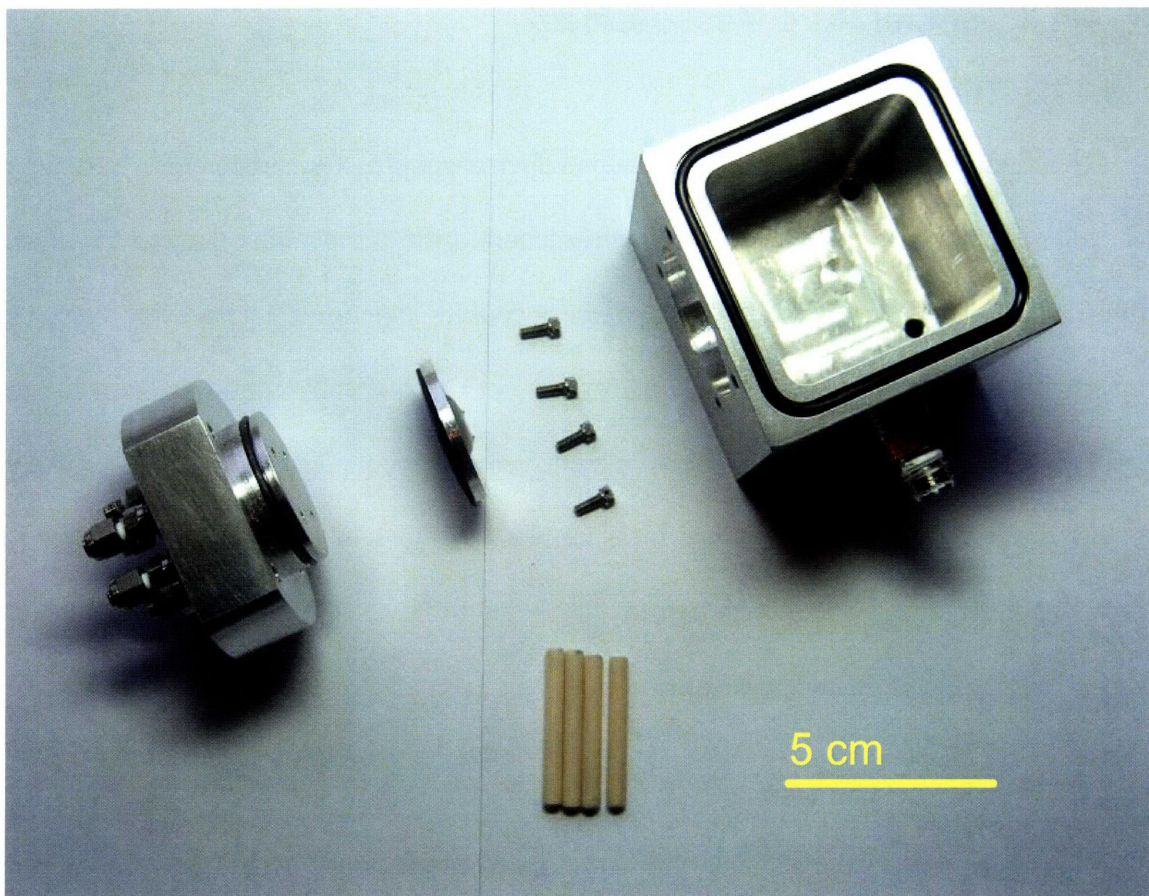
Figure 4-14. Packaging of reactor for chemical testing. This setup allowed for testing in both ambient atmosphere and vacuum at pressures as low as 16 mTorr.
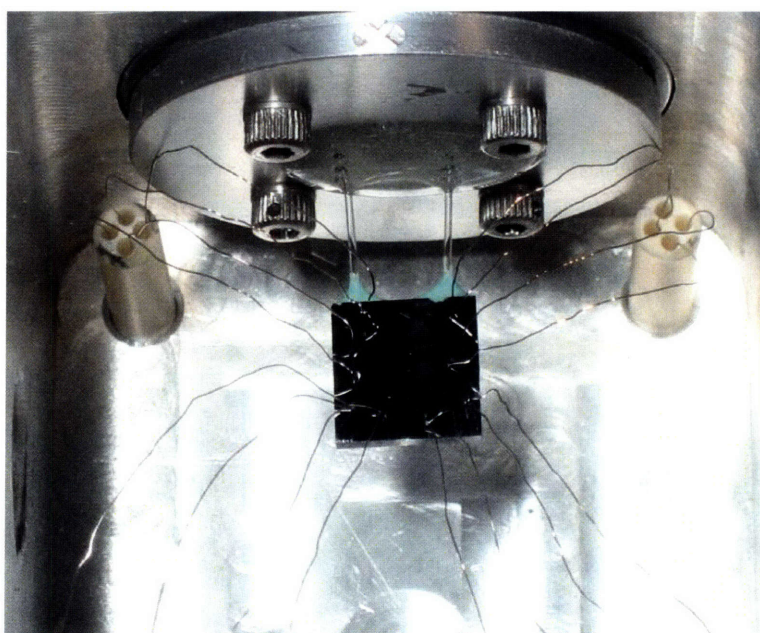
Figure 4-15. Assembled reactor for chemical testing.

4.4.2 Temperature Measurement

4.4.2.1 Thermocouples

The first set of experiments relied upon thermocouples for temperature measurement. The smaller the thermocouple used, the more accurate the temperature measurement due to minimization of heat losses from the thermocouple junction. However, very small thermocouples (e.g. 0.001" junction diameter) are not mechanically robust enough to survive multiple reaction runs. Temperature measurement via thermocouples was eventually abandoned as it was discovered that temperature measurements made with 0.01" thermocouples – the smallest size mechanically stable enough to survive multiple tests – yielded measurements that were inaccurate, especially under vacuum.

4.4.2.2 Infrared Camera

A FLIR Systems SC 1000 ThermaCam infrared camera was used to measure the reactor temperature for one set of experiments. These experiments were limited to low-temperature runs due to the limited range of the camera ($\leq 450°C$). In addition, measurements could only be taken with a direct line of sight to the reactor as no IR filter was available at the time of testing. Hence, temperature measurements could not be made when the reactor was in a vacuum environment. The IR transparency at temperatures below 550°C made it difficult to calibrate the infrared camera, and this method of temperature measurement was also ultimately abandoned.

4.4.2.3 Infrared Thermometer

The bulk of the testing was performed using a MICRO-EPSILON Optris LS infrared thermometer as the temperature sensing device. The Optris LS is sensitive to IR wavelengths between 9 and 12 microns at temperatures up to 900°C, allowing for easy measurement of high-temperature reactions. In addition, a ZnSe optical window was used for measurements in

vacuum. The ZnSe window included an anti-reflective coating that permitted the transmission of 96% of the infrared radiation between 9 and 14 microns. Calibration of the IR thermometer was achieved using OMEGALAQ temperature indicating liquids. The experimental setup is shown in Figure 4-16.
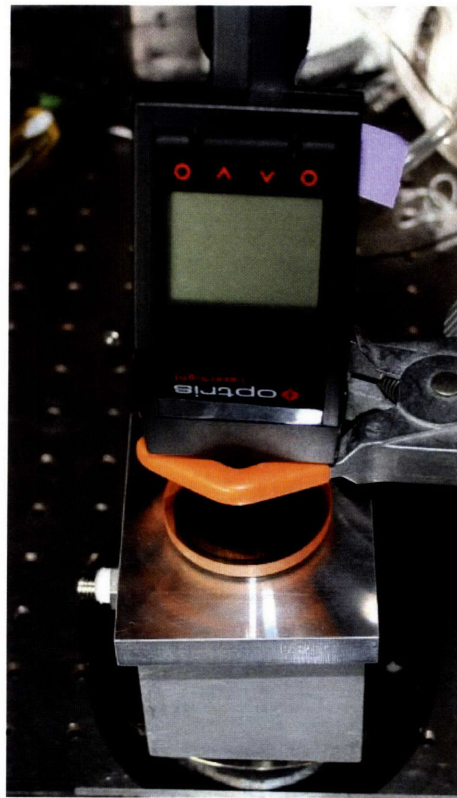
Figure 4-16. Infrared thermometer experimental setup.

Chapter 5   Heat Transfer Analysis

The efficiency of any fuel reformer scales inversely with the amount of energy lost from the system. In the case of the micro fuel processor, system inefficiencies are manifest as heat lost from the system. Therefore, in order to determine whether the micro fuel processor will be suitable for portable power applications, a thorough understanding of its thermal performance must be developed.

This chapter studies the various modes of heat loss from the micro fuel processor, and these results are used to generate an overall energy balance from the system. The calculations are then compared to experimental results generated in the laboratory.

5.1   Theoretical Steady-State Heat Loss

As mentioned in Section 3.5, the micro fuel processor is designed to produce electricity in one of two ways: by powering a photovoltaic generator or by coupling an exothermic combustion reaction with an endothermic fuel reforming reaction. In both of these cases, a steady-state combustion reaction is run to power the device. During steady-state combustion, heat is lost via several mechanisms including: conduction through the tubes, natural convection from the reactor and tubes, radiation from the reactor and tubes, and enthalpic losses from the heated gas exhaust. These mechanisms are outlined in detail below.

5.1.1 Losses from the Reaction Zone

The bulk of the potential thermal losses occur from the silicon reaction zone. The three pathways for thermal losses include convection and conduction through the ambient air, radiation from the silicon reactor, and conduction down the glass capillary inlet and outlet tubes.

Each of these losses will be outlined in detail below, and their relative importance will be compared.

5.1.1.1 Conduction from the Capillary Tubes

In Section 2.3.1, the linearized form of Fourier's Law was used to estimate the amount of heat lost via conduction for various sizes of tubing:

$$q = -kA\frac{\Delta T}{\Delta L}$$ (2-2b)

Equation 2-2b can be used to estimate the amount of conductive energy losses from SµRE IV under isothermal, steady-state conditions when convection and radiation from the tubes are ignored. The value of the conductive heat transfer coefficient, k, is 1.1 $Wm^{-1}K^{-1}$ for borosilicate glass. The cross-sectional area of a 550-µm OD, 400-µm ID round capillary is 1.12×10^{-7} m^2. For a 700-µm OD, 500-µm ID round capillary, the cross-sectional area is 1.88×10^{-7} m^2. SµRE IV made use of 10 mm-long capillary tubes. Figure 5-1 illustrates the amount of energy lost via conduction as a function of steady state operating temperature for the two types of capillaries used in the design.
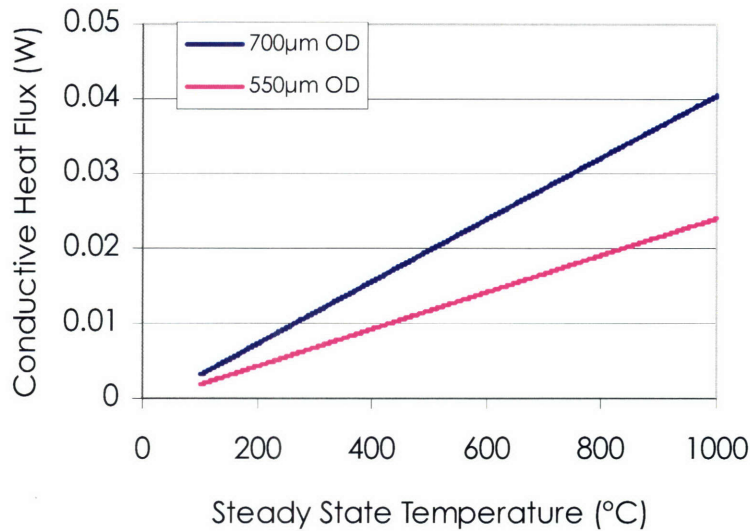
Figure 5-1. Calculated estimate of conductive heat losses from two tubes in SµRE IV under isothermal, steady-state conductions. The 700-µm capillary tubing has an inner diameter of 500 microns, while the 550-µm capillary tubing has an inner diameter of 400 microns.

From Figure 5-1, the amount of heat lost via conduction through both tubes during operation at 700°C is between 0.015 and 0.035 W. As will be seen later, this is a small number compared to other heat loss mechanisms. It should be noted that under real operation, the amount of heat lost through the tubes will be significantly larger than these numbers, due to the contribution of radiation – and, during ambient operation, convection – from the external surfaces of the tubes.

5.1.1.2 Natural Convection

As discussed in Section 2.3.2, heat loss due to convection (natural and forced) from a high-temperature region to a low-temperature ambient can be described by Newton's Law of Cooling:

$$q = h \, A \, dT \tag{2-3}$$

The primary challenge in calculating the theoretical convective heat losses from SμRE IV is determining the value of the convective heat transfer coefficient, h. Given the closed-package design of SμRE IV, natural convection should be the primary contributor to heat losses, and forced convection from the exterior surface can be ignored.

The convective heat transfer coefficient for natural convection in air can be calculated as [10]:

$$h = b(\Delta T)^m L^{3m-1} \qquad (5\text{-}1)$$

In Equation 5-1, ΔT is the temperature difference between the hot surface and the ambient, L is the characteristic length of the system, and b and m depend on the orientation of the hot surface. Values of b and m for various orientations are outlined in Table 5-1.

Table 5-1. Orientation dependence of b and m in Equation 5-1

Hot Surface Orientation	b	m
Vertical	1.37	0.25
Horizontal, facing up	1.86	0.25
Horizontal, facing down	0.88	0.25

SμRE IV includes six surfaces from which heat can be lost via natural convection. One of these surfaces is horizontal and faces up, another is horizontal and faces down, and the other four are vertically oriented, although one of the four vertically oriented surfaces is covered with sealant once the reactor is assembled. Using the coefficients in Table 5-1, the overall convective heat losses from an isothermal reactor in ambient atmosphere can be calculated. The results are illustrated in Figure 5-2.
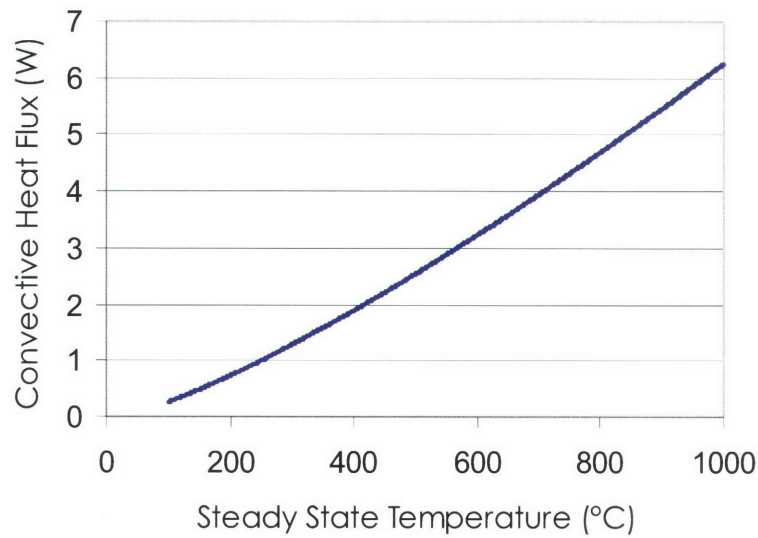
Figure 5-2. Calculated estimate of convective heat losses from the silicon reaction zone in SµRE IV under isothermal, steady-state conductions. Note that this estimate does not include convective losses from the sealant or capillary tubes.

From Figure 5-2, the amount of heat lost via natural convection from the reactor faces during operation at 700°C is nearly 4 W. Clearly, this represents a large amount of energy loss for a 1 W fuel processor, and therefore, the micro fuel processor must be packaged under vacuum in order to operate efficiently.

In order to determine the pressure at which most of the convective heat losses are eliminated, one must calculate the mean free path for convection given the geometry of the reactor. The mean free path for convection can be calculated as:

$$\lambda = \frac{RT}{\sqrt{2}\pi d^2 N_A P} \tag{5-2}$$

In Equation 5-2, R is the ideal gas constant, T is the temperature of the gas, d is the diameter of the gas molecules, N_A is Avagadro's number (6.02×10^{23}), and P is the pressure of the gas. Assuming that the external package of the reactor remains under 50°C, the mean free path varies with vacuum pressure as shown in Figure 5-3.
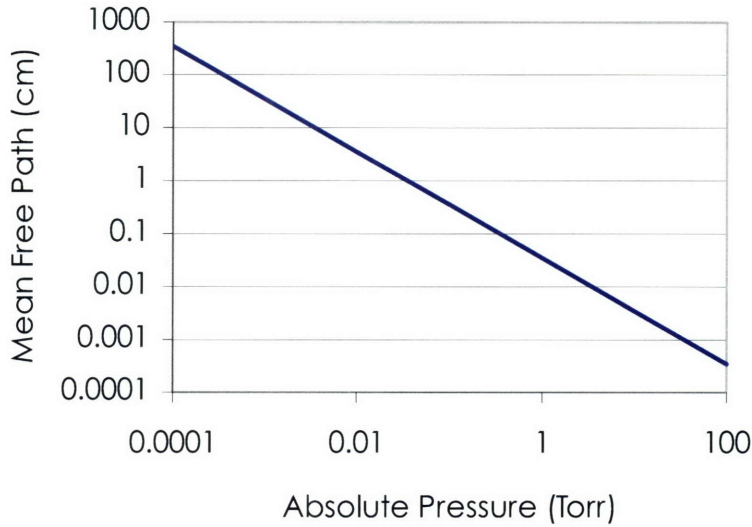
Figure 5-3. Mean free path between collisions as a function of absolute pressure. Note that 760 Torr = 1 atm.

In the case of SµRE IV, the final package will include a distance of no more than 0.25 cm between the reactor and external frame. For testing purposes, however, the distance between the chuck and the reactor is 2.5 cm. In order to eliminate convective heat losses during testing, the chuck pressure must be lowered to at least 13 mTorr.

5.1.1.3 Radiation

As discussed in Section 2.3.3, the amount of energy lost via radiation can be calculated as:

$$q = \varepsilon_H \sigma A_H (T_H^4 - T_C^4) \tag{2-5}$$

In Equation 2-5, q is the rate of radiative heat loss, ε_H is the emissivity of the gray body emitter, σ is the Stefan-Boltzmann constant (5.7×10^{-12} W·cm^{-2}·K^{-4}), and A_H is the external surface area of the gray body emitter. Radiative losses can be particularly large in high-temperature systems as reflected in the fourth-order dependence on temperature.

In determining the amount of heat energy lost as radiation, one must determine the emissivity, ε_H, of the hot material. In the case of silicon, as shown in Figure 5-4, the emissivity varies widely with temperature and emitted wavelength.
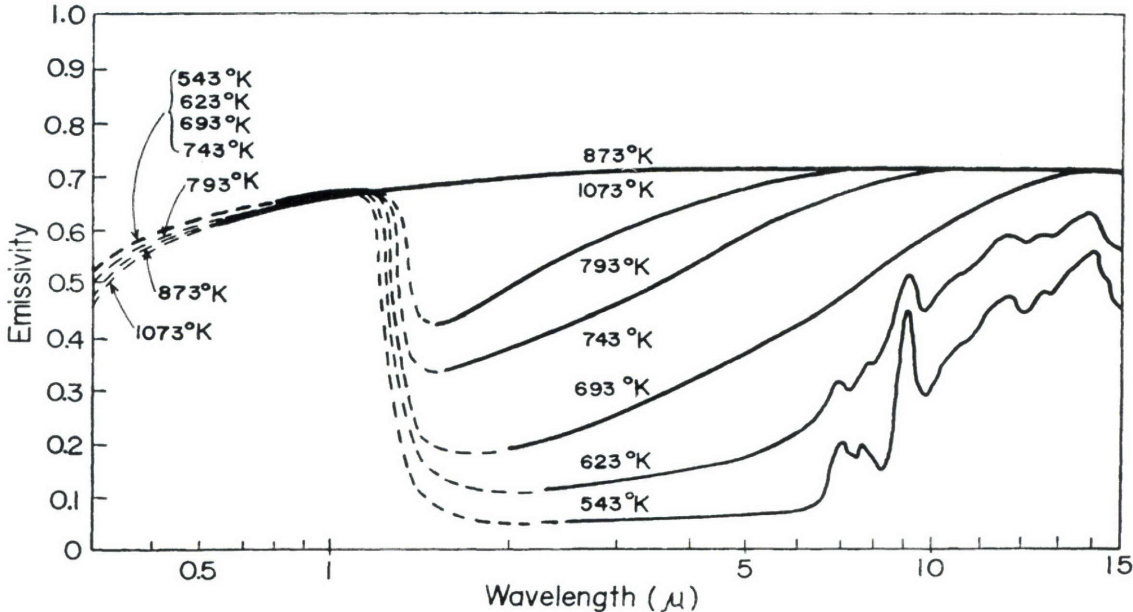
Figure 5-4. Spectral emissivity of pure silicon. From [61].

Figure 5-4 shows that the emissivity of silicon varies between 0.60 and 0.71 at the temperatures and wavelengths of interest. Using these values as lower and upper limits, the amount of heat energy lost via radiation was calculated for SμRE IV at various steady-state temperatures. The results are shown in Figure 5-5.
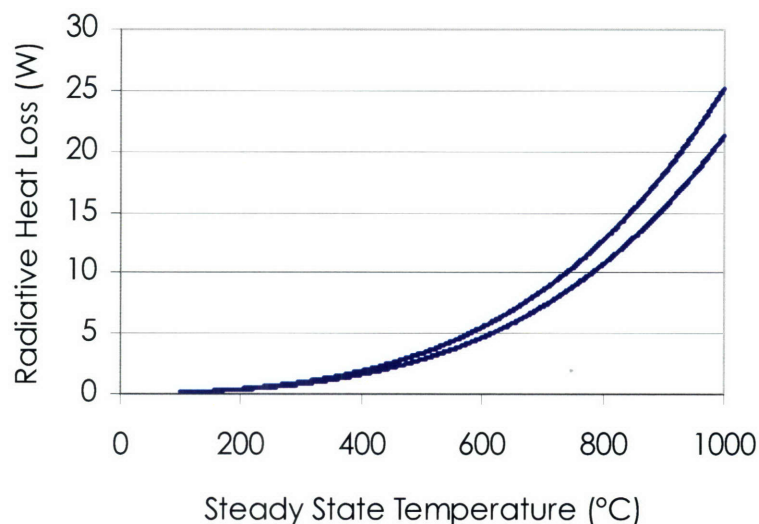
Figure 5-5. Lower and upper limits of calculated radiative heat losses from the silicon reaction zone in SμRE IV under isothermal, steady-state conductions. Note that this estimate does not include radiation losses from the sealant or capillary tubes.

From Figure 5-5, the amount of heat lost via radiation from the reactor faces during operation at 700°C is around 8 W, nearly twice the amount lost via natural convection in ambient atmosphere. Also, at higher temperatures, variations in the emissivity of the material have a larger effect on the amount of heat lost than at lower temperatures. This effect is expected due to the fourth-order dependence of radiative heat loss on temperature. For the rest of the calculations in this chapter, an emissivity of 0.65 will be used for silicon. This value is consistent with the measured apparent emissivity of SμRE IV in the laboratory.

5.1.1.4 Pathway Comparison

The three pathways for heat loss from the reaction zone have been plotted in Figure 5-6. The potential heat losses from the reaction zone are quite large (~30 W) for a system in which 1 W of power generation is the goal. However, a large percentage of these losses can be eliminated by strategic packaging of the reactor.

At low temperatures (i.e. < 400 °C), natural convection is the dominant form of heat loss. However, at higher temperatures, radiation becomes more dominant. The temperature at which this transition occurs depends upon two factors: the size of the reactor and the extent to which forced convection is occurring from the reactor surface. In situations where forced convection is present, such as a vented laboratory hood, convection may play a larger role in transporting heat away from the reactor zone. In the case of reactor size, smaller reactors lose heat via natural convection more quickly due to the reduced characteristic length for convection. For this reason, one would expect a small reactor to lose a higher percentage of its heat via natural convection than a large reactor.
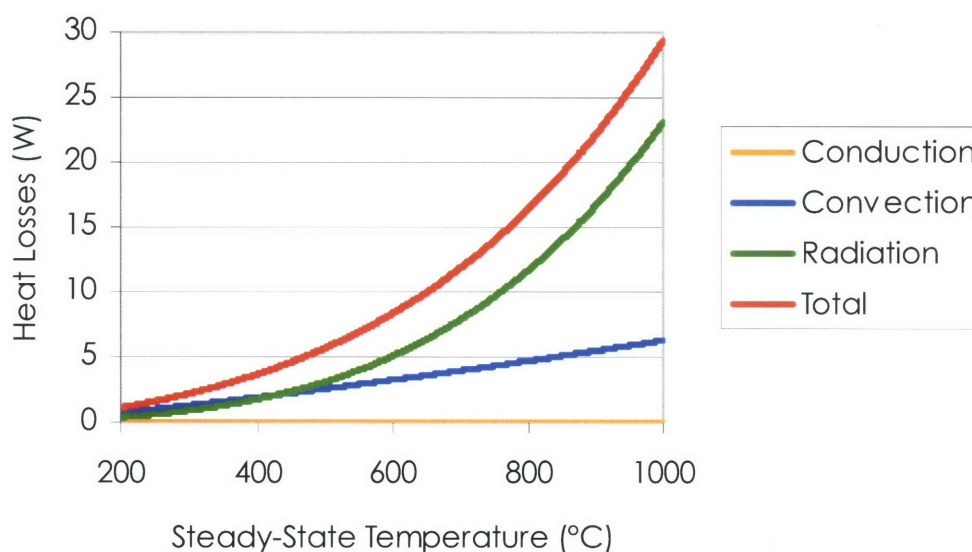
Figure 5-6. Comparison of heat loss pathways from the silicon reaction zone in SμRE IV under isothermal, steady-state conductions. Note that this estimate does not include radiation losses from the sealant or capillary tubes.

5.1.2 Convection and Radiation from Glass Sealant

The glass sealant connecting the capillary tubes to the reaction zone also contribute to the heat losses in the system. While the glass is not isothermal in practice, a quick estimate requires that one assume isothermal behavior. Assuming that the sealant is 3 mm wide and extends

1.5 mm from the reaction zone, one can apply Equations 2-3 and 2-5 to determine the heat losses from the sealant. These losses are summarized in Figure 5-7.
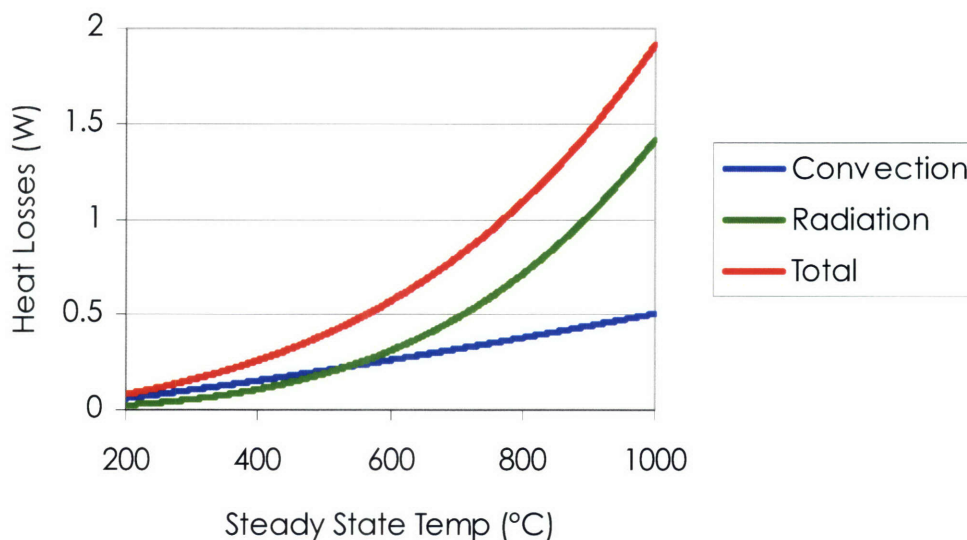
Figure 5-7. Calculated estimate of convective and radiative losses from the glass sealant in SμRE IV under isothermal, steady-state conductions.

Figure 5-7 illustrates that, while the losses from the glass sealant are not as large as those from the silicon reaction zone, they are significant and must be considered when calculating the overall heat balance in the system. Unfortunately, the size and shape of the brazed sealant varies from reactor to reactor, introducing error into the heat loss estimates. In addition, the glass sealant is not isothermal during combustion; a significant portion of the inlet sealant is cooled by the room temperature inlet gases to several hundred degrees below the operating temperature of the silicon reaction zone. Therefore, the estimated heat loses from the glass sealant are an overestimate compared to observed values.

5.1.3 Losses via Exhaust Gases

The final pathway for heat loss in the system is via the heated exhaust gases. The amount of heat lost via the exhaust gases can be calculated as

$$q = mC_p \Delta T \tag{5-3}$$

In Equation 5-3, *m* represents the mass flow rate, *Cp* is the heat capacity of the gas, and *ΔT* is the difference in temperature between the exhaust and inlet gases. Since lower heating values will be used in later sections, the amount of energy lost due to the vaporization of water will be ignored.

In order to calculate the amount of heat lost via the exhaust gases, it is assumed that the exiting gas is uniform in temperature equal to that of the silicon reaction zone. While it is possible that the average temperature of the exiting gases will be slightly lower than the silicon reactor, assuming uniform temperature should produce reasonable results. In addition, these calculations assume that the inlet gases are fed at a 2:1 stoichiometric ratio of oxygen to fuel, and full conversion is achieved in the reactor. Finally, it is assumed that the heat capacities of the gases are constant over the temperature range of interest. Using Equation 5-3 and the assumptions listed above, the percentage of generated heat – based on lower heating value – lost in the exhaust gases has been calculated and plotted for several fuels in Figure 5-8.
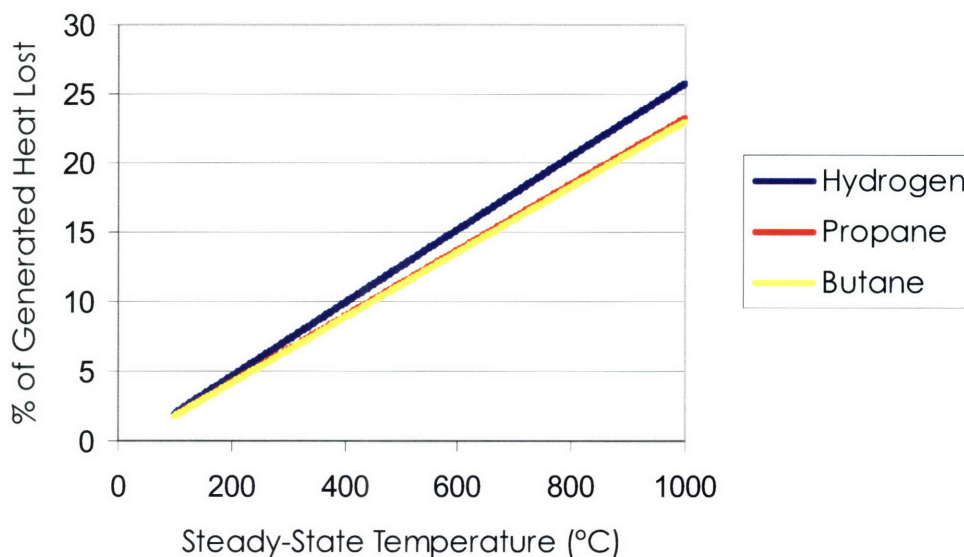
Figure 5-8. Percentage of generated heat lost via heated exhaust gases from SμRE IV under isothermal, steady-state conductions.

From Figure 5-8, the amount of heat lost via the exhaust gases is between 16% and 18% during operation at 700°C. The combustion of hydrogen results in slightly more losses via the exhaust gases than other fuels because proportionately more moles of gas are generated per watt of generated combustion energy. Unfortunately, heat loss via the exhaust gases cannot be reduced without redesigning the reactor to include heat exchange between the inlet and outlet tubes.

5.1.4 Overall Energy Balance

Using the heat loss analysis above, an overall energy balance for the system can be derived for steady state combustion with various fuels. The overall energy balance can be used to make predictions of reactor performance for different flow rates of fuels and steady-state reactor temperatures. In a steady-state system, the energy generated by the combustion of the fuel will be equal to the amount of heat energy lost from the system.

For the overall heat balance analysis, several assumptions are made. First, it is assumed that the fuel is completely combusted. This assumption ensures that the results obtained from the analysis will describe the reactor when operating at its highest kinetic efficiency. Another assumption is that the combustion reaction serves as the sole source of heat in the system. As previously mentioned, the reactor is assumed to be operating isothermally; in practice, there are significant thermal gradients across the chip. Finally, this analysis assumes that conductive heat transfer in the tubes is not enhanced by radiative and convective heat transfer from the outer surfaces of the capillaries.

Figure 5-9 and Figure 5-10 show the predicted steady-state heat loss from SμRE IV as a function of fuel flow rate at 400°C for hydrogen and propane, respectively. Steady-state operating points occur where the green line – corresponding to the amount of energy generated via combustion of the fuel – intersects the heat loss line – shown in blue and red. From Figure 5-9, one can deduce that the combustion of 13.5 sccm of hydrogen are required to sustain a steady-state temperature of 400°C under vacuum while 25.5 sccm of hydrogen are required in ambient. Similarly, Figure 5-10 shows that the complete combustion of 1.4 sccm of propane are required to sustain a steady-state temperature of 400°C under vacuum while 3.0 sccm of propane are required in ambient. In both cases, it is immediately evident that operation under vacuum is essential in maximizing the overall efficiency of the fuel processor.
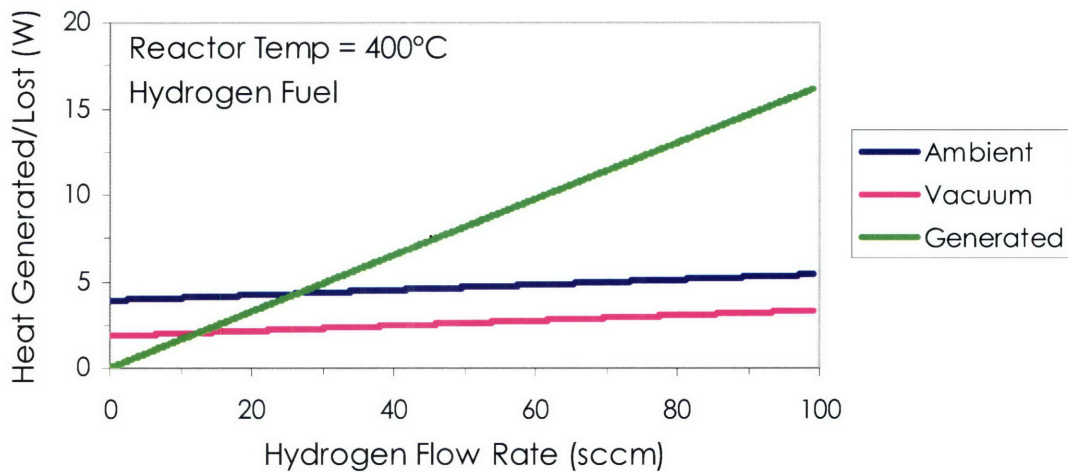
Figure 5-9. Predicted steady-state heat loss and energy generation in SµRE IV at 400°C as a function of hydrogen inlet flow rate. The heat generation line corresponds to the full combustion of fuel at a 2:1, oxygen to fuel stoichiometric ratio.
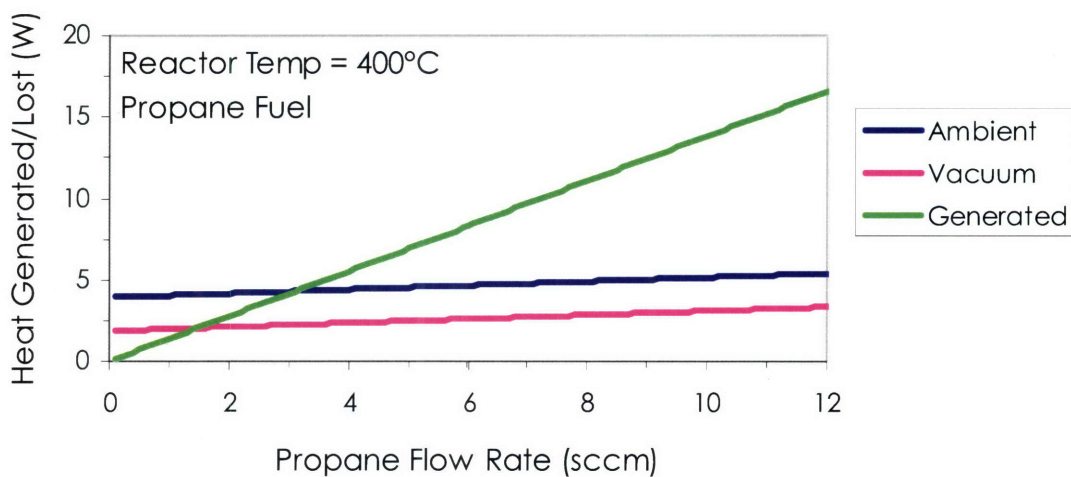
Figure 5-10. Predicted steady-state heat loss and energy generation in SµRE IV at 400°C as a function of propane inlet flow rate. The heat generation line corresponds to the full combustion of fuel at a 2:1, oxygen to fuel stoichiometric ratio.

A similar analysis can be performed for any desired steady-state operating temperature. Figure 5-11 and Figure 5-12 show the predicted steady-state heat loss from SµRE IV as a function of fuel flow rate at 550°C for hydrogen and propane, respectively. In this case, 31 sccm of hydrogen are required to sustain a steady-state operation under vacuum while 50 sccm of

hydrogen are required in ambient. To sustain a steady-state temperature of 550°C via propane combustion, 3.7 sccm of propane are required under vacuum while 6.1 sccm of propane are required in ambient. For both hydrogen and propane, twice as much fuel is required to sustain a steady-state temperature of 550°C, compared to the amount needed to sustain 400°C.
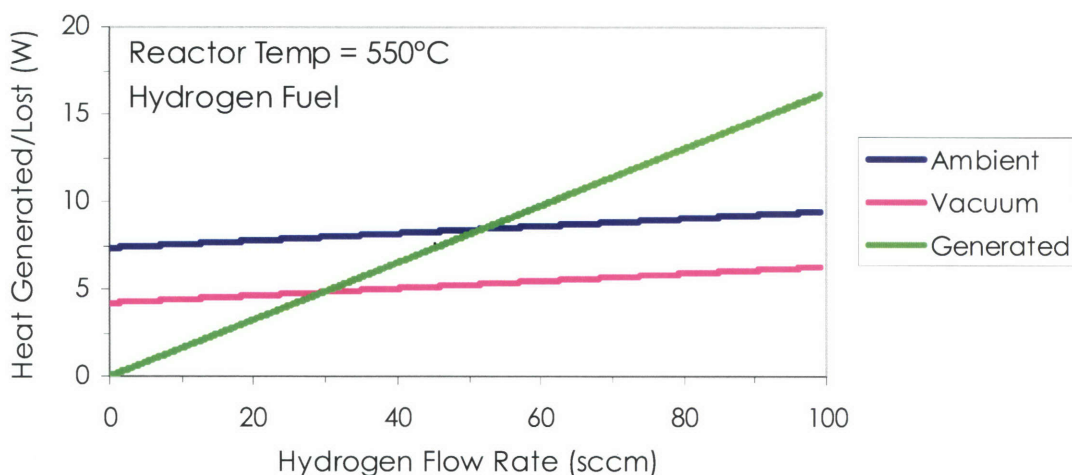
Figure 5-11. Predicted steady-state heat loss and energy generation in SμRE IV at 550°C as a function of hydrogen inlet flow rate. The heat generation line corresponds to the full combustion of fuel at a 2:1, oxygen to fuel stoichiometric ratio.
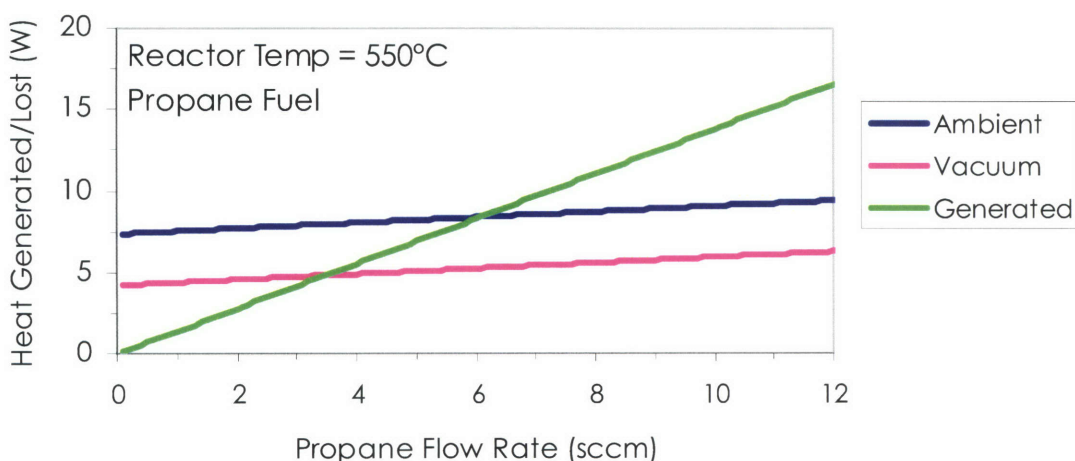
Figure 5-12. Predicted steady-state heat loss and energy generation in SμRE IV at 550°C as a function of propane inlet flow rate. The heat generation line corresponds to the full combustion of fuel at a 2:1, oxygen to fuel stoichiometric ratio.

Figure 5-13 and Figure 5-14 show the predicted steady-state heat loss from SμRE IV as a function of fuel flow rate at 700°C for hydrogen and propane, respectively. In this case, the heat losses from the reactor are much more significant due to the fourth-order dependence of radiative losses on reactor temperature. 61 sccm of hydrogen are required to sustain a steady-state operation under vacuum while 92 sccm of hydrogen are required in ambient. To sustain a steady-state temperature of 700°C via propane combustion, nearly 7 sccm of propane are required under vacuum while 10.5 sccm of propane are required in ambient. Again, for both hydrogen and propane, nearly twice as much fuel is required to sustain a steady-state temperature of 700°C, compared to the amount needed to sustain 550°C. Also noteworthy is that with each increase in temperature, the percentage of heat losses eliminated by operating in vacuum decrease due to the relatively larger amount of heat lost via radiation.
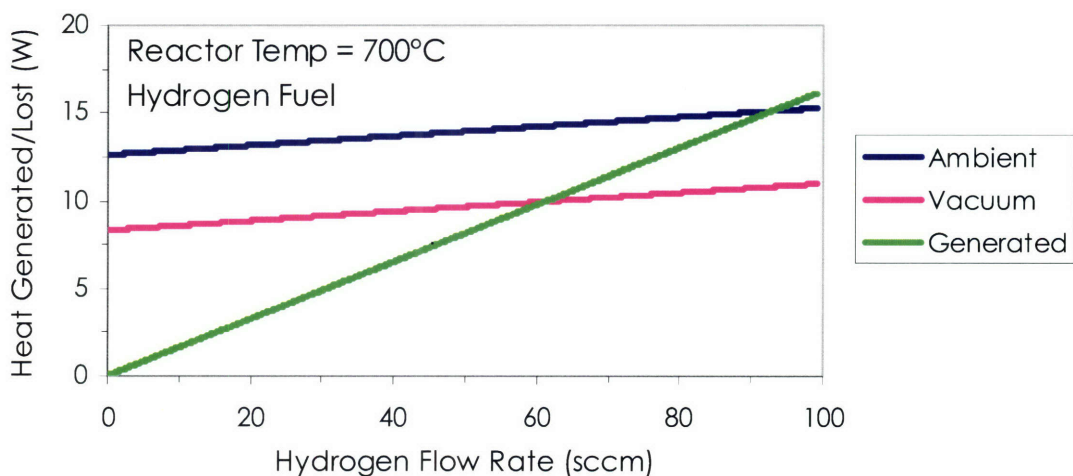
Figure 5-13. Predicted steady-state heat loss and energy generation in SμRE IV at 700°C as a function of hydrogen inlet flow rate. The heat generation line corresponds to the full combustion of fuel at a 2:1, oxygen to fuel stoichiometric ratio.
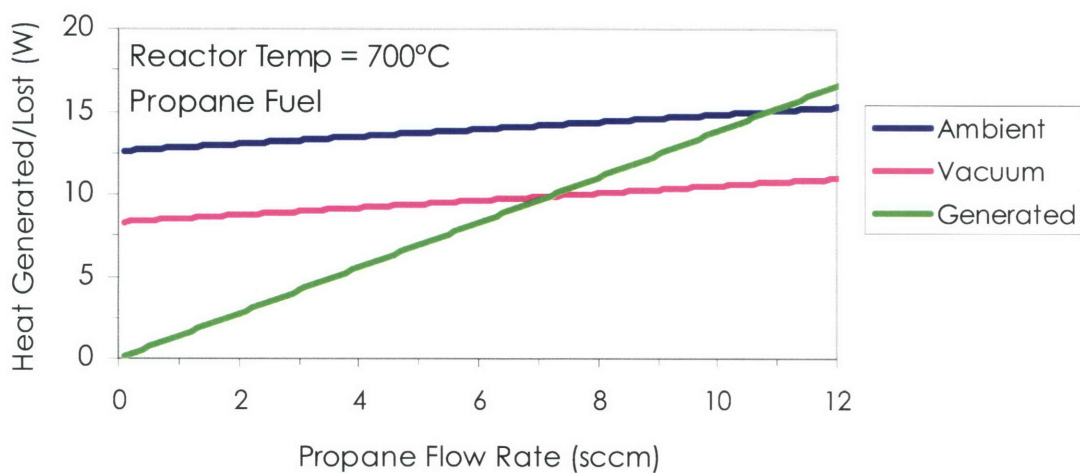
Figure 5-14. Predicted steady-state heat loss and energy generation in SμRE IV at 700°C as a function of propane inlet flow rate. The heat generation line corresponds to the full combustion of fuel at a 2:1, oxygen to fuel stoichiometric ratio.

Using the steady-state operating points gathered from plots such as those in Figure 5-9 to Figure 5-14, one can construct a plot of steady-state autothermal combustion temperatures for various fuel flow rates. Figure 5-15 and Figure 5-16 show two such plots for hydrogen and propane in which 2:1 stoichiometric ratios of oxygen to fuel are fed. In both cases, for a given flow rate, much higher temperatures can be reached under vacuum than in ambient.
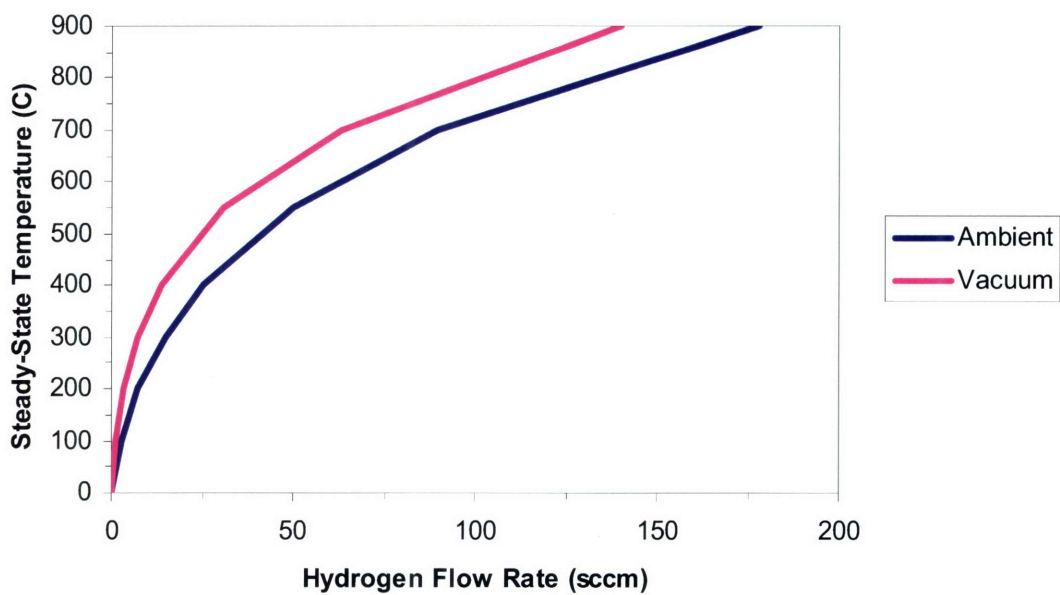
Figure 5-15. Predicted autothermal steady-state temperature of SμRE IV during complete conversion of hydrogen.
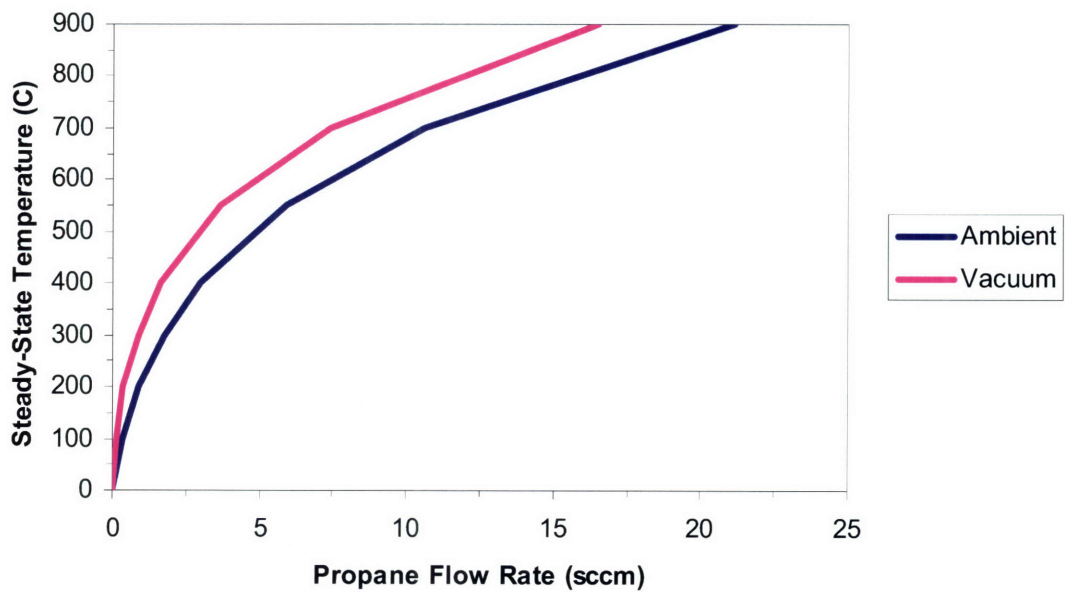
Figure 5-16. Predicted autothermal steady-state temperature of SμRE IV during complete conversion of propane.

Chapter 6   Chemical Reaction Testing

For hydrogen generation via autothermal endothermic reforming, several SμRE IV reactors must be bonded as shown in Figure 3-5. In this case, the heat generated by the exothermic combustion is used to drive the endothermic reforming reaction. When coupling SμRE IV with a set of TPV cells to generate power – as shown in Figure 3-6 – only one reactor is required. In both cases, a thorough understanding of the reactor performance when running an autothermal combustion reaction is required.

To test the performance of SμRE IV, catalytic combustion was carried out using several types of fuels including hydrogen, propane, butane, and ammonia. All of the results described in this chapter were obtained using reactors with the channel design depicted in Figure 4-9. Combustion testing was performed using two types of catalyst: 1wt% Pt on γ-Al$_2$O$_3$ and 5wt% Pt on γ-Al$_2$O$_3$.

6.1   Experimental Procedure

6.1.1 Test Setup

The experimental setup is outlined in Figure 6-1. All of the reactors used for combustion testing included channel geometries depicted in Figure 4-9. All experiments were run on a ventilated bench top using the aluminum chuck shown in Figure 4-14 and Figure 4-15. The reactor plate – shown in Figure 4-12 – was compressed against the aluminum fluidic chuck using a Kalrez® elastomer gasket to form a fluidic seal. Reactants were fed continuously using calibrated UNIT mass flow controllers (Model 1660 for ammonia and Model 1100 for all other gases). Swagelok 1/3 atm check valves were installed at each of the gas inlets to prevent upstream propagation of reaction fronts. The reactor exhaust was heated to 110 °C to prevent

condensation of water in the exhaust lines. Product gas compositions were analyzed on-line using an Inficon mass spectrometer, described in Section 6.1.2.
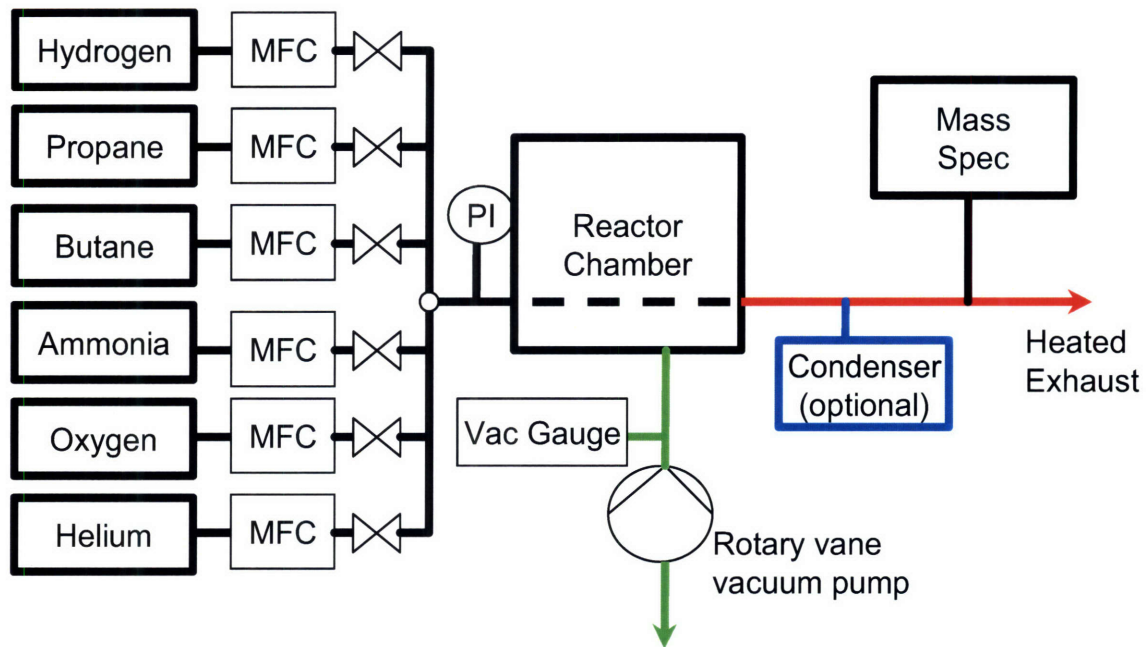
Figure 6-1. Experimental setup.

A two-stage condenser was installed between the heated exhaust line and the unheated capillary sampling line to remove water vapor from exhaust. The first stage of the condenser consisted of a 6-inch length of ¼-inch copper tube exposed to the ambient environment. A glass bulb immersed in a mixture of ethylene glycol and dry ice, with a sustained temperature of − 12 °C, served as the second condenser. Mass spectrometer readings indicated that over 99% of the water in the exhaust line was condensed using this method.

Experiments were performed in ambient atmosphere as well as under vacuum. For vacuum experiments, the aluminum chuck was evacuated using a rotary vane vacuum pump. Vacuum levels were measured with a Kurt J Lesker Co. KJL-6000 thermocouple gauge. Temperature measurements were made using a MICRO-EPSILON Optris LS infrared thermometer, with a spectral response between 8 and 14 μm. This thermometer measures the

average temperature across a 1-mm diameter spot size, the location of which is indicated by a laser sight. For vacuum experiments, a ZnSe window provided the necessary IR transparency between the IR thermometer and the hot reactor. This window was 94% transparent across the 8 to 14 μm spectrum. For ambient experiments, the IR thermometer was calibrated by applying a small spot of OMEGALAQ temperature indicating liquid on an isothermal section of the reactor and measuring the temperature adjacent to the spot. Liquids were available for temperatures between 300 °C and 850 °C in roughly 25 °C increments. For temperature calibration in vacuum experiments, only the following OMEGALAQ liquids were sufficiently resistant to sublimation: 399 °C, 621 °C, 649 °C, 677 °C, 704 °C, 816 °C, and 871 °C.

The catalysts used for the combustion reactions in which temperature data are reported were deposited from aqueous slurries of 5 wt.% Pt on La-doped γ-Al_2O_3. The catalyst was reduced *ex situ* in 100% hydrogen at 400 °C for one hour. For hydrogen combustion experiments, a 2:1 stoichiometric ratio of pure oxygen was fed as the oxidant. In the case of propane combustion, a 1.5:1 stoichiometric ratio of pure oxygen was fed. Auto-ignition was achieved in all combustion experiments by co-feeding hydrogen in the reactant stream. For propane and butane combustion, hydrogen flow rates were ramped down after ignition.

6.1.2 Chemical Analysis

The exhaust gases were analyzed using an Inficon Transpector2 mass spectrometer (MS). The Transpector2 is a quadrupole partial pressure analyzer capable of measuring the partial pressures of each species in a gas mixture. The MS samples gas at a fixed rate depending on the length of capillary tube used to supply the sample (~6 sccm of gas for the experiments run in this thesis). For most cases, the sample rate was small enough that the exhaust gases could be sampled directly. In low-flow cases, helium make-up gases were injected prior to sampling.

This practice was also employed when sampling flows with high concentrations of hydrogen to avoid chamber saturation.

Analyzing combustion products posed some challenges. High water concentrations in the exhaust stream caused condensation and plugging in the MS sampling valves. For this reason, a condenser was used when combustion products were analyzed. Also, since propane has the same molecular weight (44) as CO_2 – a by-product of its combustion – mass 29 was used to analyze propane concentrations. Combustion reaction conversions were calculated using mass 2 for hydrogen, mass 16 for ammonia, and masses 58 and 43 for butane.

6.1.3 Calculations

6.1.3.1 Reaction Stoichiometry

Several reactions have been run using SµRE IV including hydrogen, propane, butane, and ammonia combustion. In every case, the combustion reactions were run using either a 2:1 or 1.5:1 stoichiometric mix of oxygen to fuel. The stoichiometry for each of these reactions is outlined in Table 6-1.

6.1.3.2 Conversion

As these reactions proceed, the concentration of each gas is affected by two factors. First, the number of moles of reactants will be lowered as they are consumed in the reaction, while the number of moles of products is increased. Second, the overall number of moles will change depending on the stoichiometry of the reaction. The overall change in the number of moles present is described by the molar expansion ratio, δ, and is included in Table 6-1 for each reaction.

When calculating the conversion of species a, the molar expansion ratio is accounted for using the following formula:

$$X_a = \frac{1 - \dfrac{P_a}{P_{a,o}}}{1 + (\delta - 1)\left(\dfrac{P_a}{P_{a,o}}\right)}$$

(5-2)

In Equation 6-1, P_a represents the partial pressure of species a during testing, and $P_{a,o}$ is the partial pressure of species a in the inlet feed.

Table 6-1. Reaction Stoichiometry

2:1, Oxygen:Fuel Combustion	$\Delta n = n_{out} - n_{in}$	$\delta = n_{out}/n_{in}$
$H_2 + O_2 \rightarrow H_2O + 0.5\ O_2$	−0.50	0.75
$C_3H_8 + 10\ O_2 \rightarrow 4\ H_2O + 3\ CO_2 + 5\ O_2$	+1.00	1.09
$C_4H_{10} + 13\ O_2 \rightarrow 5\ H_2O + 4\ CO_2 + 6.5\ O_2$	+1.50	1.11
$NH_3 + 1.5\ O_2 \rightarrow 1.5\ H_2O + 0.5\ N_2 + 0.75\ O_2$	+0.25	1.10
1.5:1, Oxygen:Fuel Combustion		
$H_2 + 0.75\ O_2 \rightarrow H_2O + 0.25\ O_2$	−0.50	0.71
$C_3H_8 + 7.5\ O_2 \rightarrow 4\ H_2O + 3\ CO_2 + 2.5\ O_2$	+1.00	1.12
$C_4H_{10} + 9.75\ O_2 \rightarrow 5\ H_2O + 4\ CO_2 + 3.25\ O_2$	+1.50	1.14
$NH_3 + 1.125\ O_2 \rightarrow 1.5\ H_2O + 0.5\ N_2 + 0.375\ O_2$	+0.25	1.12
Ammonia Cracking		
$NH_3 \rightarrow 0.5\ N_2 + 1.5\ H_2$	+1.00	2

6.2   Hydrogen Combustion

Steady state hydrogen combustion was achieved for a wide variety of flow rates. The activation energy of hydrogen combustion over platinum is low, with reported values as low as 14.9 kJ mol^{-1} [62]. For this reason, light-off of the reactor was easily achieved. In fact, every reactor in which fresh catalyst was used (both 1wt% and 5wt%) could be ignited at room

temperature. In addition, 100% conversion was observed for all of the hydrogen flow rates tested. This is expected due to the fast diffusion of hydrogen from the bulk and the fast reaction kinetics. At high temperatures (>700 °C) and fuel rich mixtures of hydrogen and oxygen, homogeneous combustion was sometimes seen. This led to runaway temperatures, melting of the glass sealant and capillary tubes, and ultimately, reactor failure.

For every flow rate tested, a concentrated hot spot is seen where the reactants first meet the catalyst. These hot spots are illustrated in Figure 6-2.

(a)   (b)

Figure 6-2. Autothermal, steady-state combustion of 40 sccm hydrogen with 2.5 mg of (a) 1wt% Pt on Al_2O_3 and (b) 5wt% Pt on Al_2O_3.

Figure 6-2a shows the temperature profile for the complete combustion of 40 sccm hydrogen over 2.5 mg of 1wt% Pt on Al_2O_3. Figure 6-2b shows the temperature profile for the same flow rate over 5wt% Pt on Al_2O_3. In both cases, the temperature profile is nearly identical.

To determine whether the hydrogen combustion reaction is kinetic or diffusion limited, one can calculate the Thiele modulus. The Thiele modulus is the ratio of the reaction rate in the absence of mass transfer limitation to the rate of diffusion through the catalyst, and it is calculated as [63, 64]:

$$\Phi_s = \frac{r_p^2 (-r)}{D_{eff} C_s} \tag{5-3}$$

In Equation 5-3, r_p is the radius of the catalyst particle, r is the rate of reaction, C_s is the surface concentration of the fuel, and D_{eff} is the effective diffusion coefficient in the porous catalyst. In the case of SµRE IV, the catalyst particle radius can be approximated as the thickness of the catalyst layer (~50 µm). D_{eff} is calculated as:

$$D_{eff} = \frac{D_{12} \theta}{\tau} \tag{5-4}$$

In Equation 5-4, D_{12} is the bulk diffusion coefficient of the fuel. θ is the porosity, or void fraction, of the catalyst. For the alumina support, the void fraction was 0.6. τ is a tortuosity factor. Assuming the catalyst pores are randomly oriented cylinders, a value of 3 was used for τ.

Using the kinetic parameters outlined in Section 7.6, the Thiele modulus for hydrogen combustion in a 2:1 stoichiometric mix of oxygen to hydrogen at 600 °C is 15.9. This suggests that the operation of the reactor in Figure 6-2 is solidly in the diffusion limited regime, and the similarity between the temperature profiles, therefore, is an expected result.

Figure 6-3 and Figure 6-4 show the temperature profile of SµRE IV as a function of hydrogen flow rate at 1 atm and 16 mTorr chamber pressures, respectively.

Figure 6-3. Temperature profile of SµRE IV as a function of hydrogen flow rate in ambient environment. In all cases, a 2:1 stoichiometric ratio of oxygen to hydrogen was fed to the reactor, and 100% conversion was observed. Temperature measurements were made using an IR thermometer calibrated using Omega indicating lacquers.

Figure 6-4. Temperature profile of SµRE IV as a function of hydrogen flow rate at 16 mTorr vacuum. In all cases, a 2:1 stoichiometric ratio of oxygen to hydrogen was fed to the reactor, and 100% conversion was observed. Temperature measurements were made using an IR thermometer calibrated using Omega indicating lacquers.

Figure 6-3 and Figure 6-4 show that the experimental results are in fairly good agreement with the isothermal temperature predictions made in Section 5.1.4. In both cases, the predicted steady-state temperature – represented by the black line – lies between the upper and lower temperature extremes, although the predicted temperatures are closer to the lower end of the measured spectrum. This result is expected due to the high concentration of the hot spot in the reactor for hydrogen combustion.

In both ambient atmosphere and vacuum conditions, the temperature gradient across the chip increases with increasing flow rates. As flow rates are increased, more gas is available for combustion, leading to higher temperatures. Higher temperatures lead to large increases in the reaction rate and, to a lesser extent, increases in the diffusion coefficient of hydrogen. For example, using the kinetic parameters in Section 7.6, the reaction rate increases over two orders of magnitude from 0.30 moles cm^{-3} s^{-1} at 25 °C to 33.6 moles cm^{-3} s^{-1} at 800 °C. Regarding the diffusion effect, diffusion coefficient of hydrogen in argon increases an order of magnitude – from 0.83 cm^2 s^{-1} to 8.10 cm^2 s^{-1} – as temperature is increased from 22.3 °C to 796 °C [65, 66]. These effects create a positive-feedback loop that results in the concentration of the hot spot. In addition, the temperature gradients are larger under vacuum than they are in ambient. This effect can be explained in the same manner as the effect of increasing flow rates.

6.3   Propane Combustion

Steady-state, autothermal propane combustion was also achieved for a wide variety of flow rates. Temperatures of ~350°C were required to sustain propane combustion. For this reason, hydrogen was fed along with propane to achieve initial light-off of the reactor.

For every flow rate tested, a concentrated hot spot is seen in the half of the reactor where the reactants are injected. These hot spots are illustrated in Figure 6-5.

(a) **(b)**
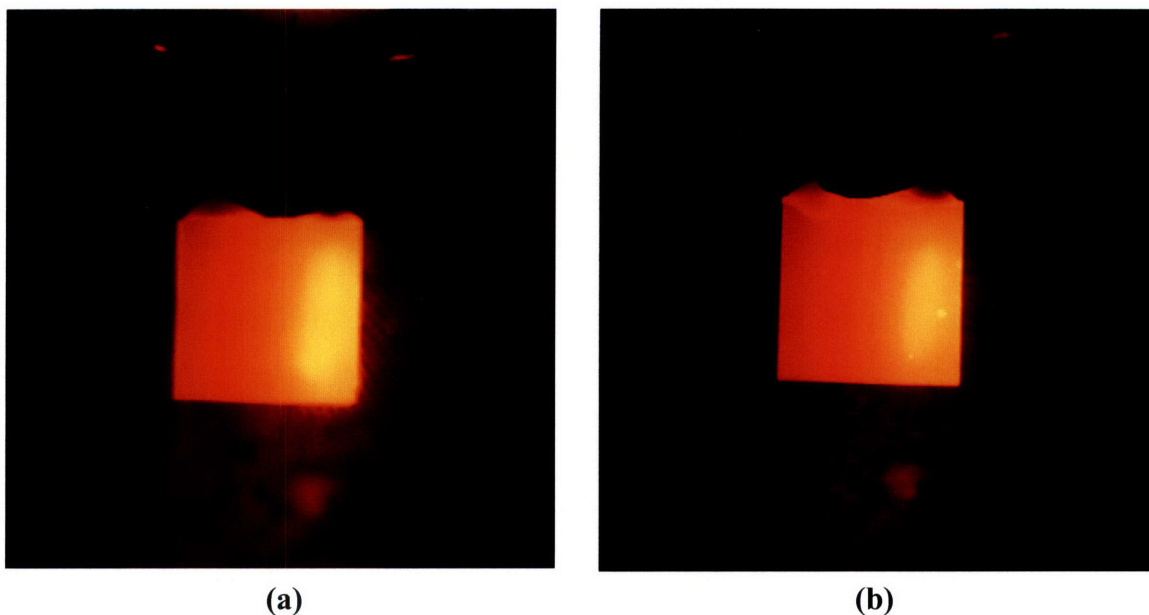
Figure 6-5. Autothermal, steady-state combustion of 13 sccm propane with 2.5 mg of (a) 1wt% Pt on Al_2O_3 and (b) 5wt% Pt on Al_2O_3.

Figure 6-5a shows the temperature profile for the complete combustion of 13 sccm propane over 2.5 mg of 1wt% Pt on Al_2O_3 while Figure 6-5b shows the temperature profile for 5wt% Pt on Al_2O_3. Again, the temperature profile is nearly identical in both cases. Again, one can calculate the Thiele modulus for propane combustion in order to determine whether the operation in Figure 6-5 is diffusion or reaction rate limited. Using the kinetic parameters in Section 7.6, the Thiele modulus for propane combustion at 800 °C is 0.79. This value suggests that neither diffusion nor reaction rate are limiting factors for the reaction in Figure 6-5. Given the similarity in the temperature profiles, this is an unexpected result. It is possible that during the crushing of the catalyst, the number of available surface sites was diminished to similar levels for both the 1wt% and 5wt% catalysts. The determination of surface site density by pulse chemisorption would be necessary to test this hypothesis.

Homogeneous combustion of propane was never seen, and – once steady-state combustion was achieved – the reaction was quite stable. For the vacuum experiments, 97%

conversion of propane was achieved at 6 sccm, and greater than 99% conversions were seen at 7 sccm and higher. Conversions higher than 99% could not be differentiated due to the noise in the baselines of the masses used to measure propane. As the flow rates were increased, the hot spot became more pronounced. Figure 6-6 and Figure 6-7 show the temperature profile of SµRE IV as a function of propane flow rate at 1 atm and 16 mTorr chamber pressures, respectively.
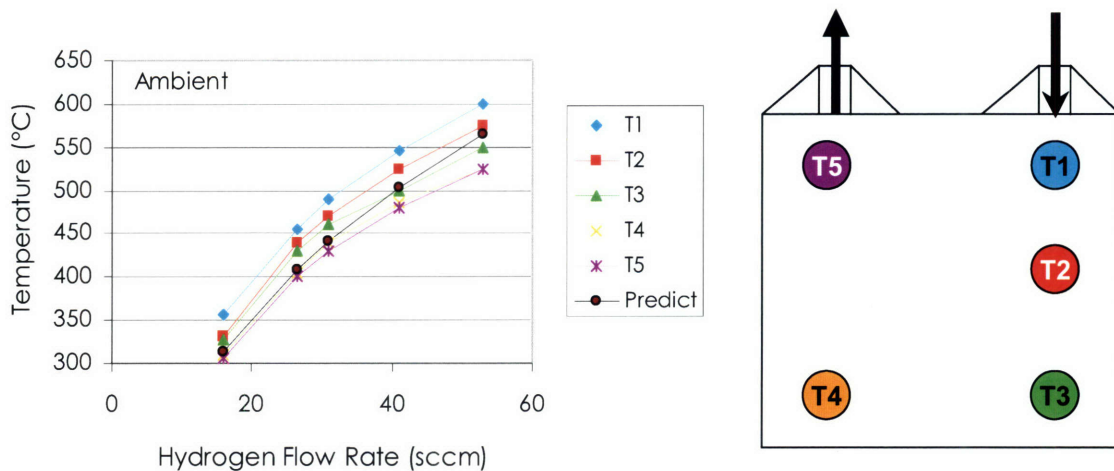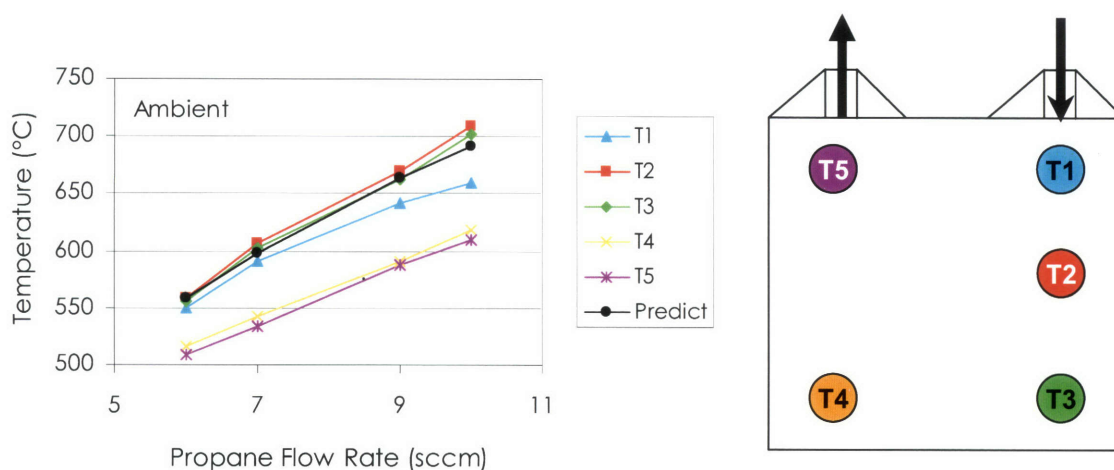

Figure 6-6. Temperature profile of SµRE IV as a function of propane flow rate in ambient environment. In all cases, a 1.5:1 stoichiometric ratio of oxygen to propane was fed to the reactor and 91%+ conversion was observed. Temperature measurements were made using an IR thermometer calibrated using Omega indicating lacquers.
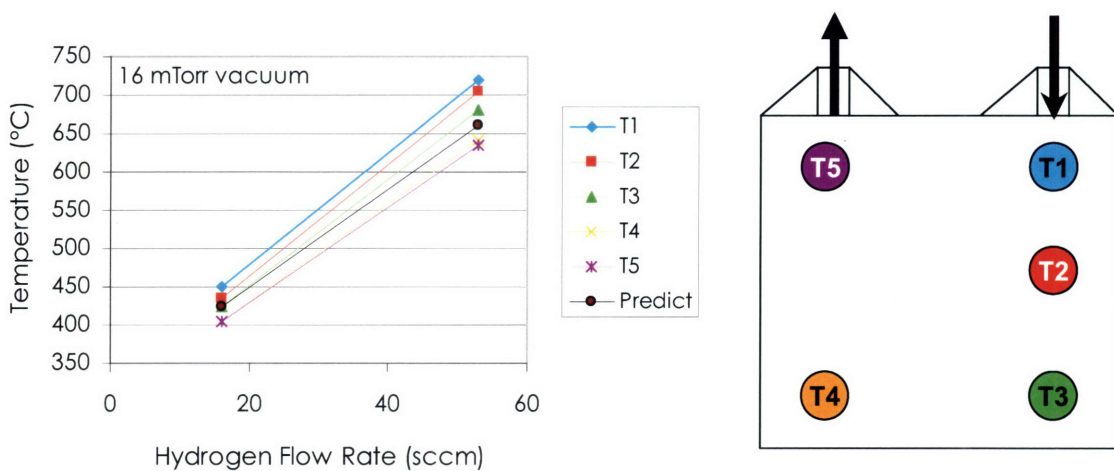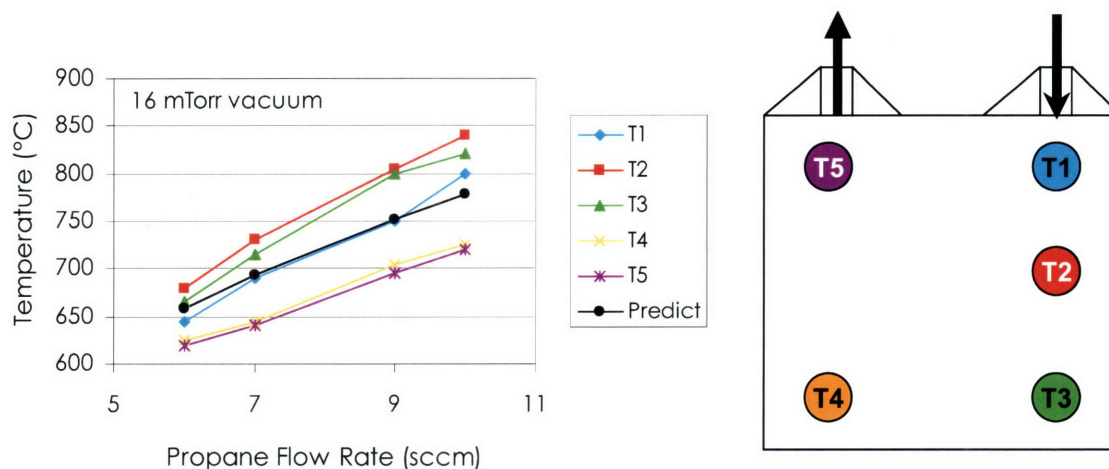
Figure 6-7. Temperature profile of SμRE IV as a function of propane flow rate at 16 mTorr vacuum. In all cases, a 1.5:1 stoichiometric ratio of oxygen to propane was fed to the reactor. 97%+ conversion was observed for propane flow rates of 6 sccm while greater than 99% conversions were observed for all other flow rates. Temperature measurements were made using an IR thermometer calibrated using Omega indicating lacquers.

Several observations can be made from Figure 6-6 and Figure 6-7. The experimental results are in fairly good agreement with the isothermal temperature predictions made in Section 5.1.4. In both cases, the predicted steady-state temperature – represented by the black line – lies between the upper and lower temperature extremes. In both ambient atmosphere and vacuum conditions, the temperature gradient – measured as the difference in temperature between T2 and T5 – across the chip increases with increasing flow rates. As was the case with hydrogen combustion, the increase in flow rates results in an increase in gas available for combustion, leading to an increase in temperature. The increase in temperature leads to an increase in reaction rate and gas diffusion. Using the kinetic parameters in Section 7.6, the propane combustion reaction rate increases many orders of magnitude from 8.6×10^{-14} moles cm^{-3} s^{-1} at 25 °C to 9.3×10^{-3} moles cm^{-3} s^{-1} at 800 °C In the case of propane in air, the diffusion coefficient increases an order of magnitude from 0.1 cm^2 s^{-1} to 1.04 cm^2 s^{-1} as temperature is increased from 25 °C to 725 °C. In addition, the temperature gradients are larger under vacuum than they are in ambient, again, due to the increase in temperature associated with operating under vacuum.

6.4   Butane Combustion

Steady-state, autothermal butane combustion was achieved for a wide variety of butane flow rates. Similar to the propane experiments, hydrogen was fed along with butane to achieve initial light-off of the reactor. The amount of hydrogen required to initiate steady-state butane combustion in SµRE IV was ~8 sccm, significantly lower than the amount needed to ignite propane combustion.

Again, a concentrated hot spot is seen in the half of the reactor where the reactants are injected for all of the flow rates tested. Homogeneous combustion of butane was never seen, and – once steady-state combustion was achieved – the reaction was quite stable. 100% conversion of butane was achieved at all flow rates tested. At high flow rates, the hot spot became more pronounced. As seen with hydrogen and propane combustion, reactors loaded with 2.5 mg of 1wt% Pt on Al_2O_3 exhibited a temperature profile similar to that seen for 5wt% Pt on Al_2O_3. Autothermal combustion of butane over 1wt% Pt on Al_2O_3 is shown in Figure 6-8.
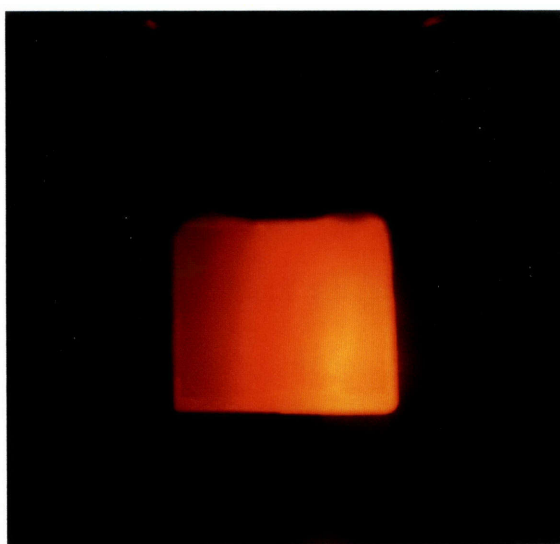
Figure 6-8. Autothermal, steady-state combustion of 9.5 sccm butane over 2.5 mg of 1wt% Pt on Al_2O_3.

6.5   Reactor Failure

Reactor failure was common during the testing of SµRE IV. Failure occurred in a variety of ways. One common failure mode was deactivation of the catalyst, especially after long runs at high temperatures. Deactivation can occur in several ways. Hydrocarbon combustion for long periods of time can lead to coking of the catalyst. Detection of coking in SµRE IV was difficult, and no evidence of coking could be seen in any of the deactivated reactors.

Another pathway to catalyst deactivation involves sintering and agglomeration of the catalyst. Metal agglomeration due to sintering has been reported in systems using platinum on γ-Al_2O_3 catalysts [67-73]. Susu et al reported decreases of 78% and 43% in the amount of hydrogen uptake after reduction for 0.3% Pt/Al_2O_3 and 0.6% Pt/Al_2O_3, respectively, sintered at 800 °C. In this study, decreases in catalytic surface site density began at temperatures of 550 °C [74]. The supported platinum catalyst in SµRE IV reaches temperatures of 690 °C during the brazing step and has reached temperatures in excess of 900 °C during combustion.

Another common form of reactor failure occurred when the reactor channel was plugged. The reactor channel can plug when water condenses in the exhaust stream, causing a buildup of pressure in the reactor. Once water has condensed in the exhaust, the reactor must be externally heated to evaporate the water. In cases where water has deposited within the reactor channel, elimination of water buildup was often not possible. Another cause of reactor plugging results from excess catalyst in the channel. Excess catalyst can result either from overloading the reactor prior to brazing or from delamination of the catalyst once the reaction has started.

Reactor failure also results when high temperatures lead to homogenous combustion at the reactor inlet. Homogeneous combustion was only seen when hydrogen was used as the fuel source. Once the hydrogen has ignited in the reactor channel, the flame propagates to the inlet of

the reactor. The high flame temperature causes softening of the glass capillary, and the back pressure causes tube swelling. Eventually, the tube fractures, and the reactor fails. Figure 6-9 shows a SµRE IV reactor that failed due to homogeneous combustion of hydrogen at the reactor inlet.
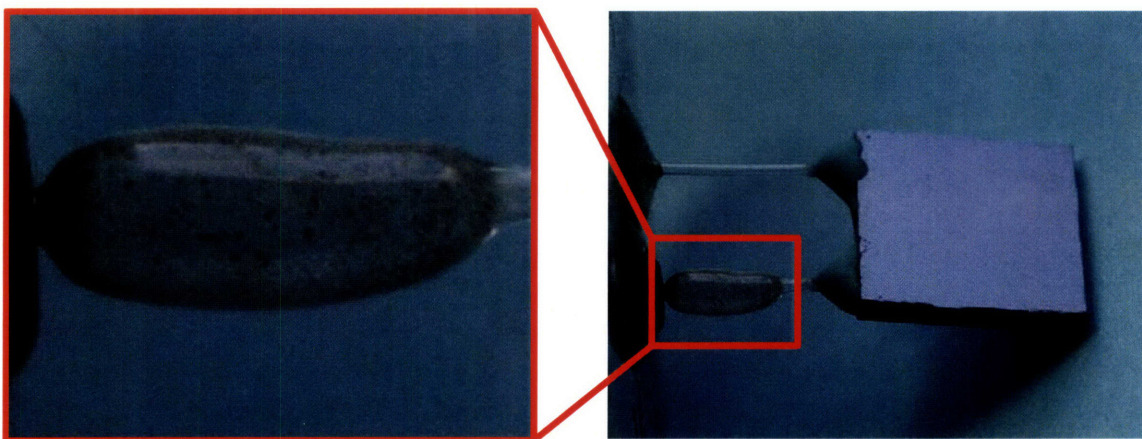
Figure 6-9. SµRE IV reactor after failure via homogeneous combustion of hydrogen. Note that the inlet tube has expanded significantly due to the high temperatures of the reaction flame.

If the inlet of SµRE IV is quickly heated beyond 700 °C, delamination of the glass sealant at the inlet can occur. Delamination occurs due to the slight mismatch in thermal expansion coefficients of the glass sealant $(3.0 \times 10^{-6} \, °C^{-1})$ and the silicon reaction zone $(2.8 \times 10^{-6} \, °C^{-1})$. When a large step increase in fuel is applied, the reactor heats quickly. The inlet gases continue to cool the glass sealant, forming a large thermal gradient across the interface. This gradient is enhanced by the low thermal conductivity of the sealant itself. Figure 6-10 shows a SµRE IV reactor that failed due to rapid heating and delamination of the sealant glass from the silicon reactor. Note that the failure resulted in a clean break along the interface where the sealant met the silicon reactor, suggesting that the fracture was caused by a thermal expansion mismatch.
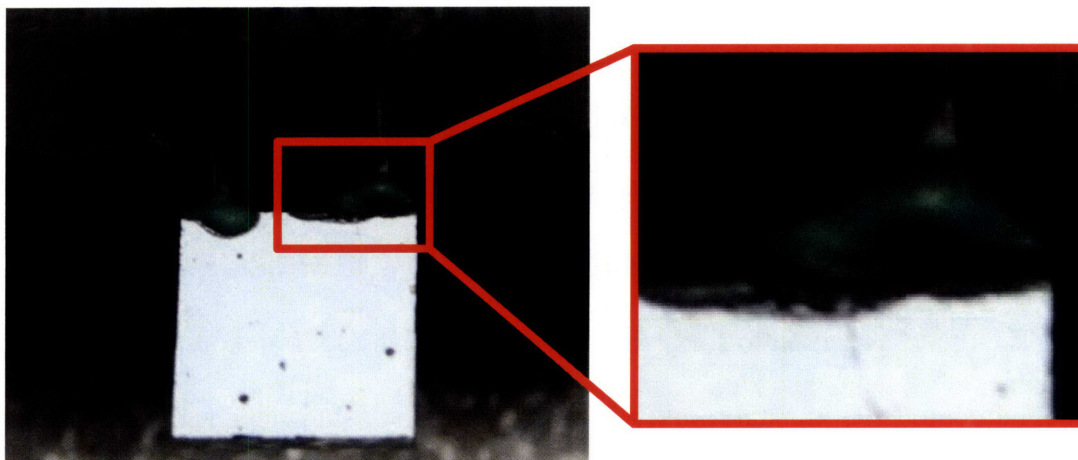
Figure 6-10. SμRE IV reactor after failure via delamination of the glass sealant from the reaction zone. Note that the failure resulted in a clean break along the interface where the braze met the silicon reactor.

When the outlet of the silicon reaction zone reaches high temperatures, the exhaust gases can cause failure of the epoxy joining the exhaust capillary to the testing chuck. Prior to failure the epoxy will change colors from clear, to yellow, to dark brown. Once the exhaust epoxy has failed, the reactor can continue operation in ambient, but vacuum cannot be maintained. Epoxy can be re-applied to fix the seal. However, re-application can only be done a limited number of times before the distance between the epoxy and the reactor is too short to allow for stable testing. Figure 6-11 shows a SμRE IV reactor in which the exhaust epoxy failed.
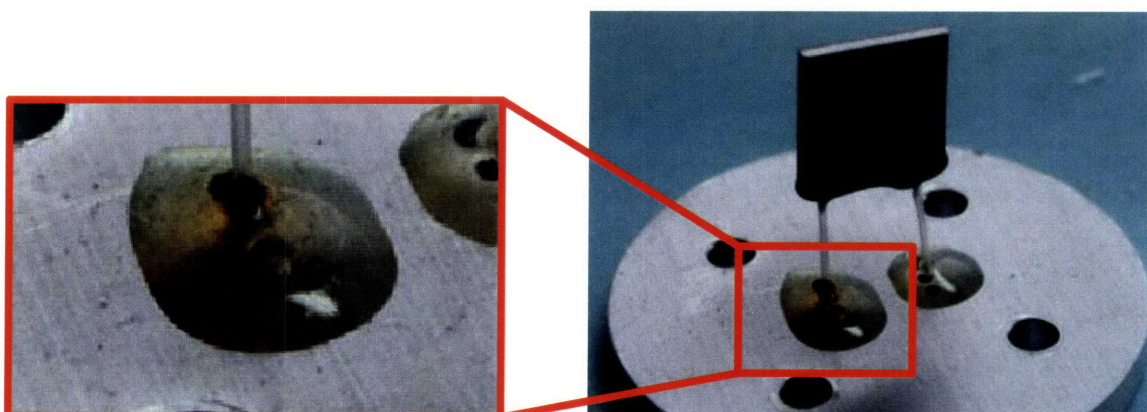
Figure 6-11. SμRE IV reactor after failure via burning of the epoxy joining the outlet capillary to the aluminum testing fixture.

Chapter 7   Theoretical Modeling

A computational fluid dynamics (CFD) model of steady-state combustion in SμRE IV was developed using CFD-ACE multiphysics software. The three-dimensional, finite-volume model allowed for the simultaneous solution of the fluid flow, heat transfer, and chemical reaction. The model was used to study the combustion of hydrogen and propane. By comparing the model output to experimental results, the reaction kinetic parameters were determined for the system.

7.1   Reactor Geometry

The reactor geometry used in the model is depicted in Figure 7-1. A plane of symmetry – indicated by the red line in Figure 7-1 – is drawn through the middle of the reactor, splitting the channel along its length. The channel pattern matches the design shown in Figure 4-9, with the exception of the omitted convex corner undercuts at the channel turns, the inlet, and the outlet. While the glass sealant has been included at the inlet and outlet, the capillary tubes have not been included to aid in the generation of the solution grid. The first pass of the reactor channel has been drawn using three volumes. This allows for the modeling of reactors with varying entry lengths before active catalyst is encountered. Ignition of the reaction can be modeled to start at Point 1, Point 2, or Point 3 on Figure 7-1.
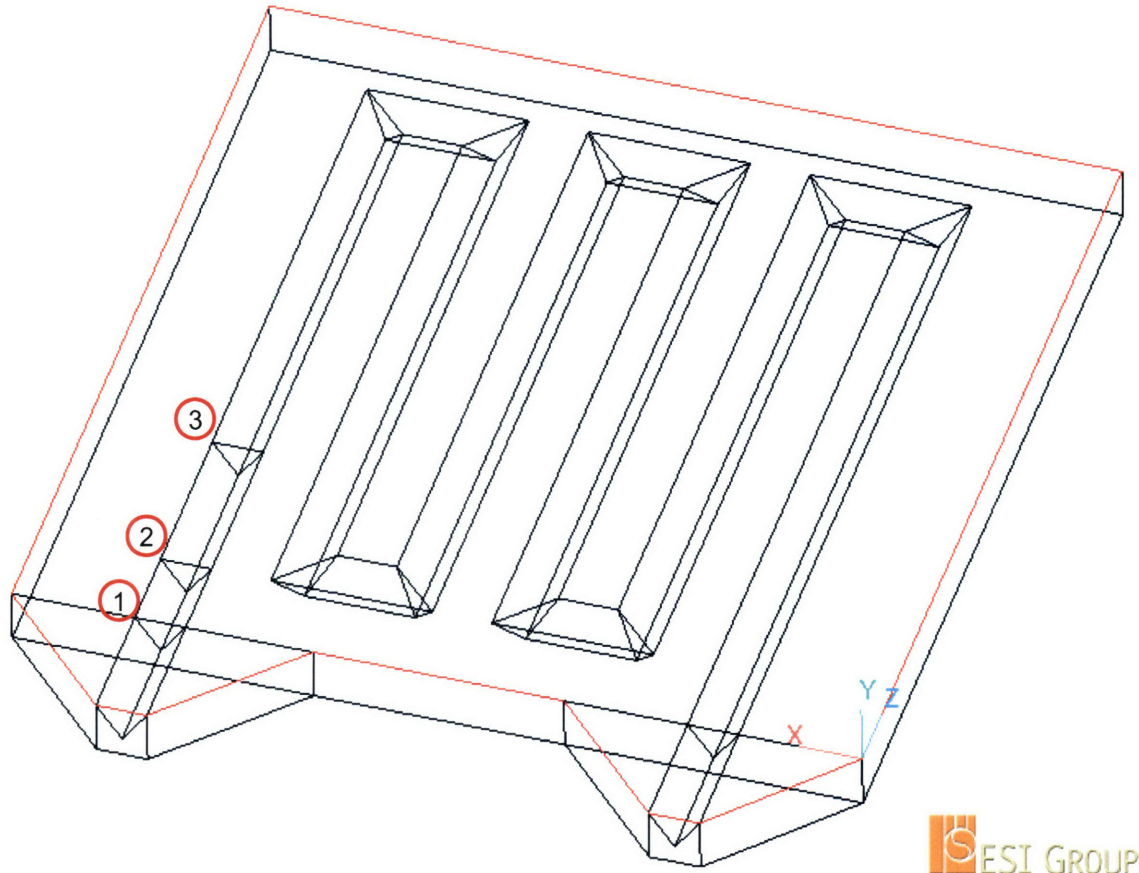
Figure 7-1. Reactor geometry

7.2   Governing Equations

The finite volume model developed using CFD-ACE solved for the flow field, thermal profile, and individual species concentrations simultaneously. This multiphysics problem is non-trivial because the temperature dependence of each equation renders the system highly coupled. In this appendix, the governing equations used to describe the system are outlined, and the resultant flow profile in the system is analyzed.

Mass conservation is expressed in the form of the continuity equation:

$$\rho = \nabla \cdot (\rho v) \tag{7-1}$$

In Equation 7-1, ρ is the mass density of the gas mixture and v is the vector of the mass-averaged velocity. The density of the gas being analyzed in this system can change due to two factors. First, as the reaction proceeds, the number of moles changes due to the consumption of the reactants. The net changes in the number of moles for the reactions considered in this thesis are outlined in Table 6-1. In addition, as the system changes temperature, the gas expands or contracts. For the combustion reactions studied using the CFD-ACE model, these two effects are coupled due to their exothermic nature.

In order to account for variations in the density of the gas, the ideal gas law can be used. Use of the ideal gas law is appropriate because the operating pressure of the system is much less than the critical pressure. In addition, the Mach number for this system is much less than 1. For a multi-component gas, the ideal gas law yields the following expression for density:

$$\rho = \frac{P_o \sum x_i MW_i}{RT} \tag{7-2}$$

In Equation 7-2, P_o is the operating pressure of the reactor, x_i is the mole fraction of species i, MW_i is the molecular weight of species i, R is the gas constant, and T is the temperature of the gas. Because

The conservation of momentum is described using the Cauchy Momentum Equation:

$$\rho v \bullet \nabla v + \nabla P + [\nabla \bullet \tau] - \rho g = 0 \tag{7-3}$$

In order to solve the 3-D model, Equation 7-3 must be expanded to three dimensions. Solution of Equation 7-3 yields velocity components in each of the three dimensions.

In addition to mass and momentum, energy must also be conserved in the system. The energy balance can be expressed as:

$$\rho C_p v \bullet \nabla T - \nabla \bullet \lambda \nabla T + \sum_{i=1}^{n} \rho y_i C_{p,i} V_i \bullet \nabla T + \sum_{i=1}^{n} w_i H_i = 0 \qquad (7\text{-}4)$$

In Equation 7-4, C_p is the constant pressure specific heat, λ is the thermal conductivity of the gas mixture, n is the number of gas phase species, y_i is the weight fraction of species i, V_i is the diffusion velocity of species i, w_i is the molar production rate of species i per unit volume, and H_i is the molar enthalpy of species i. The diffusion velocity of species i can be expressed as:

$$V_i = -D_{im} \frac{1}{x_i} \nabla x_i - \frac{D_i^T}{\rho y_i} \frac{1}{T} \nabla T \qquad (7\text{-}5)$$

In Equation 7-5, D_{im} is the mixture diffusion coefficient, and D^T is the thermal diffusion coefficient. Thermal diffusion is generally a significant contributor to molecule motion when large thermal gradients and low molecular weight species are encountered. While the thermal gradients observed in SµRE IV are mild for the flow rates tested, the contribution of thermal diffusion has been included in all simulations.

Finally, mass must be conserved in the system. This is expressed as:

$$\rho v \bullet \nabla y_i + \nabla \bullet (\rho y_i V_i) - w_i M_{w,i} = 0 \qquad (7\text{-}6)$$

If there are n number of species present in the system, $n-1$ equations in the form of Equation 7-6 must be included. The final species can be solved for as:

$$y_n = 1 - \sum_{i=1}^{n-1} y_i \qquad (7\text{-}7)$$

7.3   Model Assumptions

Many assumptions had to be made in order to produce a workable model. For example, it was assumed that the gas phase behaves as a continuum. This is a reasonable assumption given the fact that the mean free path is much smaller than the distance over which the gas properties change. In addition, it was assumed that the gases obeyed the ideal gas law. Given the types of gases involved in the reactions and the operating pressure of 1 atm, this is also a reasonable assumption.

It was also assumed that the flow of gases in the reactor is always laminar. Given the small length scales of SμRE IV, laminar flow dominates over a wide range of flow rates. In fact, The Reynolds number ranged from 1–1000 for the flow rates studied. This range is significantly lower than the value corresponding to the onset of turbulence for pipe flow (Re ~ 2300).

The gravitational effects in the system were assumed to be negligible. This assumption is reasonable due to the small diameter of the enclosed channel. In addition, the gases in the reactor are low in density.

Regarding the channel geometry, the thickness of the catalyst layer has been assumed to be infinitely small. In practice, the catalyst layer occupies some finite volume, thus reducing the exposed surface area and residence time. In addition, it is assumed that the elimination of the convex corner undercuts from the model geometry has a negligible effect on the final solution.

Finally, several assumptions were made regarding the chemical reaction. First, it was assumed that the chemical reactions followed simple, 1-step reaction mechanisms. In addition, the reaction rate was assumed to follow Arrhenius-type behavior. Finally, because it was assumed that the catalyst layer was infinitely small, the diffusion of the reactants through the

pores of the catalyst was ignored in this analysis. Instead, the reaction progressed once the reactants reached the channel wall. In reality, the thickness of the deposited catalyst layer was ~50 μm.

7.4   Solution Grid

The solution grid used to model hydrogen combustion is shown in Figure 7-2. Due to the irregular shape of the channels, an "unstructured grid" using tetrahedral cells was employed. The density of the cells was doubled until the final solution of consecutive models converged to within 1 °C. Construction of the solution grid requires *a priori* knowledge of how the reactor behaves in practice. The concentration and flow gradients were confined to the interior of the channels. For this reason, the grid was made denser within the channel volumes. The velocity profile was more difficult to model at the channel turns. Therefore, more grid volumes were placed at the channel corners. Based on preliminary experimental data, hydrogen combustion produced a concentrated hot spot at the first third of the first pass through the reactor, requiring a denser mesh at this point as well. Finally, the glass sealant was expected to tolerate large thermal gradients, requiring a dense mesh there as well.
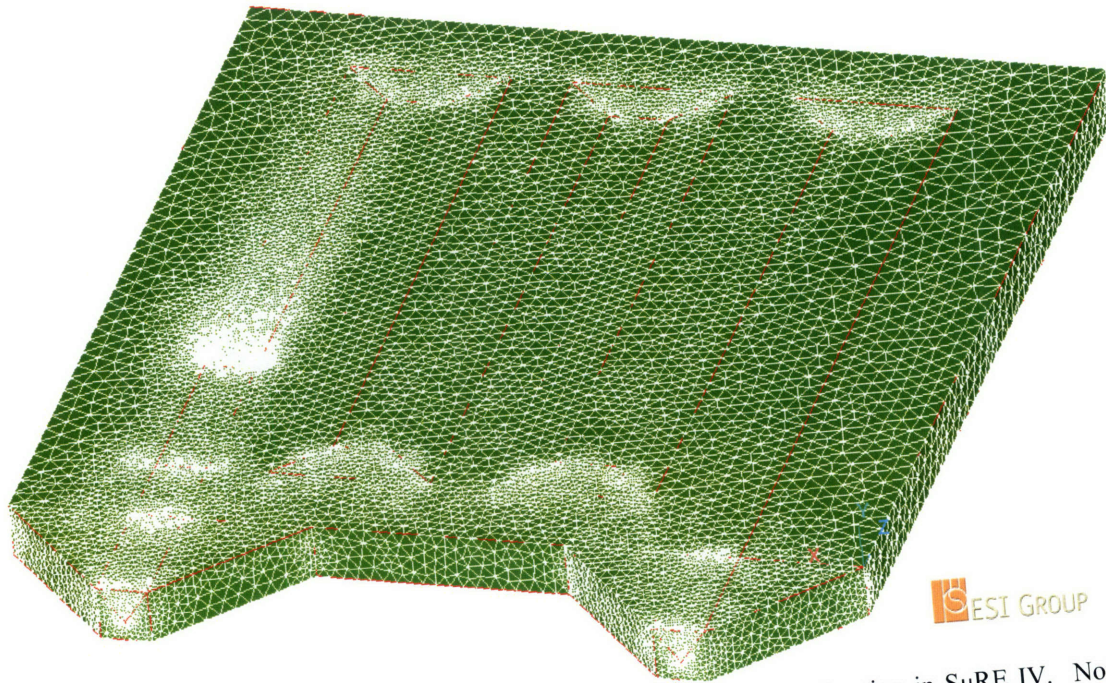
Figure 7-2. Volume element mesh used to simulate catalytic hydrogen combustion in SµRE IV. Note that the concentration of the mesh in the reactor channels, in the glass sealant, at the ignition points, and at the inlet and outlet.

7.5 Volume Conditions

The physical properties of the materials included in the simulation are specified in the "Volume Conditions" tab of the CFD-ACE simulation. In this section, the calculation methods are outlined for the gaseous and solid phases.

7.5.1 Gases

7.5.1.1 Density

The fluid density was modeled using the ideal gas law, as previously discussed. CFD-ACE calculates the density of the gas as:

$$\rho = \frac{P_o \sum x_i MW_i}{RT}$$

(7-8)

7.5.1.2 Viscosity

To calculate the viscosity of the gas mixture, the "Mix Kinetic Theory" option is employed. "Mix Kinetic Theory" uses the Chapman-Enskog theory to determine viscosity. The viscosity of each component in the gas is calculated as:

$$\mu_i = 2.6693 \times 10^{-5} \frac{\sqrt{MW_i T}}{\sigma_i^2 \Omega_\mu} \tag{7-9}$$

In Equation 7-9, MW_i is the molecular weight of species i, σ_i is the characteristic diameter of the molecule/atom in Angstroms, and Ω_μ is the collision integral given by:

$$\Omega_\mu = \frac{1.16145}{T*^{0.14874}} + \frac{0.52487}{e^{0.77320T*}} + \frac{2.16178}{e^{2.43787T*}} \tag{7-10}$$

where $T*$ is the dimensionless temperature given by:

$$T* = \frac{\kappa T}{\varepsilon} \tag{7-11}$$

In Equation 7-11, ε is the characteristic energy (Lennard-Jones parameter) and κ is Boltzmann's constant. To calculate the viscosity of the gas mixture using kinetic theory, the following formula is used:

$$\mu_{mix} = \sum_{i=1}^{N} \frac{x_i \mu_i}{\sum_j x_j \Phi_{ij}} \tag{7-12}$$

In Equation 7-12, x_i and x_j are the mass fraction of species i and species j, μ_i is the viscosity of species i, and Φ_{ij} is a dimensionless quantity defined as:

$$\Phi_{ij} = \frac{1}{\sqrt{8}} \left(1 + \frac{MW_i}{MW_j} \right)^{-1/2} \left[1 + \left(\frac{\mu_i}{\mu_j} \right)^{1/2} \left(\frac{MW_j}{MW_i} \right) \right]^2 \tag{7-13}$$

7.5.1.3 Thermal Conductivity

The thermal conductivity of the gas is also calculated using the "Mix Kinetic Theory" option. The equations employed are similar to those in Section 7.5.1.2.

7.5.1.4 Specific Heat

The specific heat of the gas mixture is calculated using the "Mix JANNAF" method. The Mix JANNAF method uses curve fits from experimental data. The specific heat and enthalpy are calculated as:

$$\frac{C_p}{R} = a_1 + a_2 T + a_3 T^2 + a_4 T^3 + a_5 T^4 \tag{7-14}$$

$$\frac{H}{RT} = a_1 + \frac{a_2 T}{2} + \frac{a_3 T^2}{3} + \frac{a_4 T^3}{4} + \frac{a_5 T^4}{5} + \frac{a_6}{T} \tag{7-15}$$

The coefficients in Equations 7-14 and 7-15 are obtained from experimental data and must be specified for each of the components in the gas mixture.

7.5.1.5 Diffusion

The "Multi-component Diffusion" option in CFD-ACE was used to model species diffusion in the gas mixture. In this model, the diffusive flux of the gas species is split into two parts, concentration gradient-driven diffusion and thermal diffusion:

$$j_i = j_i^C + j_i^T \tag{7-16}$$

The concentration gradient-driven diffusion of the gas species is calculated as:

$$j_i^C = -\rho D_i \nabla y_i \tag{7-17}$$

In Equation 7-17, y_i is the mass fraction of species i, and D_i is the concentration-driven diffusion coefficient calculated as:

$$D_i = \frac{1 - x_i}{\left[\sum_{j=1}^{n} \frac{x_j}{D_{ij}} \right]_{j \neq i}}$$

(7-18)

D_{ij} is calculated using the Chapman-Enskog formulas.

The second part of the calculation of the overall diffusive flux represents the thermal diffusive flux and is calculated as:

$$j_i^T = -\rho D_i^T \nabla (\ln T)$$

(7-19)

In Equation 7-19, the thermal diffusion coefficient is calculated as:

$$D_i^T = \left[\sum_{j=1}^{n} \frac{M_i M_j}{M^2} k_{ij} D_{ij} \right]_{j \neq i}$$

(7-20)

where k_{ij} is the thermal diffusion ratio.

Species conservation was ensured by selecting the "Stefan Maxwell" option, which makes use of a modified form of the Stefan-Maxwell equation.

7.5.2 Solids

Volume conditions also must be specified for the solids in the system. Given that the solids are pure materials, the volume conditions specifications are more straightforward. Specific heat, thermal conductivity, and density of silicon and the sealant (modeled as glass) were specified as piecewise continuous functions of temperature.

7.6   Boundary Conditions

Heat transfer boundary conditions were specified at every external wall. For vacuum simulations, only radiation was considered as a heat loss pathway. The emissivity of the silicon and the glass sealant were modeled as 0.65 and 0.95, respectively. For ambient atmosphere simulations, convective heat transfer was added at each of the walls.

The inlet flowrate was specified as an average volumetric flowrate of the gas mixture. The outlet pressure was specified as 1 atm. No-slip conditions were imposed at the channel walls.

The chemical reaction was modeled as a surface reaction at the channel walls. The catalyst layer was assumed to be infinitely thin, and thus, diffusion through the catalyst layer was not considered in the model.

The chemical reaction was modeled using an Arrhenius expression to model the reaction rate constant:

$$k = Ae^{E_a/RT} \qquad (7\text{-}21)$$

In Equation 7-21, A is a pre-exponential constant and E_a is the activation energy.

Hydrogen combustion was modeled using a one-step mechanism proposed by Schefer [62]. Schefer's mechanism includes a first-order rate dependence on hydrogen concentration and a zero-order dependence on oxygen concentration. The reported activation energy for this model is 14.9 kJ mol^{-1}. Given this information, the rate expression can be written as:

$$Rate = A[H_2]e^{1792K/T} \qquad (7\text{-}22)$$

For propane combustion, a one-step mechanism was also employed. The order of the reaction was assumed to be 1.1 with respect to propane concentration and -0.5 with respect to oxygen, similar to the values reported in Ma et al [75] and Burch et al [76] in which explicit reaction orders were specified for oxygen. It has been reported that excess oxygen can lead to inhibition of the reaction and complicate the first-order dependence on propane concentration [77]. This phenomenon was not included in the CFD-ACE model. Activation energies ranging from 73.7 kJ mol^{-1} to 104.7 kJ mol^{-1} were found in the literature [72, 75, 77-81]. Wanke studied the oxidation of propane over a spherical commercial catalyst. Wanke's activation energy of 89.1 kJ mol^{-1} was used in the simulations as it lies in the middle of the reported range [81].

7.7 Results

7.7.1 Velocity Profile

The equations described in Section 7.2 are solved simultaneously using CFD-ACE. To check the accuracy of the solution, heat, mass, and species balances must be performed over the system. Of particular interest in this appendix is the flow profile of the reactor.
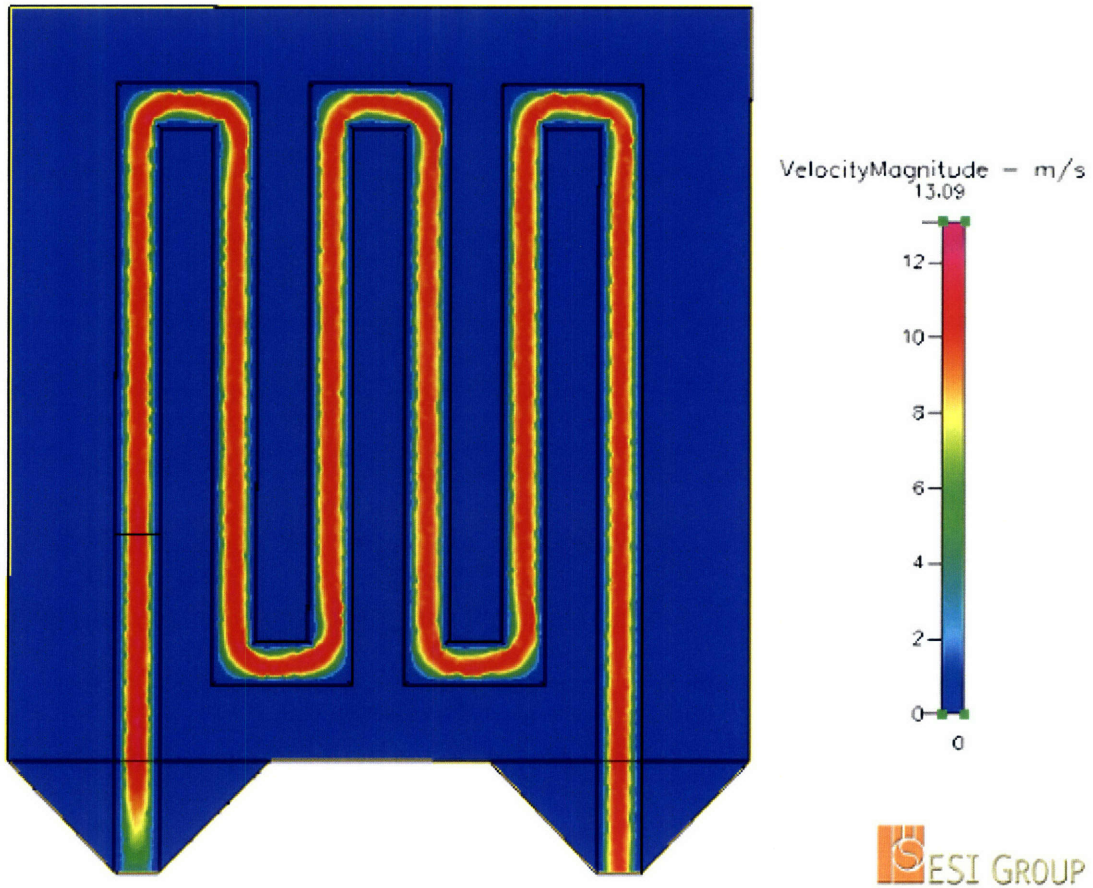
Figure 7-3. Velocity profile in SμRE IV for the combustion of 26.5 sccm hydrogen in 26.5 sccm oxygen.

The average temperature at the point of full conversion in Figure 7-3 was ~875 K, 3.2 times greater than the ambient temperature of 298 K. From Table 6-1, δ for 2:1 oxygen:hydrogen combustion is 0.75. Therefore, a 240% increase in the average velocity from the inlet to the point of full conversion is expected.

7.7.2 Hydrogen Combustion

Hydrogen combustion simulations were run for a variety of flow rates. In all simulations, 100% conversion of hydrogen was achieved in the first third of the first channel pass, as illustrated in Figure 7-4 (53 sccm). This is in good agreement with what was observed experimentally.
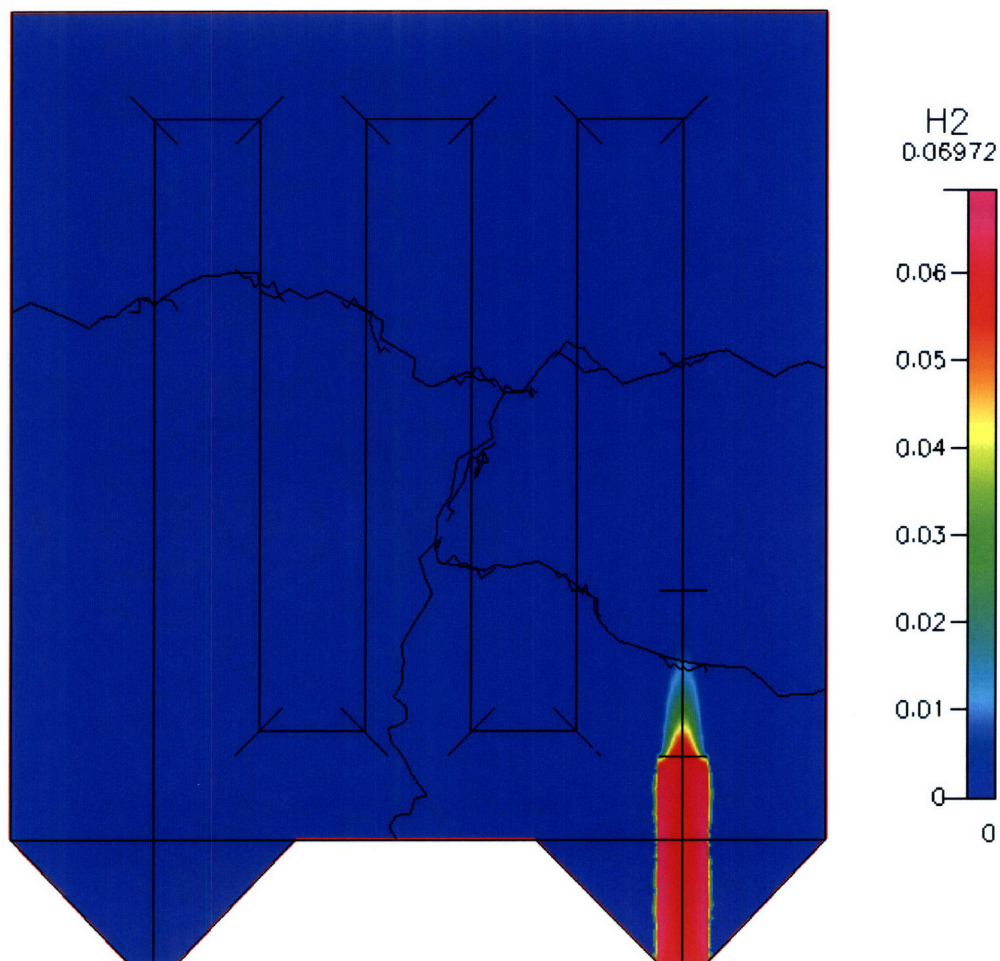
Figure 7-4. Simulated hydrogen concentration as a function of position in SμRE IV. For this simulation, the hydrogen flow rate is set at 53 sccm. A 2:1 stoichiometric ratio of oxygen to hydrogen was supplied to the inlet.

For all hydrogen combustion simulations, a concentrated hot spot was observed at the inlet of the reactor. Figure 7-5a shows the experimental temperature profile for a feed of 53 sccm of hydrogen. The simulated profile in Figure 7-5b can be directly compared. The temperature distributions are consistent with the exception of the temperatures of the hot spots. The large difference in numbers is due to the fact that the hot spot was concentrated to an area less than 1 mm, the resolution limit of the IR thermometer used to measure the reactor temperature.

Figure 7-5. Comparison of (a) experimental temperature profile to (b) simulated temperature profile for the combustion of 53 sccm of hydrogen in 16 mTorr vacuum. A 2:1 stoichiometric ratio of oxygen to hydrogen was supplied to the inlet.

Figure 7-6. Comparison of (a) experimental temperature profile to (b) simulated temperature profile for the combustion of 16 sccm of hydrogen in 16 mTorr vacuum. A 2:1 stoichiometric ratio of oxygen to hydrogen was supplied to the inlet.

Figure 7-6a shows the experimental temperature profile for a feed of 16 sccm of hydrogen. The temperature distributions in Figure 7-6a and Figure 7-6b are in fairly good

agreement. Note that the measured hot spot temperature is closer to the simulation hot spot temperature. This is due to the fact that the temperature gradient at the hot spot is much smaller for the combustion of 16 sccm hydrogen than in the combustion of 53 sccm hydrogen.

7.7.3 Propane Combustion

Propane combustion simulations were also run for a variety of flow rates. 97% conversion of propane was observed at propane flow rates of 6 sccm, and greater than 99% conversion of propane was observed for flow rates of 7 sccm and higher. This observation is in good agreement with experimental observations. Propane concentration profiles for several flow rates are shown in Figure 7-7. As flow rates were increased, full conversion of propane occurred closer to the reactor inlet. Increases in flow rates lead to higher hot spot temperatures at the inlet due to the positive feedback effect discussed in Section 6.3. As the reactor temperature is increased, the reaction rate increases many orders of magnitude, thus causing a further increase in temperature.
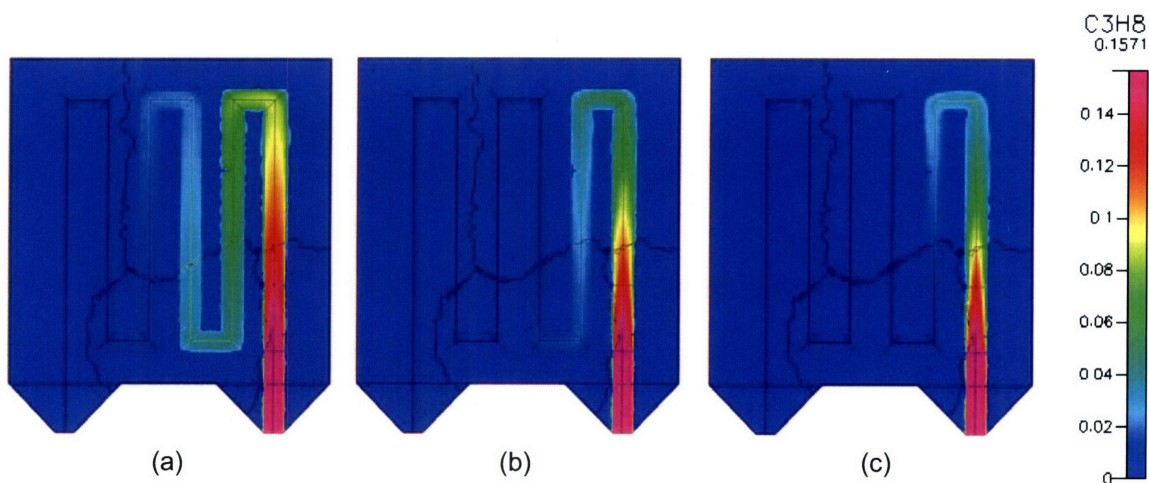
Figure 7-7. Steady-state propane concentration profile for initial propane flow rates of (a) 6 sccm, (b) 8 sccm, and (c) 10 sccm. As the flow rate is increased, more propane reacts closer to the inlet. A 1.5:1 stoichiometric ratio of oxygen to propane was supplied to the inlet.

For all propane combustion simulations, the inlet half of the reactor exhibited a hot spot while the exhaust half was cooler. Again, this was consistent with the experimental observations reported in Section 6.3. Figure 7-8a shows an experimental temperature profile for a feed of 6 sccm of propane. The simulated profile in Figure 7-8b can be directly compared. In this case, the temperature distributions are consistent including the hot spot. This is because the temperature gradient within a 1 mm spot is only 2 °C, compared to 25 °C for the 53 sccm hydrogen simulation.
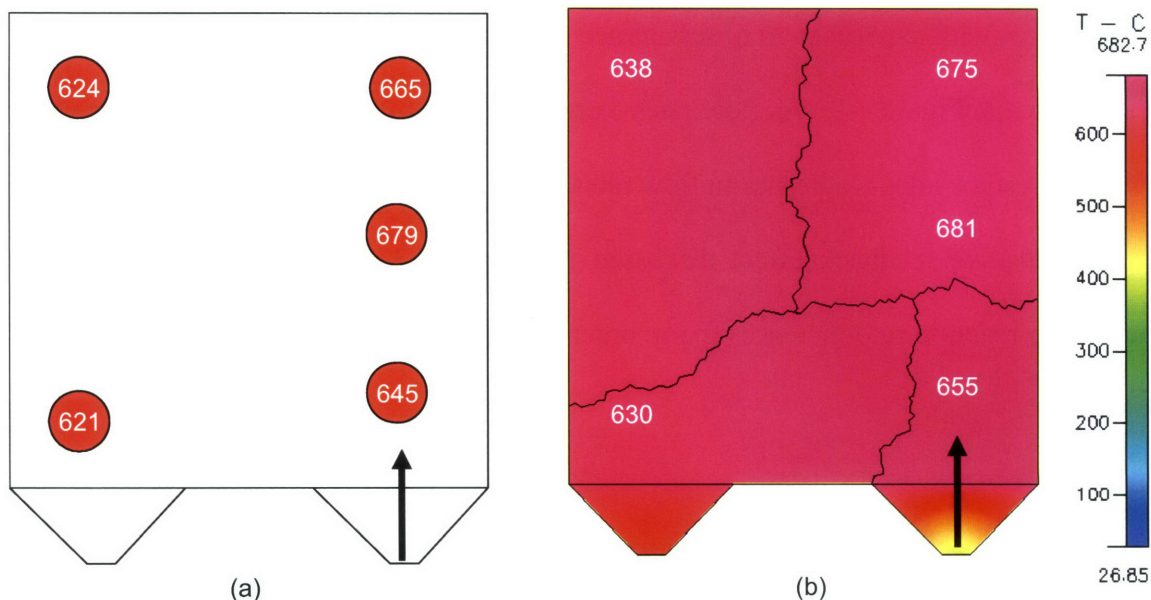
Figure 7-8. Comparison of (a) experimental temperature profile to (b) simulated temperature profile for the combustion of 6 sccm of propane in 16 mTorr vacuum. A 1.5:1 stoichiometric ratio of oxygen to propane was supplied to the inlet.

Figure 7-9a shows the experimental temperature profile for a feed of 10 sccm of propane. The simulated profile in Figure 7-9b can be directly compared. The temperature distributions are in fairly good agreement.
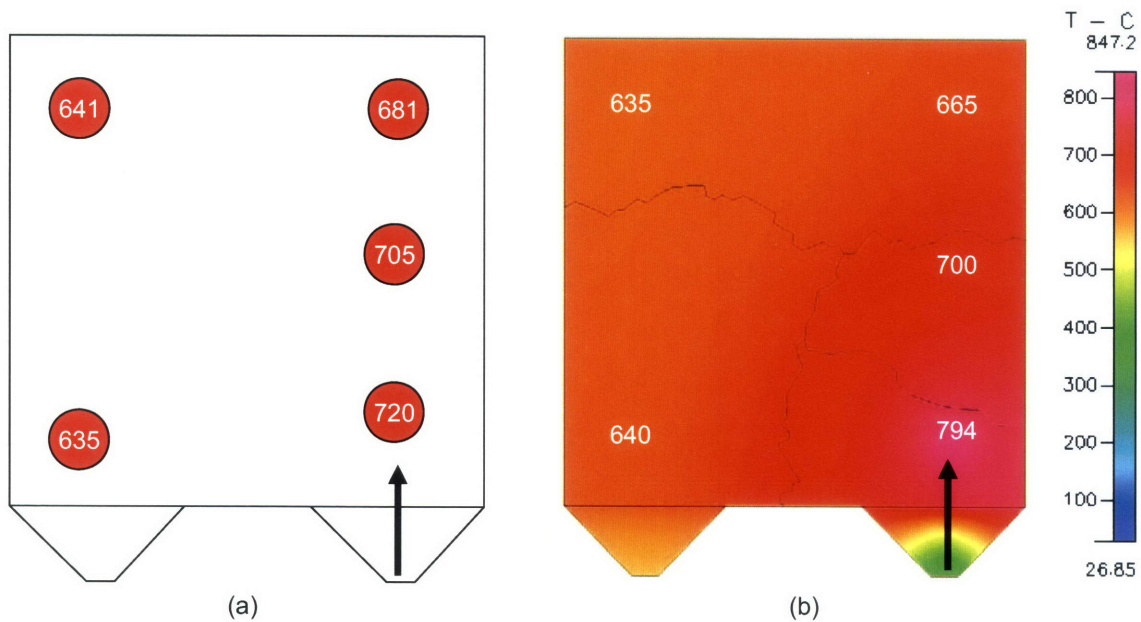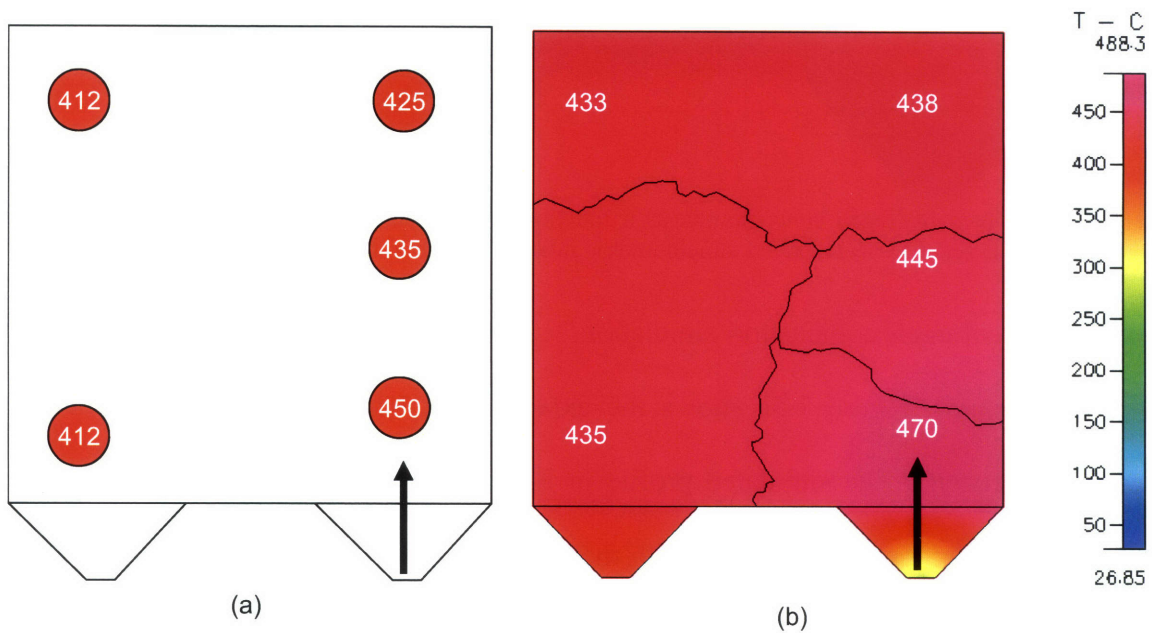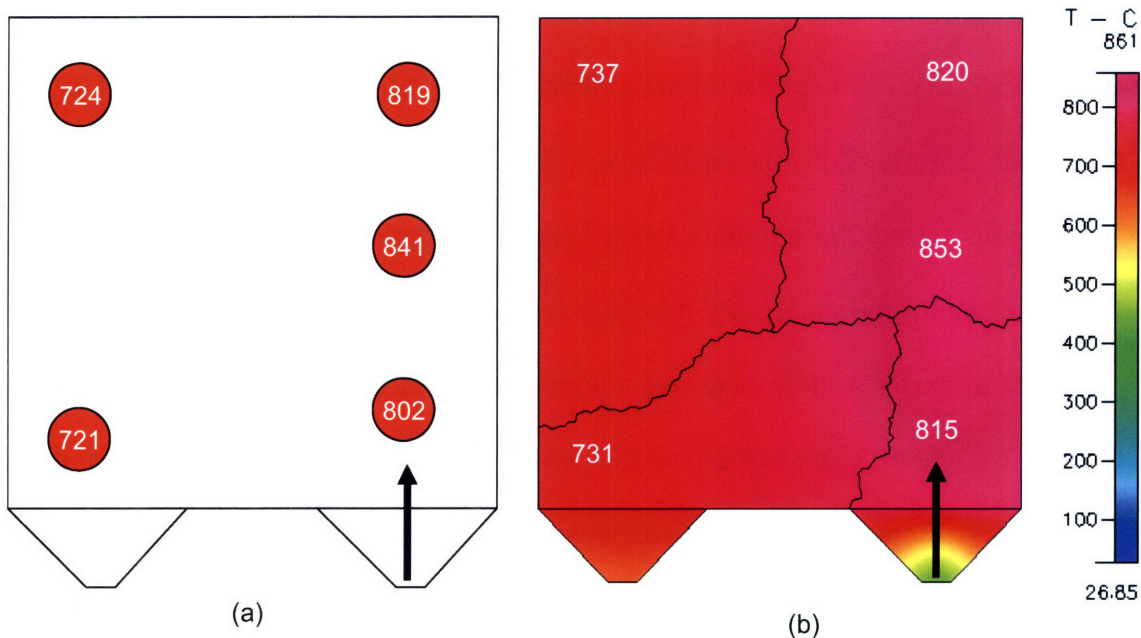
Figure 7-9. Comparison of (a) experimental temperature profile to (b) simulated temperature profile for the combustion of 10 sccm of propane in 16 mTorr vacuum. A 1.5:1 stoichiometric ratio of oxygen to propane was supplied to the inlet.

7.7.4 Discussion

The theoretical temperature distributions agree to within experimental error in all cases. The small differences between the measured temperature distribution and the theoretical temperature distribution may be explained by a number of uncontrolled variables. First, the theoretical model does not account for thermal losses via conduction down the borosilicate tubes, although this contribution to temperature loss is almost certainly minimal. Most importantly, the theoretical model assumes that the glass sealant can be applied reproducibly, and that the final brazed glass does not overlap with the silicon reaction zone. In almost all cases, the final glass sealant shape did not conform to these restrictions. The model also did not account for increased channel surface area due to convex corner undercutting, and it did not account for the thickness of the catalyst layer.

On the experimental side, obtaining accurate temperature measurements proved to be a difficult challenge. To calibrate the infrared thermometer, OMEGALAQ temperature indicating liquid was used. Unfortunately, the emissivity of the OMEGALAQ (0.95) was much higher than that of the silicon. In order to minimize the effect of excess heat loss through the lacquer, it had to be applied in small spots using very thin layers. This was difficult to accomplish. Moreover, it was difficult to perform more than one calibration for each reactor due to the residue left behind after a calibration test was performed. No lacquers for use between 400 °C and 621 °C were suitable for vacuum testing. Therefore, only two hydrogen flow rates could be tested.

Chapter 8   Conclusion

8.1   Principal Accomplishments

There are several contributions from this thesis work to the fields of portable power generation and MEMS. To start, it has been demonstrated that the general design proposed by Arana (SµRE I) can be extended to work at larger reactor volumes using simpler microfabrication techniques. The design of SµRE IV included a forty-fold increase in reactor volume, twenty-fold increase in internal exposed surface area, while incorporating only a twenty-fold increase in external surface area. Moreover, the design allows for the stacking of multiple reactors, producing incremental increases in reactor volume and catalytic surface area with only marginal increases in exposed surface area.

In addition, the process required to produce SµRE IV reactors was inexpensive and less complex compared to the SµRE I process. The SµRE IV design eliminated the need for deep reactive ion etching – which is expensive and time-consuming – by incorporating the use of a potassium hydroxide wet etch. In SµRE IV, pre-fabricated thin-walled capillary tubing replaced CVD-grown silicon nitride tubing, greatly reducing fabrication time and expense. Additionally, the pre-fabricated capillary tubing allows one to load the catalyst directly into the reaction zone, eliminating the need for complex integrated catalyst loading structures. The new design also eliminates the need for unconventional fabrication steps including ultra-thin wafer bonding and spray coating of photoresist. While SµRE I required expensive SOI and ultra-thin silicon wafers, SµRE IV requires two standard double-side polished wafers. Overall, the fabrication of SµRE IV requires 35 hours of processing to produce a finished reactor, compared to 150 hours for SµRE I.

Another contribution from this thesis was the development of a robust glass sealant brazing technique. This technique produced a hermetic glass seal stable up to temperatures of 710°C and pressures up to the yield strength of the capillary tubes. This sealing method is promising for use in a wide variety of applications that require precision heating of a small zone.

Stable autothermal combustion of hydrogen, propane, and butane were all demonstrated at millimeter length scales. Maximum combustion temperatures in excess of 900°C were realized.

Finally, a CFD model of SµRE IV was developed. This model accurately predicted the thermal, chemical, and microfluidic behavior of the system at a variety of flow rates for both hydrogen and propane combustion. This model provided insight into the operation of the reactor that allowed for the incorporation of several design improvements. In addition, the model will be a useful tool as further design improvements are made.

8.2   Limitations of Approach

This thesis work includes several limitations in its approach. Most prominently, the low thermal stability of the glass sealant poses a large problem when trying to develop an isothermal reactor capable of withstanding temperatures of 900°C. While a significant amount of time (~24 months) was devoted to testing glass sealants, additional options should be investigated.

In addition to the glass sealant issue, several additional limitations in the design of SµRE IV have also been discovered. The amount of exposed catalytic surface area and reactor volume are limited by the etching method. Increasing the exposed catalytic surface area allows for increased conversion of slower reactions at higher flow rates. In addition, increasing reactor

volume leads to increases in residence time for a given flow rate, also leading to greater reactant conversion.

In SµRE IV, up to 25% of the heat generated via reaction is lost via the exhaust gases. A fraction of these losses could be recuperated by incorporating heat exchangers between the inlet and outlet streams. Given the modular nature of the reactor fabrication, heat exchanger integration is particularly challenging. The material used for the heat exchanger should be able to structurally withstand the thermal expansion of the tubes and the reactor. In addition, the material used to bond the heat exchangers to the tubes must be thermally well-matched.

Due to the uniformity of the catalyst deposition and concentration, thermal non-uniformities were seen in the reactor in all cases where 100% conversion was achieved. In order to combat this problem, a method for controlled catalyst deposition could be developed, allowing the reaction to proceed at an even pace despite decreasing reactant concentrations.

Finally, the CFD model was only used to describe the steady-state autothermal combustion of hydrogen and propane. This model should be extended to describe the combustion of other fuels, simultaneous combustion and reforming, and the effects of bonding multiple reactors.

8.3   Recommendations for Future Work

As mentioned previously, the glass sealant used in SµRE IV is not capable of withstanding temperatures in excess of ~710°C for extended periods of time. For this reason, alternatives to the SCC-7 sealant should be investigated. Given the minute amount of heat lost via thermal conduction through the inlet and outlet tubes, one should consider increasing the wall thickness of the capillary tubing used in the reactors. This would provide much more structural

stability to the reactor, allowing for the use of materials that are less well-matched from a thermal expansion standpoint.

Several design modifications could be made to produce improved reactor performance. First, the inlet and outlet tubes could be spaced closer together. This would facilitate the exchange of heat between the two streams as well as reduce the amount of mechanical stress imparted to the tubes during the thermal expansion of the reaction zone. Second, the inlet gases should be fed in such a way that their first contact with the catalyst occurs at the center of the reactor. By focusing the reaction at the center of the device, thermal uniformity would be easier to achieve.

Another method for improving thermal non-uniformity would be to selectively deposit or dope the catalyst in such a way as to allow for reaction rate uniformity across the entire stretch of expose catalyst surface area. For example, a sharp pulse of poisoning gas could be fed into the reaction inlet in such a way as to reduce the activity of the catalyst closest to the inlet. In addition, alternative catalyst loading methods should be investigated to combat the problem of uncontrolled catalyst deactivation. Employing a sol-gel deposition technique, for instance, would result in reduced platinum agglomeration and catalyst delamination.

This thesis focused mainly on the autothermal combustion of fuel in a single cell. The insight gained from these experiments should be used to perform an in-depth study of auto-thermal reforming of fuels to hydrogen Reactions such as the partial oxidation and steam reforming of hydrocarbons and alcohols should be studied.

Given the large amount of heat lost as radiation from SµRE IV, its use as a combustor in a TPV system should be investigated. SµRE IV's use in other power generation schemes, including in thermoelectric systems, could also be studied.

Appendix A Arana's Design

The previous design by Arana made use of traditional silicon micromachining to fabricate a monolithic reactor. Via a complex fabrication process, Arana was able to integrate several materials with different heat transfer properties to achieve the necessary thermal isolation. While the process was successful, the fabrication scheme required many hours of fabrication time, was expensive, and was difficult to reproduce on the facilities upgraded equipment. Arana's process and the limitations associated with it are described in detail below.

A.1   Fabrication of SµRE I

A schematic outlining the fabrication process associated with Arana's is shown in Figure A-1. Arana's process makes use of two 100-mm (100) double-side polished (DSP) silicon wafers. One is a silicon on insulator (SOI) wafer of standard thickness (~480 µm), and the other is an ultra-thin wafer of 20-µm thickness. To begin, a mold for the reaction zone channels, the SiN_x tubes, and the release pits is etched into the SOI wafer using DRIE and the buried oxide layer as the etch stop. On the back side, four 20- µm-deep square pits are etched. These pits serve two purposes: to act as the points of contact for external fluidic connections and to serve as a pathway for the SiNx precursor gases to reach the tube and reactor zone molds.

Next, the ultra-thin wafer is bonded to the bottom side of the SOI wafer, sealing the release pits. A 2-µm film of low-stress LPCVD silicon nitride is deposited, coating the exterior of the chip as well as the interior of the tube and reaction zone molds. The nitride on the external surface of the reactor is patterned to expose the silicon above the release pits and protect the silicon to be used as the slab heat exchangers. Next, integrated heaters and temperature sensors are incorporated via the deposition and patterning of Ti/Pt layers. Finally, the reactor is released

by etching the expose silicon in fluorine gas. For an in-depth description of the fabrication process, see [40].

A.2   Arana's Design: Limitations

The fabrication process outlined in this section requires ~150 hours of processing time in the clean room. The time-consuming nature of the fabrication process makes quick implementation of design changes very difficult. Additionally, Arana's fabrication process was not able to be scaled from a 100-mm to a 150-mm wafer process. The DRIE apparatus used to etch the channels in SµRE I is expensive, and DRIE machines are not readily available in commercial fabrication facilities. The process also requires specialized starting materials – including ultra-thin silicon wafers and SOI wafers – that are expensive and sometimes difficult to acquire. Finally, performance testing revealed that the reactor performance would be enhanced if the system could be made larger.

(a) DRIE to define fluidic ports (top), channels and release pits (bottom)

Flip

(b) Bond ultra-thin wafer on bottom side

(c) Deposit 2 μm of LPCVD low-stress nitride on all exposed surfaces

(d) Pattern nitride on top and bottom to define release area

(e) Deposit and pattern Ti/Pt heater and TSR on top side

(f) Release structure in KOH or fluorine gas
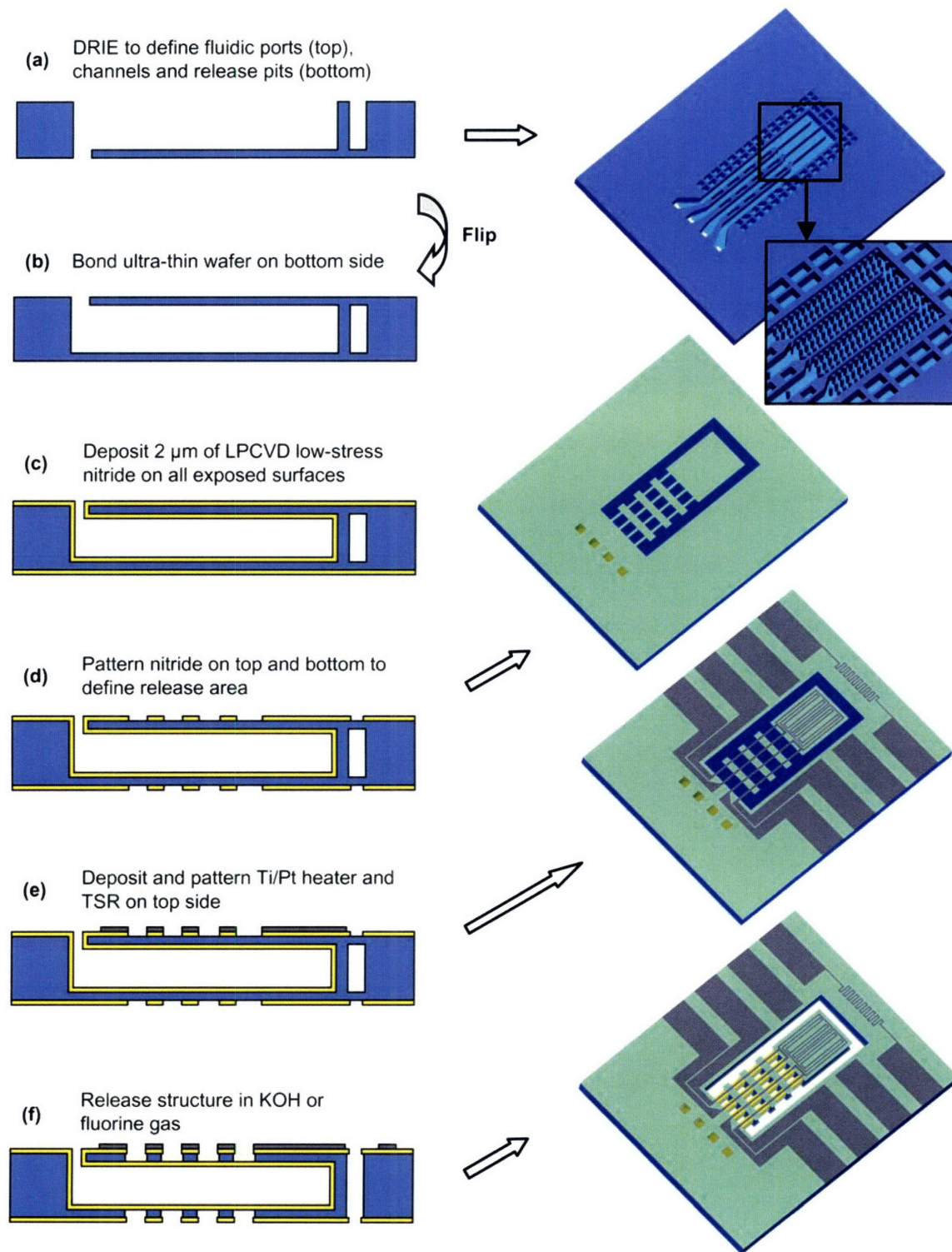
Figure A-1. Schematic of Arana's fabrication process. [1]

Appendix B   SµRE IV Processing Steps

B.1   SµRE IV Fabrication Process

Project Name: **Fuel Processor**

Process Lead: Brandon Blackwell (bblackwe)
Date: 9/13/04

Overview: Begin w/ two silicon wafers. Deposit nitride on both sides of both wafers. Pattern and KOH etch both wafers to define fluidic channels and processor cavities. Oxidize wafers for added chemical resistance. Align and bond wafers to complete the process.

Starting material: 2, 6-in, single-side polished (100) Si wafers (test or better)

STEP	DATE	FAC	wafer #	MACHINE	ACTION	NOTES	CODE
1					**DEPOSIT NITRIDE**		
1.1		ICL	1,2	RCA	RCA clean wafers for CVD		
1.2		ICL	1,2	VTR	Deposit 250nm VTR SiN on both sides of wafers		
2					**PATTERN NITRIDE**		
2.1		TRL	1,2	HDMS	Deposit HDMS		
2.2		TRL	1,2	coater	coat wafer w/ 10um AZ4620 resist		
2.3		TRL	1,2	prebakeoven	prebake 30 min at 90°C		
2.4		TRL	1,2	EV1	Expose ~10 sec.	Use "reactor" mask on both wafers	
2.5		TRL	1,2	postbakeoven	postbake 30 min at 120°C		
2.6		ICL	1,2	LAM490B	Remove exposed nitride using standard nit-etch		
2.7		TRL	1,2	asher	Remove polymer from LAM490B step		
2.8		TRL	1,2	acidhood	Piranha clean wafer to remove resist		
2.9		TRL	2	HMDS	Deposit HDMS		
2.10		TRL	2	coater	coat back side of wafer w/ 10 um AZ4620 resist		
2.11		TRL	2	prebakeoven	prebake 30 min at 90°C		
2.12		TRL	2	EV1	Expose ~10 sec.	Use "reactor_back" mask on back side of wafer 2	
2.13		TRL	2	postbakeoven	postbake 30 min at 120°C		
2.14		ICL	2	LAM490B	Remove exposed nitride using standard nit-etch		
2.15		TRL	2	asher	Remove polymer from LAM490B step		
2.16		TRL	2	acidhood	Piranha clean wafer to remove resist		

3				**KOH ETCH CHANNELS**	
3.1	ICL	1,2	TMAH-KOHhood	25%, 80°C KOH etch wafer	
3.2	TRL	1,2	acidhood	post KOH clean + nitride removal (2 piranhas; 49% HF ~60 min)	
4				**BOND WAFERS**	
4.1	TRL	1,2	RCA-TRL	RCA clean wafers	
4.2	TRL	1,2	EV501	Align wafers for bonding	
4.3	TRL	1,2	tube B3	fusion bond in H2/O2 to grow 500 A SiO2	
4.4	ICL	1,2	bonded diesaw	dice wafers	

Appendix C   Photomasks

Figure C-1. Photolithography mask used to fabricate the first version of SµRE IV reactors with the channel pattern shown in Figure 4-8. This mask is referred to as "reactor" in the fabrication process outlined in Appendix B.

Figure C-2. Close-up view of a single cell in the photolithography mask shown in Figure C-. This mask was used to fabricate the first version of SμRE IV reactors with the channel pattern shown in Figure 4-8. This mask pattern produced nearly perfect convex corners. However, the spacing of the compensation features did not allow for more than 4 passes through the reactor. Additionally, this mask design yielded reactors with no inserts for tubes at the inlet and outlet ports. The resultant channel width is 800μm.
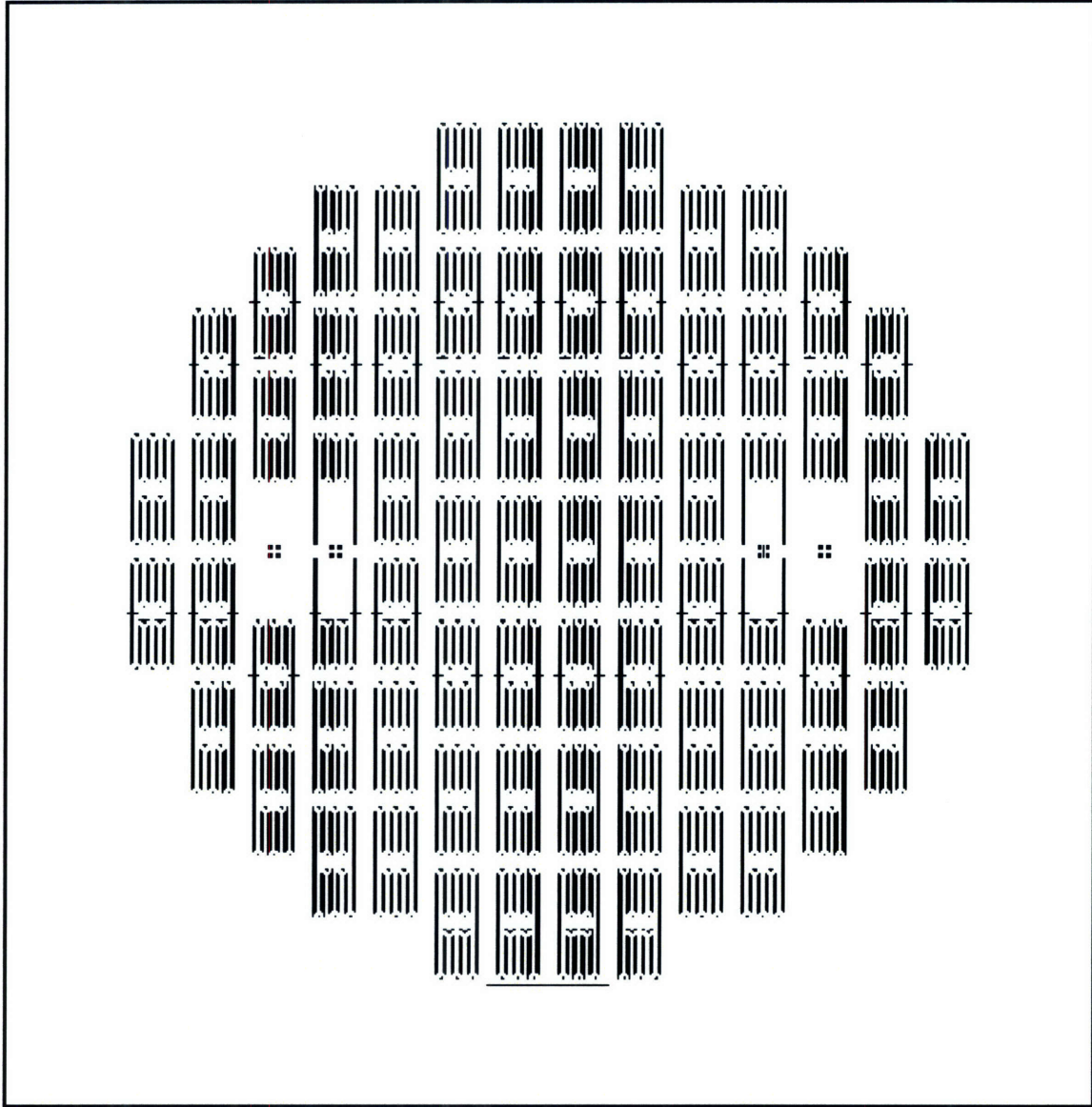
Figure C-3. Photolithography mask used to fabricate the second version of SμRE IV reactors with the channel pattern shown in Figure 4-9. This mask is referred to as "reactor" in the fabrication process outlined in Appendix B.
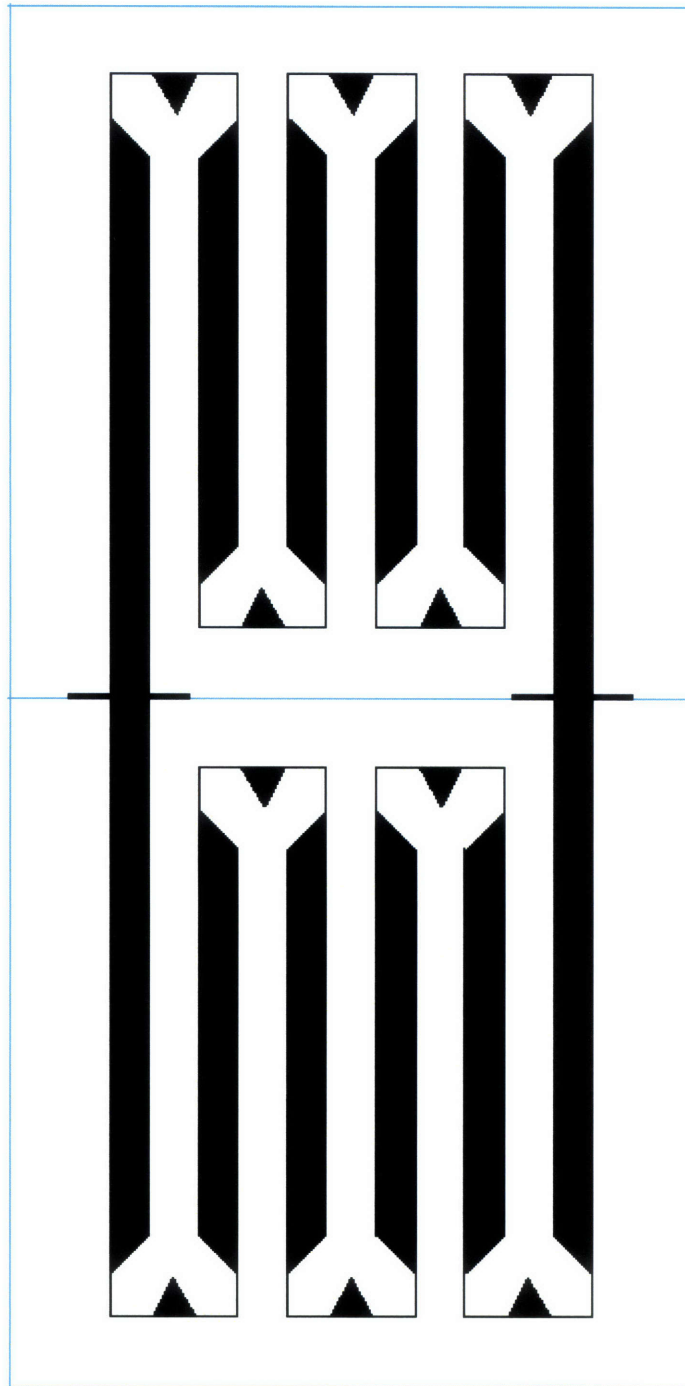
Figure C-4. Close-up view of a single cell in the photolithography mask shown in Figure C-. This mask was used to fabricate the first version of SμRE IV reactors with the channel pattern shown in Figure 4-9. This mask pattern produced convex corners that were slightly undercut due to the close spacing and slight skewing of the corner compensation features. The resultant channel width using this mask is 600μm. Close packing of the channels allows for an additional two passes through the reactor compared to the first version of the channel mask. Additionally, features have been added at the inlet and outlet to produce inserts for tubes at the inlet and outlet ports.
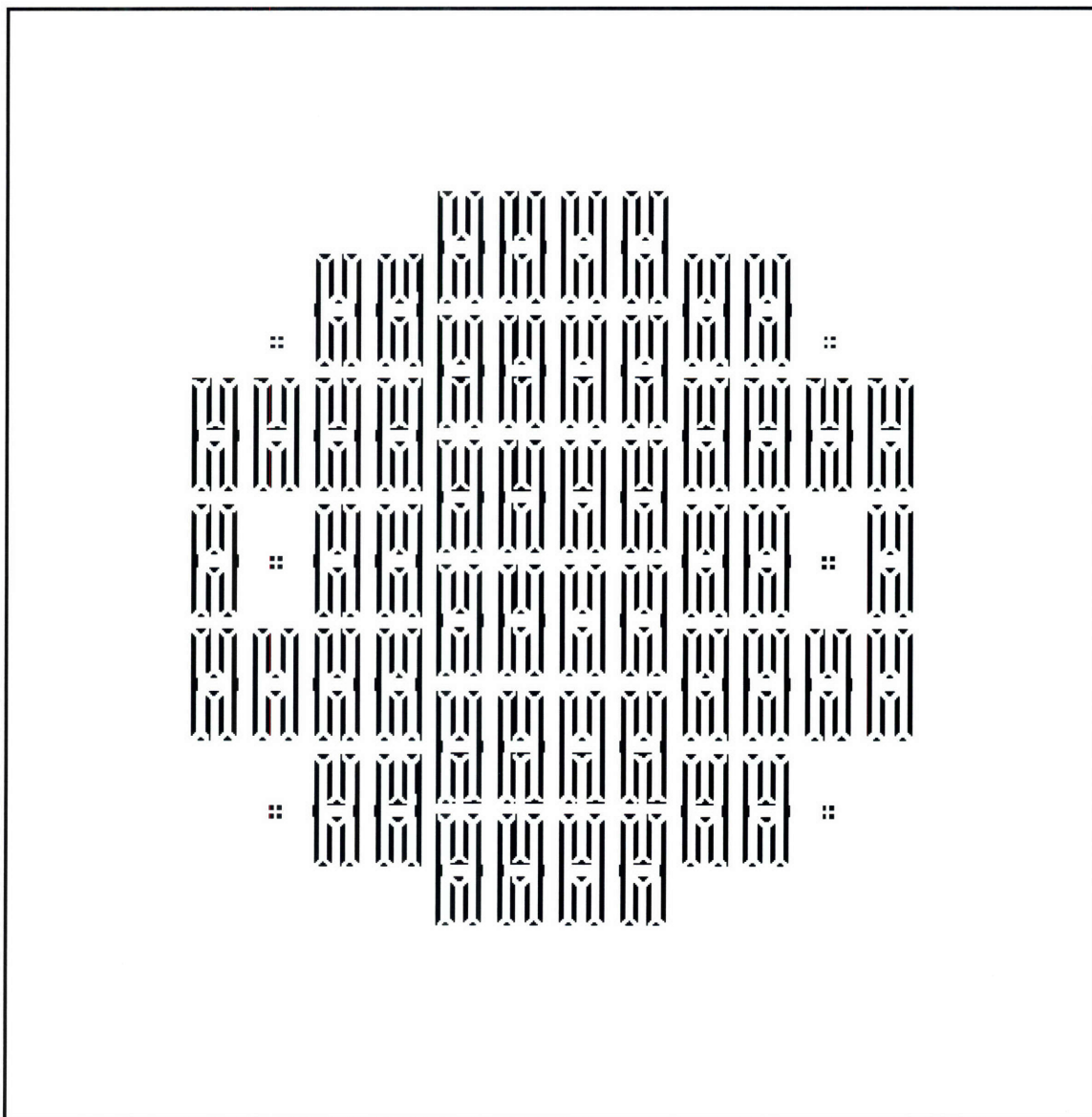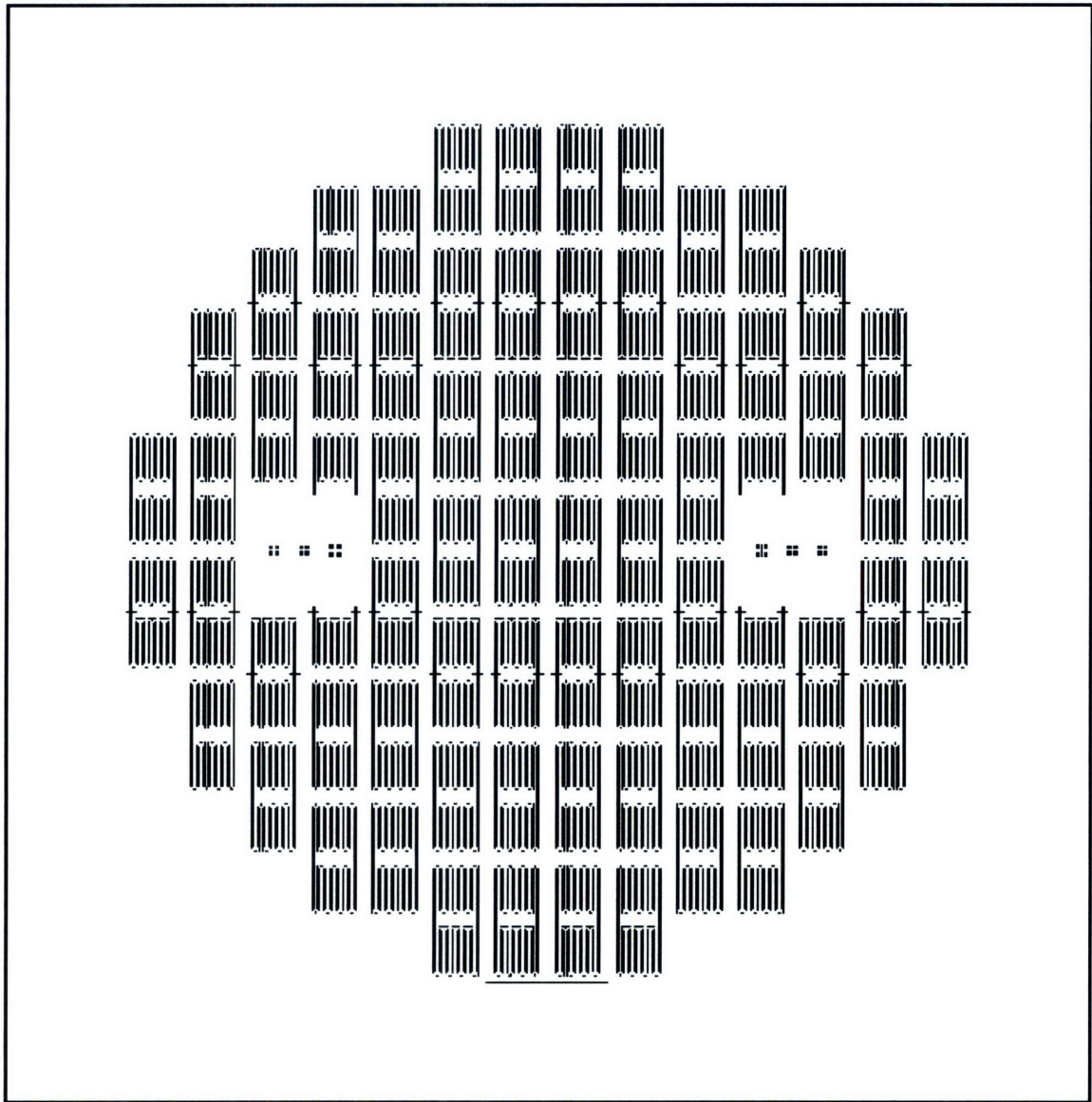
Figure C-5. Photolithography mask used to fabricate the third version of SμRE IV reactors with the channel pattern shown in Figure 4-10. This mask is referred to as "reactor" in the fabrication process outlined in Appendix B.
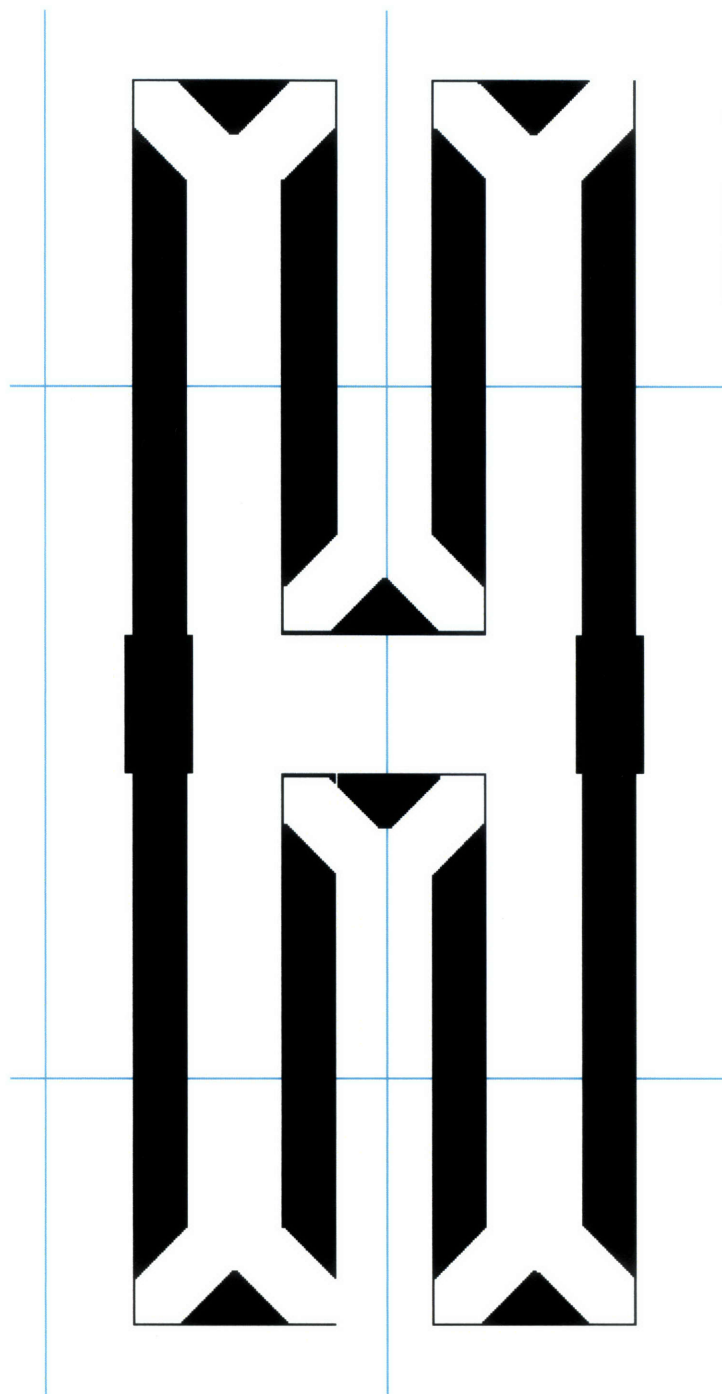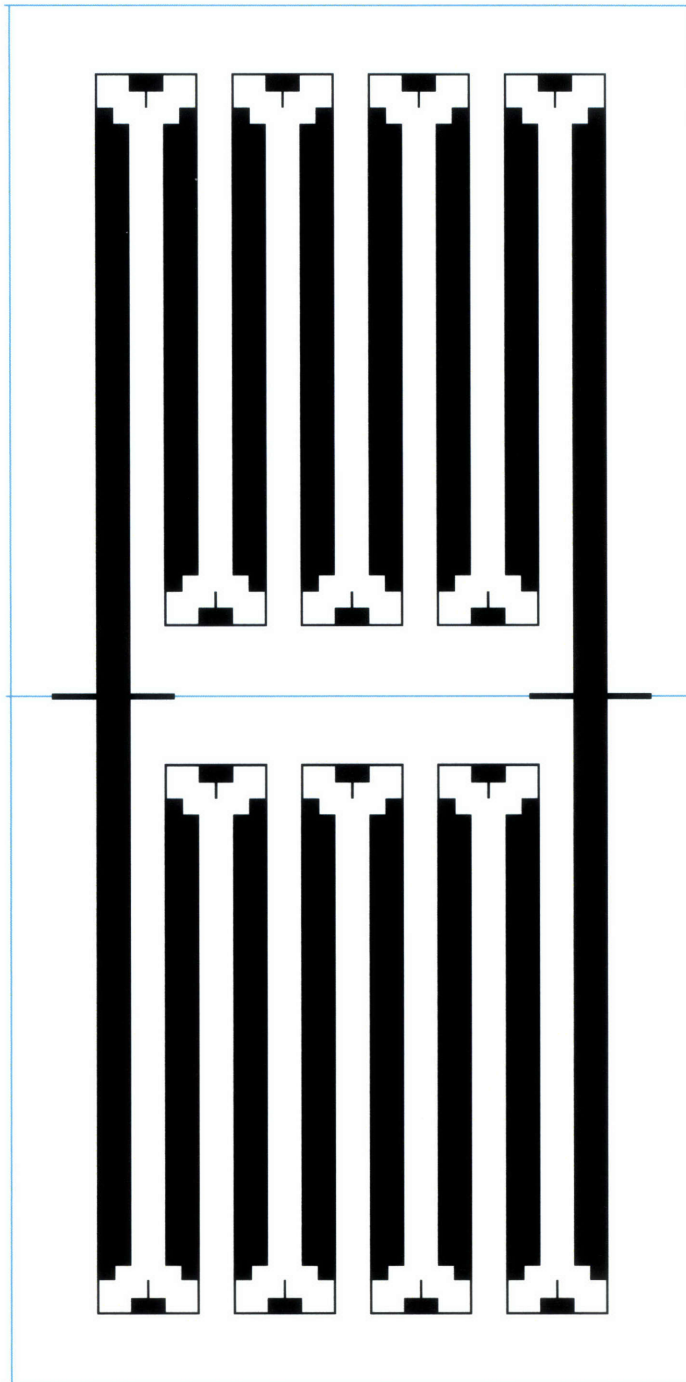
Figure C-6. Close-up view of a single cell in the photolithography mask shown in Figure C-. This mask was used to fabricate the third version of SμRE IV reactors with the channel pattern shown in Figure 4-10. This mask pattern produced convex corners that were slightly undercut due to an intentional overetch of the channels (to produce a self-terminating etch). The use of improved corner compensation features allowed for 8 total passes of the channel through the reactor. The resultant channel width using this mask is 500μm. Close packing of the channels allows for an additional two passes through the reactor compared to the first version of the channel mask. Additionally, features have been added at the inlet and outlet to produce inserts for tubes at the inlet and outlet ports.
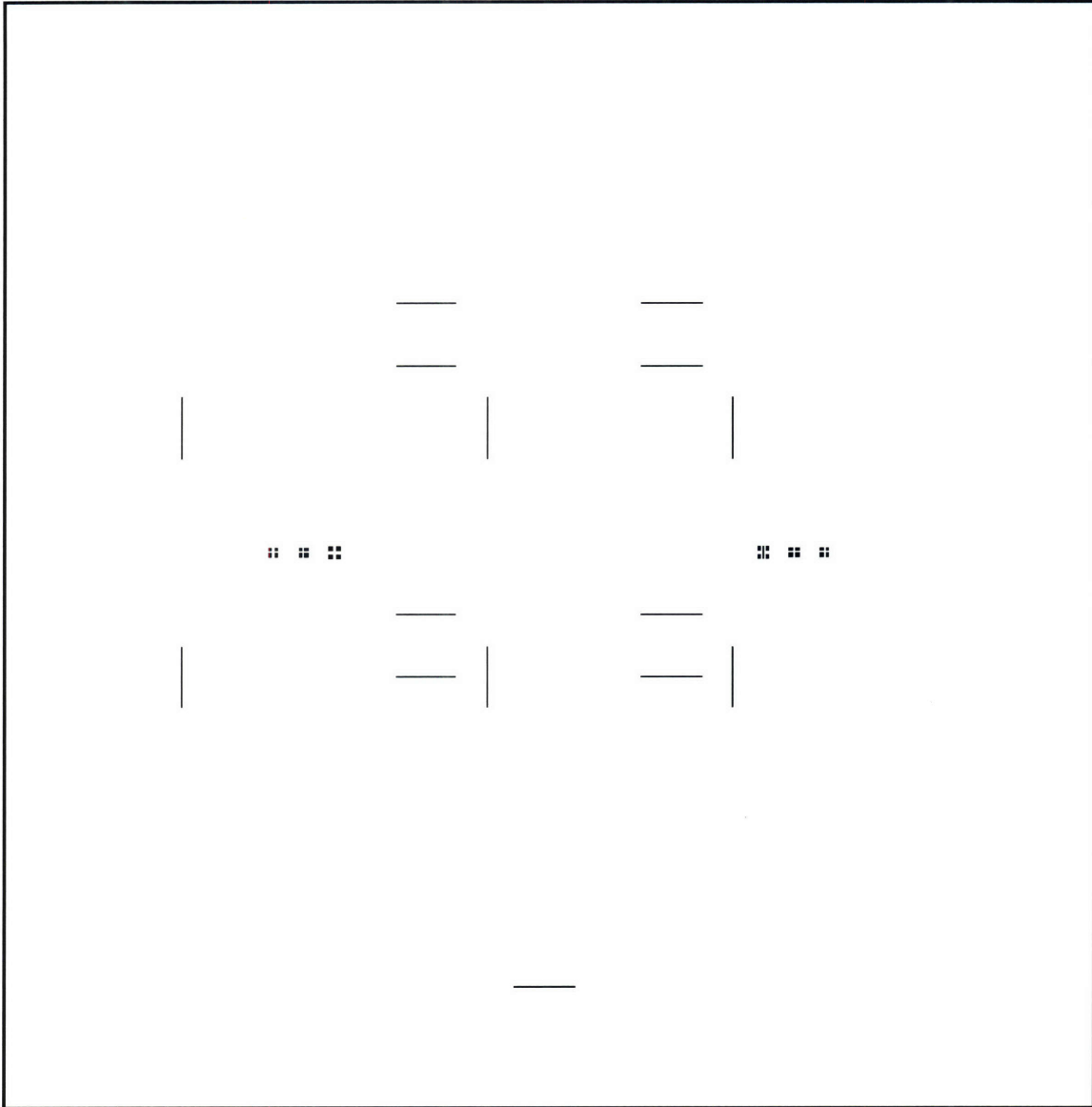
Figure C-7. Photolithography mask used to etch the alignment marks and dicing lines into the backside of the SμRE IV reactor wafer. This mask is referred to as "reactor_back" in the fabrication process outlined in Appendix B.
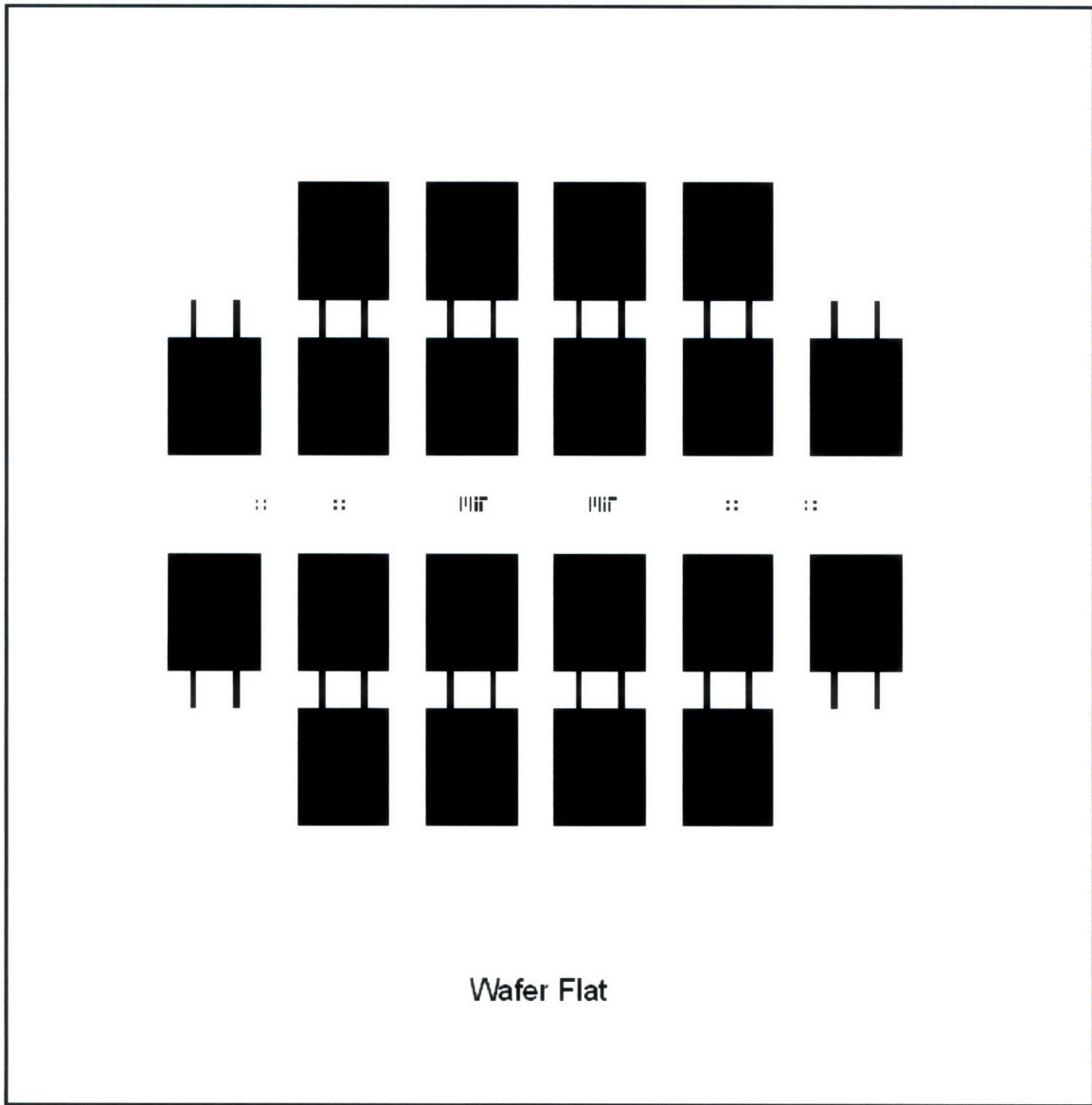
Figure C-8. Photolithography mask used to etch the bonded side of the silicon frame for SµRE IV.
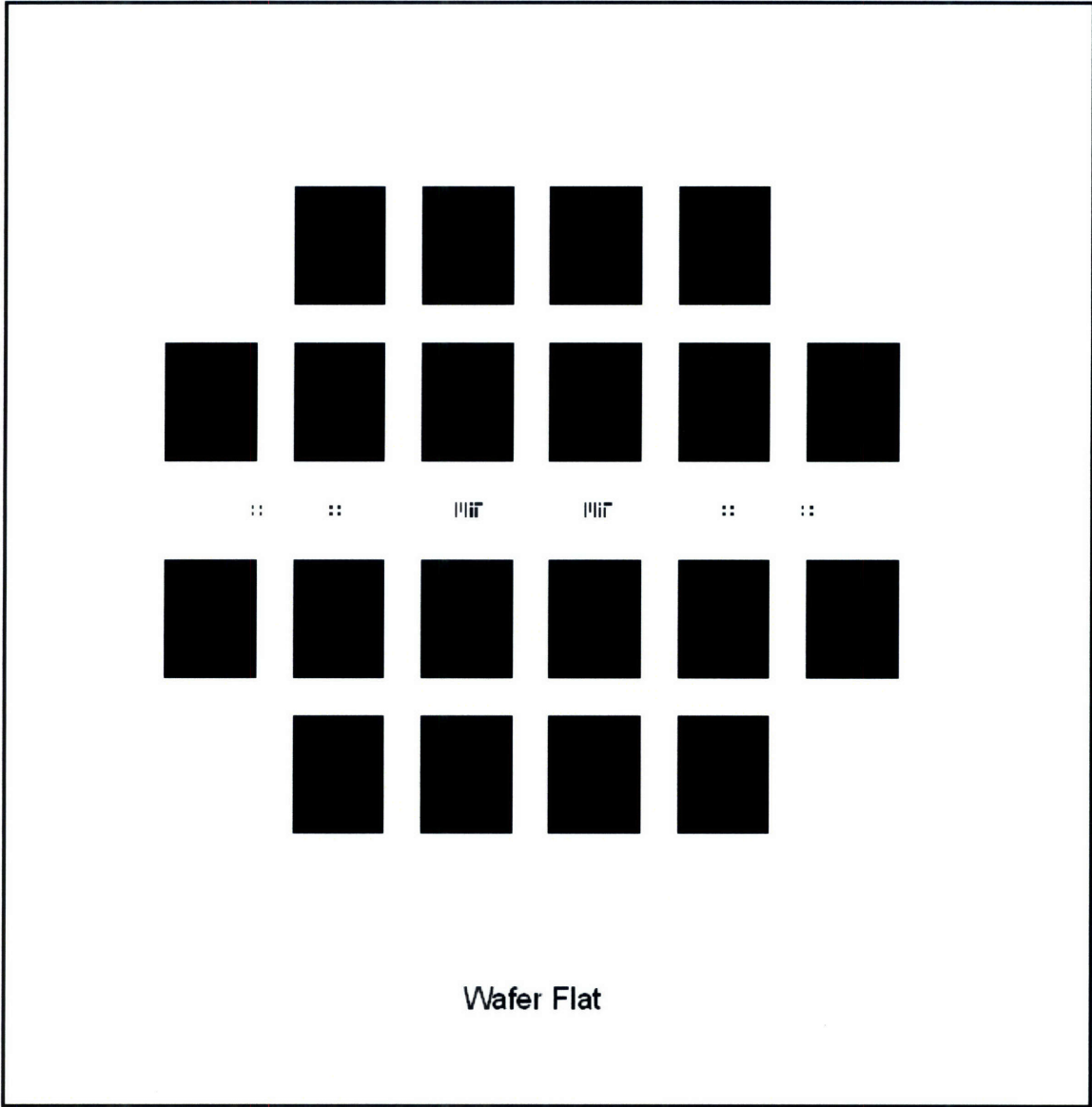
Figure C-9. Photolithography mask used to etch the bonded side of the silicon frame for SµRE IV.

Appendix D   Glass Tube Brazing

D.1   Capillary Tubes

Two types of capillary tubes were tested for use in SµRE IV: borosilicate and fused quartz. Two tube sizes were tested: 700µm OD (500µm ID) and 550µm OD (400µm ID).

D.2   Glass Sealants

A variety of glass sealants were tested for use in SµRE IV. Their properties are outlined in Table D-1. Note that under "Melt. Pt." the curing temperature has been listed for Aremco sealants.

Table D-1. Properties of Glass Sealants Tested for Use in SµRE IV

Sealant	$\alpha \times 10^{-6}$ ($^{o}C^{-1}$)	Reheat (^{o}C)	Comments
SCC-7	3.6	710	From SEM-COM
Pyrex 7760	3.3	820	
Fused Quartz	0.5	1683	
P/FQ mix	Varies	Varies	Pyrex and fused quartz mixes were testing using acetone as a solvent, Span 80 as a surfactant, and BCA and B75,000 as binders
Aremco 503	7.2	1650	Used with Aremco 617 glass sealant
Aremco 569	7.6	1650	Used with Aremco 617 glass sealant
Aremco 618N	0.59	1650	Used with Aremco 617 glass sealant
Aremco 690	3.6	850	Used with Aremco 617 glass sealant
Aremco 865	2.7	1650	Used with Aremco 617 glass sealant

D.3 Experiment Summary

The process of discovering an appropriate sealant/tubing combination involved conducting hundreds of experiments. Table D-2 includes a summary of the experimental results. When possible, the results of several experiments are summarized in one line. Under the "Tube" column, "BS" stands for borosilicate, and "FQ" stands for fused quartz. The OD of the tubing – 550 or 700 – is listed after the tube material. "T_H" is the temperature at which the sealant is melted. Under "Cooling" is the rate at which the reactor is cooled to room temperature.

Table D-2. Summary of Glass Brazing Experiments

Sealant	Tube	T_H (°C)	Cool (C/min)	Result
SCC-7	BS	690	1	This formulation worked well. Nearly 100% yield is achieved on the brazing step
SCC-7	BS	690	5 – 25	This recipe also worked, although the higher rate of cooling sometimes led to non-hermetic seals
SCC-7	FQ	690	1 – 25	SCC-7 always broke the fused quartz tubing
Pyrex	BS	< 710	1 – 25	Pyrex never achieved a hermetic seal below 710°C
Pyrex	BS	> 710	1 – 25	Borosilicate tubing deformed severely above ~710°C
Pyrex	FQ	700 – 800	1 – 25	Pyrex rarely formed a hermetic seal below 800°C. Yields were less than 5%.
Pyrex	FQ	800 – 1000	1 – 25	Differential thermal expansion, tube breakage
20:80, P:FQ	FQ	800 – 1100	1 – 25	Always led to noticeable cracks in the braze and/or tubing
30:70, P:FQ	FQ	800 – 1100	1 – 25	Always led to noticeable cracks in the braze and/or tubing
40:60, P:FQ	FQ	800 – 1100	1 – 25	Always led to noticeable cracks in the braze and/or tubing
50:50, P:FQ	FQ	800 – 1100	1 – 25	Always led to noticeable cracks in the braze and/or tubing
60:40, P:FQ	FQ	800 – 1100	1 – 25	Almost always led to noticeable cracks in the braze and/or tubing. The few reactors that did survive usually broke during handling.
70:30, P:FQ	FQ	800 – 1100	1 – 25	Almost always led to noticeable cracks in the braze and/or tubing. The few that survived handling broke during testing.

Table D-2 (continued). Summary of Glass Brazing Experiments

Sealant	Tube	T_H (°C)	Cool (C/min)	Result
80:20, P:FQ	FQ	800 – 1100	1 – 25	Almost always led to cracks in the braze and/or tubing. The few that survived handling broke during testing.
Aremco 503	FQ	871	1 – 25	Noticeable cracks were observed. Surviving reactors were always brittle and broke right out of the oven.
Aremco 503	BS	371	1 – 25	Several attempts survived, but were very fragile. Aremco sealant could never be used due to high temperature requirements, so hermetic seal was never formed.
Aremco 569	FQ	871	1 – 25	Noticeable cracks were observed.
Aremco 569	BS	371	1 – 25	Several attempts survived, but were very fragile. Aremco sealant could never be used due to high temperature requirements, so hermetic seal was never formed.
Aremco 618N	FQ	871	1 – 25	Appeared to work well, but cracks were always discovered in seal
Aremco 618N	BS	371	1 – 25	Not a good match, tubes broke often.
Aremco 690	FQ	871	1 – 25	Noticeable cracks were observed.
Aremco 690	BS	371	1 – 25	Several attempts survived, but were very fragile. Aremco sealant could never be used due to high temperature requirements, so hermetic seal was never formed.
Aremco 865	FQ	871	1 – 25	Most promising of the Aremco brazes. SEM revealed cracks in the structure, and hermetic seal was never formed
Aremco 865	BS	93	1 – 25	Reactors were less fragile than other Aremco brazes. However, sealant could not be used with borosilicate glass.

Appendix E   Pulse Chemisorption

In order to compare the activity of supported metal catalysts among multiple samples, it is necessary to extract the active surface site density. Quantifying the active surface site density is also important when deriving a kinetic expression for a homogeneous catalytic reaction system. Catalyst characterization procedures should be performed *in situ* when possible, as changes in environment can often affect catalyst performance. For this reason, a system was developed to measure, *in situ*, the number of active catalyst surface sites in a loaded microreactor using pulse chemisorption.

E.1   Single-Channel Reactor

The microreactors used for the pulse chemisorption experiments were fabricated using two 150-mm wafers, one double-side polished silicon wafer and one Pyrex® wafer. The fabrication of the original reactor has been described by Baertsch et al [82]. A few modifications were made for the reactors used in these experiments, namely the inclusion of a resistive heater on the backside of the reactor. A silicon dioxide mask was patterned to form the channel features. The channels were 20 mm long and 1 mm wide and included 50×300 μm retention posts at one end. Six thermocouple wells – three on each side of the channel – were spaced 5 mm apart. The silicon dioxide mask was nested under a 10 μm-thick photoresist mask. The photoresist mask was used to mask the DRIE of 600 μm diameter fluidic ports. The DRIE was performed in two steps; first, the ports were etched to a depth of 400 μm, and next, the channels were etched to a depth of ~350 μm. After etching, the oxide mask was stripped. Negative photoresist was deposited on the backside of the wafer using an airbrush; spinning photoresist was not effective once the fluidic ports were etched through the wafer. The resist was patterned

and a 10/200/20 nm tri-layer of Ta/Pt/Ta was deposited to act as a resistive heater. Prior to bonding, only a native oxide remained on the surface of the reactor. The channel was sealed by anodically bonding the Pyrex$^{®}$ wafer to the smooth silicon surface. The single channel reactor is shown in Figure E-1.
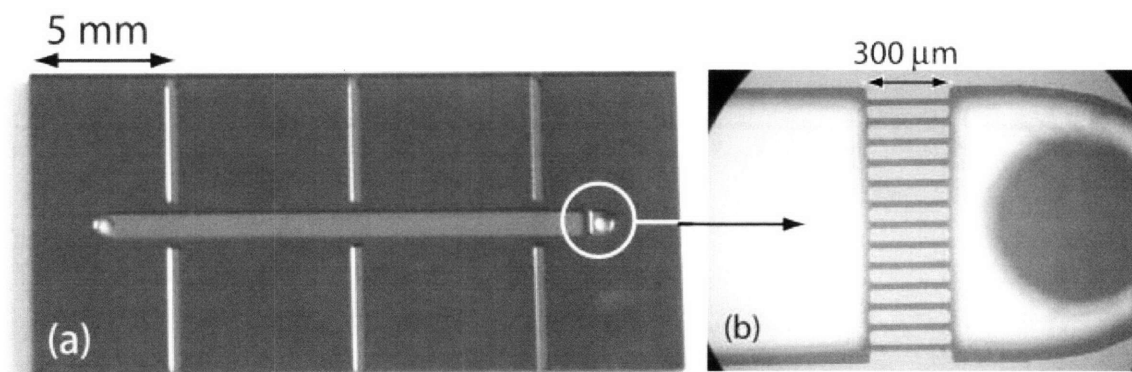
Figure E-1. Photograph of (a) the axial flow single-channel microreactor including (b) the detail of the catalyst retention posts [82].

In order to pre-treat the catalyst at temperatures above 400 °C, the reactor had to be thermally isolated from the environment. This was achieved by using the glass brazing technique described in Section 4.2.3. 2-mm OD Pyrex tubes (1 mm ID) were brazed to the silicon surface using pre-formed glass frits of SCC-7 glass (SEMCOM). The results of the brazing procedure are shown in Figure E-2.
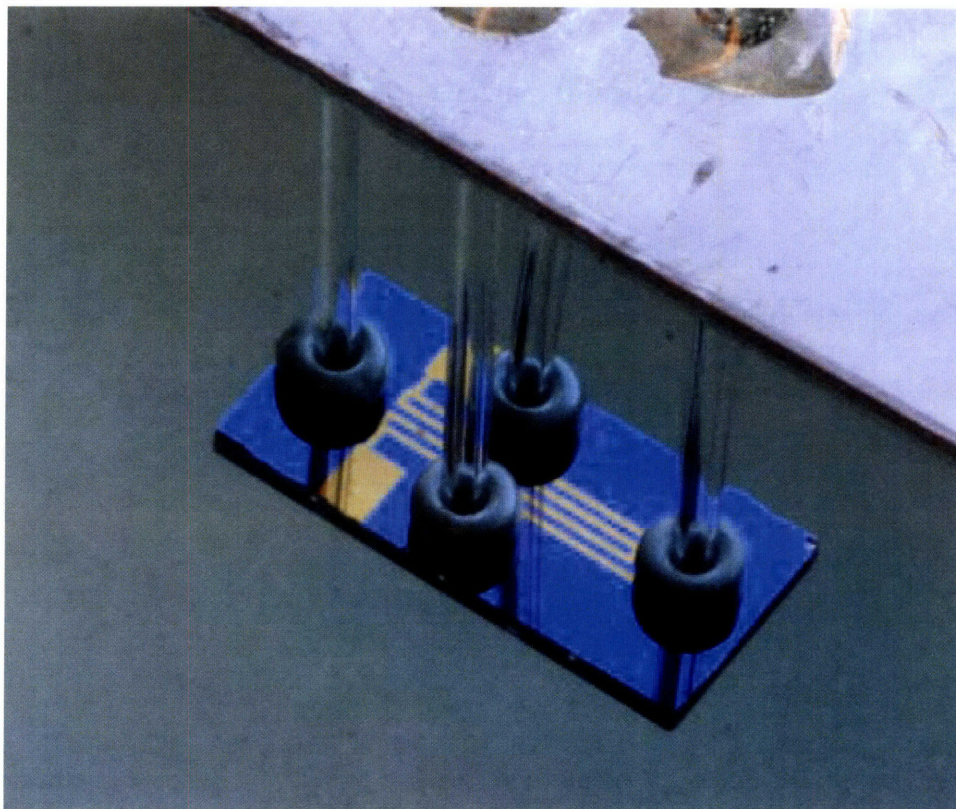
Figure E-2. Photograph of the axial flow single-channel microreactor with glass brazed fluidic connections. The two tubes covering the ports of the reactor are used to make fluidic connections while the other two tubes are used for support.

E.2   Experimental Procedure

The experimental setup for the pulse chemisorption system is shown in Figure E-3.
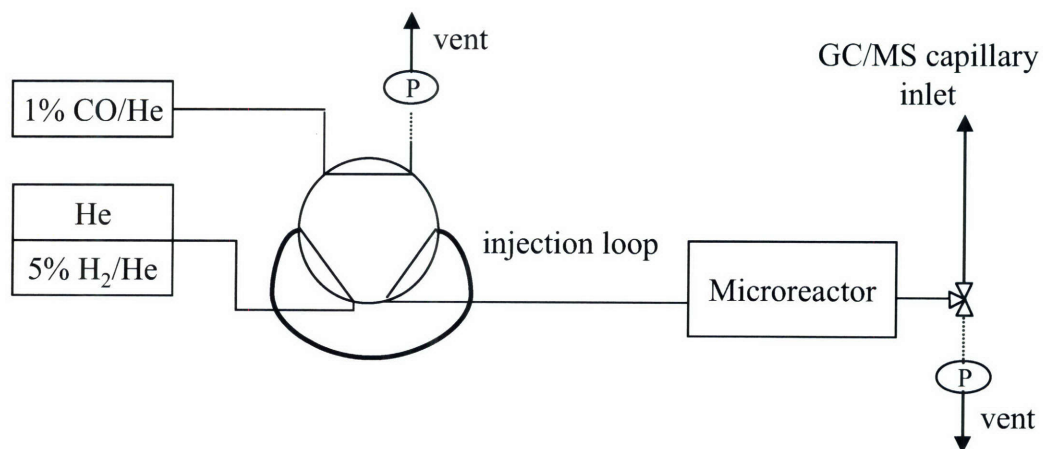
Figure E-3. Experimental setup for pulse chemisorption experiments.

Fluidic connections to the single-channel microreactor were made by compressing a Kalrez® elastomer between the supporting aluminum plate and the aluminum fluidic chuck. Reactors were loaded by drawing supported catalyst powders through the channel using a vacuum line attached to the outlet of the reactor. Fully loaded reactors contained ~4 mg of catalyst. The weights of loaded catalyst were determined by measuring the weight of the microreactor before and after loading using a 6-place Sartorius microbalance. The catalyst retention posts prevented catalyst from escaping the reactor exit, and quartz wool was packed into the inlet tube to prevent catalyst from exiting the inlet. For experiments in which larger samples of catalyst were to be analyzed, a 1/8" stainless-steel tube was used.

The single-channel micro reactor was heated during pre-treatment steps using the thin-film resistive heater. Pre-treatment began with dehydration of the catalyst bu flowing 25 sccm pure He over the heated reactor for 1 hour. Next, 25 sccm of 5% H_2 was flowed to reduce the catalyst. Finally, 25 sccm of pure He was again flowed for 1 hour before the reactor was cooled to room temperature.

After pre-treating, pulse chemisorption was performed for 1wt% Pt on Al_2O_3 support (178 m^2 g^{-1}, Aldrich chemical). 25-1000 μL pulses of 1% CO in He gas at 1 atm gauge pressure were injected using an electronically actuated Valco EC6WE 6-way sampling valve. The sub 100-ms sampling speed was necessary to ensure no exhaust gases flowed back over the catalyst during switching. The exhaust gases were analyzed using an Inficon Transpector2 mass spectrometer (MS). The cumulative CO uptake was determined by summing the areas of the eluted CO peaks. Pt dispersion was calculated assuming an adsorption ratio of 1 CO molecule per active Pt surface site.

E.3 Experiments

The experimental results obtained for the single-channel microreactors were inconsistent, generally underestimating the amount of active surface sites. The biggest problem encountered during experimentation was the inability to measure the eluted CO peaks consistently due very low signal to noise ratios. Part of the reason for the large amount of noise in the system was that the packaging of the single-channel reactor included a large amount of dead volume. This resulted in a large amount of CO peak broadening; by the time the CO peaks reached the mass spec, the peaks were too broad to measure. In addition, small leaks in the system were detected on numerous occasions. This leads to both CO loss and nitrogen contamination. When nitrogen is allowed to enter the system, the baseline CO signal is amplified due to the similar masses of the two species (28 amu).

Several successful runs were performed using 1/8" stainless-steel reactors. The results of one such run are shown in Figure E-4 below. In this case, 185 mg of 1wt% Pt on Al_2O_3 were loaded into the reactor. 1000 µL pulses were flowed over the sample, and a 40% dispersion of catalyst was calculated. This number was very close to Baertsch's reported dispersion of 41% as well as the dispersion reported in the Aldrich packaging.
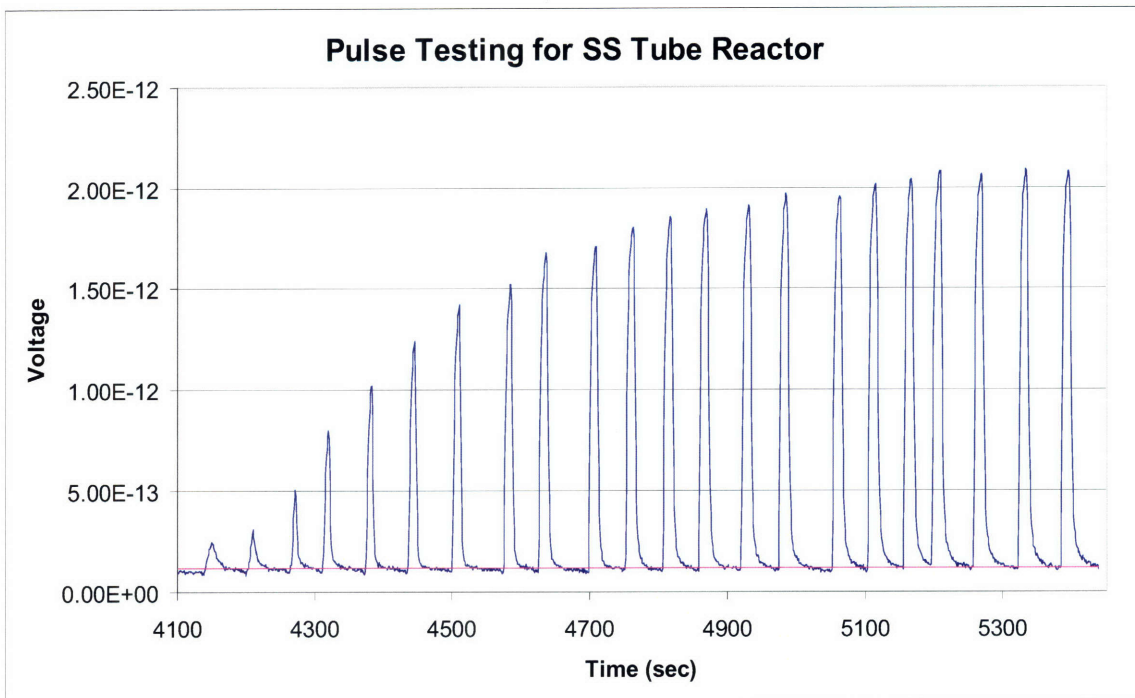
Figure E-4. Pulse chemisorption output for a 185 mg sample of 1wt% Pt on Al_2O_3 catalyst. A 1/8" stainless-steel tube reactor was used for this experiment.

Appendix F   Autothermal Hydrogen Generation

Several experiments were conducted to investigate the use of SμRE IV for the autothermal production of hydrogen via ammonia cracking. Reactor stacks similar to the one shown in Figure 4-13 were used for the experiments. The reactors used for these experiments included the original channel layout, shown in Figure 4-8. 550μm tubing was fed to the bottom of the first channel pass, causing the hot spot to form in the middle of the reactor. Propane combustion was used to supply the necessary thermal energy to power the endothermic ammonia cracking reaction. A 1.1:1 stoichiometric ratio of oxygen to propane was fed to the top reactor, which was combusted over 5wt% Pt on Al_2O_3 catalyst. Anhydrous ammonia was fed to the bottom reactor, which was loaded with 3wt% Ir on Al_2O_3 catalyst. The ammonia inlet was aligned with the propane outlet. The counter-current flow configuration allowed for the pre-heating of the ammonia inlet by the propane combustion exhaust. In addition, it allowed for the gradual heating of the ammonia prior to making contact with the hottest spot on the reactor. The reactor operation is shown in Figure F-1.
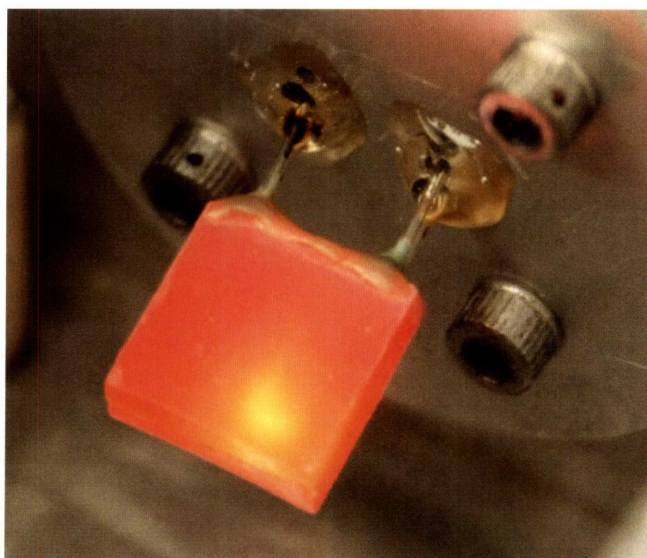
Figure F-1. SμRE IV reactor stack used for autothermal hydrogen production via ammonia cracking.

The mass flow controllers used in the system could not be sufficiently calibrated prior to operation, and therefore, the hydrogen production could not be quantified. However, the mass spectrometer output – shown in Figure F-2 – clearly showed hydrogen production in the system. Hydrogen production ceased at 800 and 1450 seconds. In both cases, the propane flow had been shut off, causing the reactor temperature to drop. The hydrogen production never reaches a steady state due to the erratic behavior of the ammonia mass flow controller. Future work should focus on building a system in which the hydrogen production can be quantified, and optimizing the system to maximize hydrogen output.
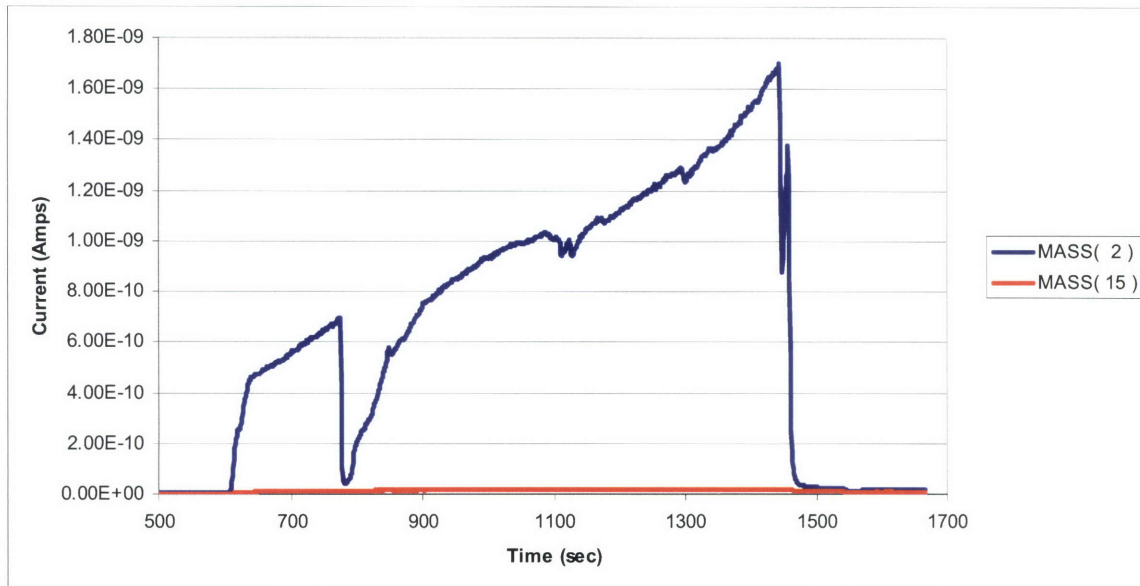
Figure F-2. Mass spectrometer output for autothermal hydrogen production via ammonia cracking. A steady-state concentration was never observed for hydrogen due to erratic behavior of the ammonia mass flow controller.

References

1. http://www.protonex.com/profuelc720.html, July 15, 2007.
2. Blomgren, D. *Perspectives on portable lithium ion batteries: lithium and polymer electrolyte types*. in *17th Annual Battery Conference on Applications and Advances*. 2002.
3. Release, *China Laptop Industry Report*, in *Research and Markets*. 2006-2007.
4. Release, *Semiconductor Industry Association*. 2006.
5. Brodd, R.J., *Recent developments in batteries for portable consumer electronics applications*. Electrochem. Soc. Interface, 1999. **8**: p. 20-23.
6. Atwater, T.B., P.J. Cygan, and F.C. Leung, *Man portable power needs of the 21st Century. I. Applications for the dismounted soldier. II. Enhanced capabilities through the use of hybrid power sources*. J. Power Sources, 2000. **91**: p. 27-36.
7. Plichta, E.J., M.A. Hendrickson, and R.P. Hamlen. *Mobile power challenges for the Army's objective force*. in *17th Annual Battery Conference on Applications and Advances*. 2002.
8. Linden, D. and T. Reddy, *Handbook of Batteries*, ed. McGraw-Hill. 2002, New York.
9. Ragone, D.V. *Review of battery systems for electrically powered vehicles*. in *Proceedings of the Mid-Year Meeting of the Society of Automotive Engineers*. 1968. Detroit, MI.
10. *Perry's Chemical Engineers' Handbook*. 7th Edition ed, ed. McGraw-Hill. 2002.
11. Arana, L., *High-Temperature Microfluidic Systems for Thermally-Efficient Fuel Processing*, in *Chemical Engineering*. 2003, MIT: Cambridge.
12. Mehra, A., et al., *A six-wafer combustion system for a silicon micro gas turbine engine*. Journal of Microelectromechanical Systems, 2000. **9**: p. 517-527.
13. A.H. Epstein, S.D.S., et al. in *IEEE Conference on Solid-State Sensors and Actuators (Transducers '97)*. 1997. Chicago.
14. Fu, K., et al. *Microscale Combustion Research for Applications to MEMS Rotary IC Engine*. in *National Heat Transfer Conference*. 2001.
15. Fu, K., et al. *"Design and Experimental Results of Small-Scale Rotary Engines"*. in *International Mechanical Engineering Congress and Exposition (IMECE)*. 2001. New York.
16. Arnold, D.P., *Magnetic induction machines integrated into bulk-micromachined silicon*. Journal of Microelectromechanical Systems, 2006. **15**(2): p. 406-414.
17. Stauffer, N., *Engine on a chip promises to best the battery*, in *MIT News Office*. 2006.
18. Shaevitz, S.B., *A MEMS thermoelectric generator*. Dept. Electrical Engineering and Computer Science, 2000.
19. Sitzki, L., et al. *Combustion in Microscale Heat-Recirculating Burners*. in *Proceedings of the Third Asia-Pacific Conference on Combustion*. 2001. Seoul, Korea.
20. O.M. Nielsen, L.R.A., C.D. Baertsch, K.F. Jensen, and M.A. Schmidt. *A Thermophotovoltaic Micro-Generator for Portable Power Applications*. in *12th International Conference on Solid-State Sensors, Actuators, and Microsystems (Transducers '03)*. 2003.
21. Yang, Y.M., et al., *Development of a prototype micro-thermophotovoltaic power generator*. Journal of Physics D: Applied Physics, 2004. **37**: p. 1017-1020.

22. L.M. Fraas, J.E.A., and H.X. Huang. *Thermophotovoltaics: heat and electric power from low bandgap 'solar' cells around a gas-fired radiant tube burner*. in *29th IEEE PVSC Conference*. 2002.

23. Carrete, L., K.A. Friedrich, and U. Stimming, *Fuel cells - fundamentals and applications*. Fuel Cells, 2001. **1**: p. 5-39.

24. Bernay, C., M. Marchanda, and M. Cassir, *Prospects of different fuel cell technologies for vehicle applications*. Journal of Power Sources, 2002. **108**: p. 139–152.

25. Folkessona, A., et al., *Real life testing of a Hybrid PEM Fuel Cell Bus*. Journal of Power Sources, 2003. **118**: p. 349–357.

26. VanMierlo, J., G. Maggetto, and P. Lataire, *Which energy source for road transport in the future? A comparison of battery, hybrid and fuel cell vehicles*. Energy Conversion and Management, 2006. **47**: p. 2748–2760.

27. Zegers, P., *Fuel cell commercialization: The key to a hydrogen economy*. Journal of Power Sources, 2006. **154**: p. 497–502.

28. Cheng, X., et al., *A review of PEM hydrogen fuel cell contamination: Impacts, mechanisms, and mitigation*. Journal of Power Sources, 2007. **165**: p. 739-756.

29. St.-Pierre, J. and D.P. Wilkinson, *Fuel cells: a new, efficient, and cleaner power source*. AIChE Journal, 2001. **47**: p. 1482-1486.

30. Lee, S.J., et al., *Design and fabrication of a micro fuel cell array with "flip-flop" interconnection*. Journal of Power Sources, 2002. **112**: p. 410-418.

31. Park, B.Y. and M.J. Madou, *Design, fabrication, and initial testing of a miniature PEM fuel cell with micro-scale pyrolyzed carbon fluidic plates*. Journal of Power Sources, 2006. **162**: p. 369-379.

32. *NTT prototype micro PEM for cell phones*. Fuel Cells Bulletin, 2005. **2005**: p. 6.

33. http://www.mtimicrofuelcells.com/, July 15, 2007.

34. http://www.ultracellpower.com/, July 15, 2007.

35. Shafirovich, E., V. Diakov, and A. Varma, *Combustion-assisted hydrolysis of sodium borohydride for hydrogen generation*. International Journal of Hydrogen Energy, 2007. **32**: p. 207-211.

36. Muradov, N.Z., *CO2-free production of hydrogen by catalytic pyrolysis of hydrocarbon fuel*. Energy & Fuels, 1998. **12**: p. 41-48.

37. Peña, M.A., J.P. Gómez, and J.L.G. Fierro, *New catalytic routes for syngas and hydrogen production*. Appl. Cat. A., 1996. **144**: p. 7-57.

38. L.R. Arana, S.B.S., A.J. Franz, Martin A. Schmidt, K. F. Jensen, *A microfabricated suspended-tube chemical reactor for thermally-efficient fuel processing*. J. MicroElectromechanical Systems, 2003. **12**: p. 600-612.

39. Palo, D.R., et al., *Development of a soldier-portable fuel cell power system Part I: A bread-board methanol fuel processor*. J. Power Sources, 2002. **108**: p. 28-34.

40. Holliday.

41. Horny, C., A. Renken, and L. Kiwi-Minsker, *Compact string reactor for autothermal hydrogen production*. Catalysis Today, 2007. **120**: p. 45-53.

42. J.C. Ganley, E.G.S., R. Masel, *Porous anodic alumina microreactors for production of hydrogen from ammonia*. AIChE Journal, 2004. **50**: p. 829-834.

43. Kutz, M., *Mechanical Engineers' Handbook - Energy and Power*. 2006: John Wiley and Sons.

44. Kraus, A.D. and A. Bejan, *Heat Transfer Handbook*. 2003: Wiley-IEEE.

45.   Gavriilidis, A., et al., *Technology and applications of microengineered reactors*. Trans. IChemE, 2002. **80**: p. 3-30.

46.   Lai, Y., E.V. Bordatchev, and S.K. Nikumb, *Metallic micro displacement capacitive sensor fabricated by laser micromachining technology*. Microsystem Technologies, 2006. **12**: p. 778-785.

47.   Matson, D., et al., *Fabrication of microchannel reactors using a metal lamination process*. Proc. 3rd International Conference on Microreaction Technology (IMRET 3), 1999.

48.   Matson, D.W., et al., *Laser-micromachined microchannel solvent separator*. Proceedings of SPIE, 1997. **3223**: p. 253-259.

49.   Martin, P.M., D.W. Matson, and W.D. Bennett, *Fabrication of plastic microfluidic components*. Proceedings of SPIE, 1998. **3515**: p. 172-176.

50.   Martin, P.M., et al., *Laser-micromachined and laminated microfluidic components for miniaturized thermal, chemical, and biological systems*. Proceedings of SPIE, 1999. **3680**: p. 826-833.

51.   Martin, P.M., et al., *Laser micromachined and laminated microchannel components for chemical sensors and heat transfer applications*. Proceedings of SPIE, 1997. **3224**: p. 258-265.

52.   Nielsen, O., *A Thermally Efficient Micro-Reactor for Thermophotovoltaic Power Generation*, in *Electrical Engineering and Computer Science*. 2006, MIT: Cambridge.

53.   Shanks, H.R., et al., *Thermal conductivity of silicon from 300 to 1400 K*. Physical Review, 1963. **130**: p. 1743-1748.

54.   Littleton, J.T., *A New Method for Measuring the Tensile Strength of Glass*. Physical Review, 1923. **22**(5): p. 510-516.

55.   Schroder, H. and E. Obermeier, *A new model for Si{100} convex corner undercutting in anisotropic KOH etching*. J. Micromech. Microeng., 2000. **10**: p. 163-170.

56.   Zhang, Q.L., L. Liu, and Z. Li, *A new approach to convex corner compensation for anisotropic etching of (100) Si in KOH*. Sensors and Actuators A, 1996. **56**: p. 251-254.

57.   G.K. Mayer, H.L.O., H. Sandmaier, and K. Kuehl, *Fabrication of Non-Underetched Convex Corners in Anisotropic Etching of (100)-Silicon in Aqueous KOH with Respect to Novel Micromechanical Elements*. Journal of the Electrochemical Society, 1990. **137**: p. 3947-3950.

58.   Fan, W. and D. Zhang, *A simple approach to convex corner compensation in anisotropic KOH etching on a (1 0 0) silicon wafer*. Journal of Micromechanics and Microengineering, 2006. **16**: p. 1951-1957.

59.   http://www.vitrocom.com/useful_info.html, August 30, 2007.

60.   Senturia, S.D., *Microsystem Design*. 2001, Boston: Kluwer.

61.   Sato, T., *Spectral Emissivity of Silicon*. Japanese Journal of Applied Physics, 1967. **6**(3): p. 339-347.

62.   Schefer, R.W., *Catalyzed Combustion of H2/Air Mixtures in a Flat Plate Boundary Layer: II. Numerical Model*. Combustion and Flame, 1982. **45**: p. 171-190.

63.   Satterfield, C.N., *Heterogeneous Catalysis in Industrial Practice*. 1996, Malabar: Krieger Publishing Company.

64.   Wagner, C., *The interaction of streaming diffusion and chemical reaction on heterogeneous catalysts*. Z Physik Chem, 1943. **A193**: p. 1-15.

65. Westenberg, A.A. and G. Frazier, *Molecular diffusion studies in gases at high temperature. V. Results for the H₂-Ar system.* Journal of Chemical Physics, 1962. **36**: p. 3499-3500.

66. Reid, R.C., J.M. Prausnitz, and T.K. Sherwood, *The Properties of Gases and Liquids.* 1977, New York: McGraw-Hill.

67. E. Ruckenstein, C.A.P., *On the aging of supported metal catalysts due to hot spots.* Chemical Engineering Science, 1972. **27**: p. 937-946.

68. Chu, Y.F. and E. Ruckenstein, *On the sintering of platinum on alumina catalyst.* Journal of Catalysis, 1978. **55**: p. 281-298.

69. Adler, S.F. and J.J. Keavney, *The physical nature of supported platinum.* Journal of Physical Chemistry, 1960. **64**: p. 208-212.

70. Lieskeb, H., et al., *Reactions of platinum in oxygen- and hydrogen-treated Pt/γ-Al₂O₃ catalysts I. Temperature-programmed reduction, adsorption, and redispersion of platinum* Journal of Catalysis, 1983. **81**: p. 8-16.

71. Rickard, J.M., et al., *Redispersion of platinum on Pt/Al₂O₃ model catalyst in oxygen studied by transmission electron microscopy.* Journal of Catalysis, 1990. **121**: p. 141-152.

72. Moro-oka, Y., Y. Morikawa, and A. Ozaki, *Regularity in the catalytic properties of metal oxides in hydrocarbon oxidation.* Journal of Catalysis, 1967. **7**: p. 23-32.

73. Johnson, M.L. and C.D. Keith, *The state of platinum in reforming catalysts.* Journal of Physical Chemistry, 1963. **67**: p. 200-201.

74. Susu, A.A., E.O. Ogogo, and H.M. Ngomo, *The effect of sintering-redispersion on the selective aromatic yield on supported platinum catalysts.* Chemical Engineering Research and Design, 2006. **84**: p. 664-676.

75. Ma, L., D.L. Trimm, and C. Jiang, *The design and testing of an autothermal reactor for the conversion of light hydrocarbons to hydrogen I. The kinetics of the catalytic oxidation of light hydrocarbons.* Applied Catalysis A: General, 1996. **138**: p. 275-283.

76. Burch, R., et al., *The nature of activity enhancement for propane oxidation over supported Pt catalysts exposed to sulphur dioxide.* Applied Catalysis B: Environmental, 1998. **19**: p. 199-207.

77. Yazawa, Y., et al., *Kinetic study of support effect in the propane combustion over platinum catalyst.* Catalysis Letters, 2001. **72**: p. 157-160.

78. Bennett, C.J., S.T. Kolaczkowski, and W.J. Thomas, *Determination of Heterogeneous Reaction Kinetics and Reaction Rates under Mass Transfer Controlled Conditions for a Monolith Reactor.* Trans. I. Chem. E., 1991. **69B**: p. 209-220.

79. Saracco, G. and V. Specchia, *Catalytic combustion of propane in a membrane reactor with separate feed of reactants. IV. Transition from the kinetics- to the transportcontrolled regime.* Chemical Engineering Science, 2000. **55**: p. 3979-3989.

80. Otto, K., J.M. Andino, and C.L. Parks, *The influence of platinum concentration and particle size on the kinetics of propane oxidation over Pt/alumina.* Journal of Catalysis, 1991. **131**(1): p. 243-251.

81. Wanke, S.E., *Oxidation of Propane over a Diesel Exhaust Catalyst.* Can. J. Chem. Eng, 1973. **51**: p. 454-458.

82. Baertsch, C.D., M.A. Schmidt, and K.F. Jensen, *Catalyst surface characterization in microfabricated reactors using pulse chemisorption.* Chemical Communications, 2004. **2004**: p. 2610-2611.